Ghent University
Faculty of Sciences
Department of Solid State Sciences
Krijgslaan 281/S1, 9000 Ghent, Belgium

In Situ Synchrotron Based Fluorescence and Scattering Techniques: A Study of Quantum Dot Encapsulation by Atomic Layer Deposition.

Kilian Devloo-Casier

Promotors: Prof. dr. Christophe Detavernier
Dr. ir. Jolien Dendooven

(Other) Members of the Jury:

Prof. dr. Dirk Poelman (UGent, chair)
Prof. dr. Ruud Van Ommen (TU Delft)
Prof. dr. Giuseppe Portale (University of Groningen)
Dr. Massimo Tallarida (Alba Synchrotron)
Prof. dr. ir. Gunther Roelkens (UGent)
Prof. dr. ir. Zeger Hens (UGent)
Dr. Eduardo Solano Minuesa (UGent)

Universiteit Gent
Faculteit Wetenschappen

Vakgroep Vastestofwetenschappen
Krijgslaan 281, S1, B-9000 Gent, België

Tel.: +32 9 264 43 42
Fax.: +32 9 264 49 96

Thesis submitted for the degree of
Doctor in Sciences: Physics
Academic year 2015-2016

Preface

In this PhD thesis, various *in situ* synchrotron based x-ray techniques are introduced for the study of atomic layer deposition. In the first part of this work, the relevance of the proposed techniques to ALD research is illustrated. In the second part, these techniques get applied to a study of quantum dot encapsulation. The research in this work, contains results from experiments conducted from September 2010 up to November 2015. The experimental work, contained in this thesis, was carried out at the Department of Solid State Sciences of Ghent University and at beamline X21 of the National Synchrotron Light Source at Brookhaven National Lab. Part of the work was obtained through collaboration between CoCooN and PCN at Ghent University and the Physics Department at Boston University.

This thesis is article-based and the results are presented as reformatted papers that have been published in or will be submitted to peer-reviewed journals. Introduction and framing is added, preceding the relevant article(s). I can only hope that you enjoy reading the following manuscript and that I can convince you of the unique possibilities offered by the use of synchrotron based techniques.

Ghent, February 2016
Kilian Devloo-Casier

Nederlandstalige samenvatting –Summary in Dutch–

Inleiding

Atomaire Laag Depositie (ALD) is een dunne film depositie techniek. Tijdens de depositie wordt het oppervlak afwisselend blootgesteld aan verschillende pulsen van reactieve gassen. Deze gassen reageren sequentieel op een zelf-limiterende manier met het oppervlak. Op deze manier wordt tijdens opeenvolgende ALD cycli telkens een (sub-)monolaag van het gekozen materiaal gegroeid.

Het onderliggende reactie mechanisme, eigen aan een ALD proces, levert ALD enkele opmerkelijke voordelen op in vergelijking met andere dunne film depositie technieken. Het belangrijkste voordeel van ALD is de controle over de dikte van de afgezette laag tot op het Ångstrom niveau. Een tweede voordeel is het conformele gedrag van ALD dat eveneens resulteert uit het zelf-limiterende karakter van ALD. Hierdoor kunnen complexe structuren met een hoge aspect ratio conformeel worden bedekt. Dit wil zeggen dat op elke positie van een complex 3D gestructureerd oppervlak een laag met dezelfde dikte wordt afgezet. Een laatste voordeel is de chemische selectiviteit van het ALD proces. ALD groei zal enkel optreden indien de juiste oppervlakte groepen aanwezig zijn. Dit biedt de mogelijkheid om via patterning een voorgedefinieerde zone te selecteren voor ALD groei. Naast deze voordelen heeft ALD als belangrijkste beperking een lage groeisnelheid, die filmgroei limiteert in de praktijk de laag diktes van 1Å tot 1 μm.

De lage groeisnelheid impliceert indirect dat om ALD processen in detail te analyseren zeer nauwkeurige technieken moeten worden gebruikt. In deze thesis willen we dan ook *in situ* synchrotron gebaseerde technieken introduceren om ALD te bestuderen. Deze technieken breiden de beschikbare set analyse methodes uit en kunnen onderzoekers een nauwkeuriger beeld geven van het ALD proces. In het eerste deel worden verschillende *in situ* synchrotron gebaseerde technieken geïntroduceerd. Telkens wordt de link met ALD onderzoek toegelicht. In het tweede deel worden enkele van deze technieken gebruikt om de ALD inkapseling van quantum dots te bestuderen. Het gebruik van deze technieken biedt inzichten die via meer conventionele onderzoekstechnieken onbereikbaar zouden zijn.

Deel I: X-stralen technieken bij in situ onderzoek van ALD

Tijdens de voorbije twee decennia werden verschillende *in situ* methodes ontwikkeld om ALD processen te karakteriseren. Licht gebaseerde technieken zijn veruit de eenvoudigste in gebruik. Deze laten namelijk toe om het ALD proces van op afstand te bestuderen, zonder dat er een fysiek contact nodig is met het sample. Visueel, UV en IR licht worden courant gebruikt, bv. in spectroscopische ellipsometrie en infrarood absorptie spectroscopie.

In dit werk breiden we het golflengte gebied uit van het optische gebied naar het x-stralen bereik, waardoor een nieuwe set technieken beschikbaar komt (bv. XRR, XRF and GISAXS). Op deze manier worden een nieuwe set karakteristieke eigenschappen van het ALD proces en van de groeiende film *in situ* meetbaar. Als we de x-stralen genereren aan een synchrotron ipv. met behulp van een labo bron, dan kunnen we gebruik maken van twee extra voordelen, inherent aan synchrotron straling. Ten eerste, reduceert de hoge foton flux de nodig meettijd en wordt de detectie limiet verlaagd. Dit zorgt ervoor dat de voorgestelde methodes gevoelig worden voor veranderingen op het (sub-)nanometer niveau. Ten tweede, kan de energie van de x-stralen aan een synchrotron worden aangepast, wat bv. XAS mogelijk maakt. In hoofdstuk 4 worden mogelijke *in situ* technieken besproken en wordt toegelicht en geïllustreerd wat hun nut kan zijn binnen ALD onderzoek:

XRR
: X-stralen reflectiviteit (X-ray reflectivity, XRR) kan gebruikt worden om de dikte, ruwheid en dichtheid van een ALD gegroeide dunne film te bestuderen.

GISAXS
: X-stralen verstrooing onder scherende inval (Grazing incidence small angle x-ray scattering, GISAXS) laat toe om de morfologie van een ALD gegroeide lagen of nanostructuren te bestuderen.

XRD
: X-stralen diffractie (X-ray diffraction, XRD) wordt gebruikt om kristallijne materialen te bestuderen. Daarom is het gebruik van XRD als *in situ* techniek tijdens ALD gelimiteerd tot specifieke processen waarbij (poly-) kristallijne materialen worden afgezet.

XRF
: X-stralen fluorescentie (X-ray fluorescence, XRF) is een spectroscopische techniek die toelaat om de samenstelling van een ALD gegroeide laag te bestuderen en om veranderingen in de hoeveelheid afgezet materiaal met een submonolaag precisie op te volgen.

XAS (in vacuo)
: X-stralen absorptie spectroscopie (X-ray absorption spectroscopy, XAS) laat toe om de locale atomaire omringing binnenin een materiaal te bestuderen.

XPS (in vacuo)
X-stralen fotoelectron spectroscopie (X-ray photoelectron spectroscopy, XPS) kan gebruikt worden om de chemische samenstelling en chemische bindingstoestand binnenin een materiaal te onderzoeken.

In hoofdstuk 5, 7 en 8 wordt geïllustreerd hoe deze *in situ* synchrotron gebaseerde x-stralen technieken een nieuwe set van nuttige hulpmiddelen vormen bij het onderzoek van ALD processen.

Deel II: Inkapseling van Quantum Dots via ALD

Het gebruik van *In situ* XRF and GISAXS wordt verder toegelicht aan de hand van een studie van de inkapseling van quantum dots (QDs) en de bijhorende interacties tussen de ALD precursoren en het oppervlak van de QDs.

De ALD inkapseling van een monolaag CdSe/CdS/ZnS QDs wordt als een model systeem gebruikt. We bestuderen zowel de inkapseling van deze QDs in ZnO, Al_2O_3 and TiO_2. Elk van deze ALD processen interageert op een verschillende manier met het QD-oppervlak. Dit leidt tot verschillen in de eigenschappen van de uiteindelijke QD structuur. Hieronder worden de belangrijkste verschillen toegelicht.

ZnO inkapseling
Het gebruik van *in situ* XRF toont aan dat de ZnO groei op as-deposited QDs wordt verhinderd. Deze groei kan echter gestart worden door de QDs voordien aan TMA bloot te stellen. De *In situ* XRF toont aan dat deze voorbehandeling gepaard gaat met een reductie van het aanwezige Zn in de QDs. Deze reductie kan worden toegewezen aan een Al-Zn kation uitwisseling aan het QD oppervlak. Hierbij wordt ongeveer een derde van het aanwezige Zn vervangen door Al. Deze oppervlakte reactie zorgt ervoor dat de ZnO groei op het QD oppervlak kan starten. Deze uitwisseling geeft echter een afname van de fotoluminescentie tot gevolg. De *In situ* GISAXS data toont verder aan dat de originele hexagonale ordening binnenin de QD-laag blijft bewaard. Daarnaast bevestigt de GISAXS data het met XRF waargenomen nucleatie gedrag.

TiO_2 inkapseling
In situ XRF en GISAXS werden opnieuw gebruikt om het nucleatie gedrag van het ALD proces tijdens TiO_2 inkapseling te bestuderen. Ondanks een kleine nucleatie periode leidt het TDMAT/H_2O proces tot een uniforme en conformele bedekking van de QD-laag. Op basis van de *in situ* XRF gegevens kunnen we verder besluiten dat de QDs tijdens het ALD proces niet worden aangetast. Tijdens TiO_2 inkapseling wordt niet alleen de originele fotoluminescentie bewaard, maar wordt er zelfs een toename waargenomen in de quantum efficiëntie.

Al_2O_3 inkapseling

In situ GISAXS toont aan dat tijdens Al_2O_3 inkapseling geen nucleatie vertraging aanwezig is. Het inkapselings proces veroorzaakt echter een significante daling in de fotoluminescentie van de QD-laag. De *In situ* XRF data biedt hier een unieke kijk op de oppervlakte reactie die aan de basis ligt van deze reductie. Vergelijkbaar met de gebruikte voorbehandeling tijdens ZnO inkapseling, zien we een daling van de hoeveelheid Zn aanwezig in de QD-laag tijdens de eerste ALD cycli. Indien we de quantum efficiëntie willen bewaren, kunnen we gebruik maken van een dunne TiO_2 laag. Deze dunne laag geeft een positieve invloed op de fotoluminiscentie en beschermt de QDs voldoende van het daaropvolgende Al_2O_3 depositie proces.

Het gebruik van *in situ* XRF en GISAXS laat ons toe om de belangrijke interactie tussen de reactieve ALD gassen en het oppervlak van de QDs beter te begrijpen. Dit leert ons dat de keuze van een inkapselings proces niet alleen mag bepaald worden op basis van de beoogde materiaal eigenschappen, er moet ook rekening worden gehouden met de verschillen in reactie mechanisme van de ALD processen en de interactie tussen de ALD precursoren en het oppervlak van de QDs. Een belangrijke conclusie van dit werk is dat het standaard ALD proces, namelijk ALD depositie van Al_2O_3, niet de optimale keuze is voor inkapseling en dat TiO_2 tot betere resultaten leidt.

In dit werk wordt aangetoond dat het gebruik van *in situ* synchrotron gebaseerde x-stralen technieken toelaat om bepaalde specifieke aspecten van ALD processen te bestuderen die via meer conventionele methodes niet bereikbaar zijn. In het bijzonder hebben we *in situ* XRF en GISAXS gebruikt om de ALD inkapseling van QDs te bestuderen. Kortom, *in situ* synchrotron gebaseerde x-stralen technieken kunnen worden beschouwd als een nieuwe toolbox met analyse technieken die de komende jaren tot veel nieuwe inzichten kunnen leiden in het ALD onderzoek.

Table of Contents

List of Acronyms

AAO	Anodized Alumina
AFM	Atomic Force Microscopy
ALD	Atomic Layer Deposition
ALE	Atomic Layer Epitaxy
BNL	Brookhaven National Laboratory
CVD	Chemical Vapor Deposition
DEZ	Diethyl Zinc
DWBA	Bistorted wave born approximation
EM	Electromagnetic
EXAFS	Extended X-ray absorption fine structure
EDX	Energy Dispersive X-ray Spectroscopy
FFT	Fast Fourier Transform
FTIR	Fourier transform infrared spectroscopy
FWHM	Full Width Half Maximum
GISAXS	Grazing Incidence Small Angle X-ray Scattering
GPC	Growth per cycle
HI	Hot Injection
HR-TEM	High-resolution transmission electron microscopy
LB	Langmuir-Blodgett
ML	Monolayer
$MeCpPtMe_3$	(methylcyclopentadienyl)trimethyl Platinum
MWCNT	Multi walled carbon nanotubes
NSLS	National Synchrotron Light Source
OES	Optical Emision Spectroscopy
PEALD	Plasma-Enhanced Atomic Layer Deposition
PECVD	Plasma-Enchanced Chemical Vapor Deposition
PL	Photoluminescence
PV	Photovoltaic
PVD	Physical Vapor Deposition
QCM	Quartz Crystal Microbalance
QD	Quantum dot
QDs	Quantum dots
QMS	Quadrupole mass spectrometry
SE	Spectroscopic Ellipsometry
SEM	Scanning Electron Microscopy
SILAR	Successive ion layer adsorption and reaction

SPA	Surface photoabsorption
TDMAT	Tetrakis(dimethylamino) Titanium
TEM	Transmission Electron Microscopy
TEMAH	Tetrakis(ethylmethylamino) Hafnium
TMA	Trimethyl Aluminum
UHV	Ultra-high vacuum
XANES	X-ray absorption near edge structure
XAS	X-ray Absorption Spectroscopy
XPS	X-ray Photoelectron Spectroscopy
XRD	X-ray Diffraction
XRF	X-ray Fluorescence
XRR	X-ray Reflectivity

1 Introduction

1.1 Brief Introduction to Atomic Layer Deposition

Atomic Layer Deposition(ALD) is a thin film deposition technique. During deposition, the surface gets sequentially exposed to different reactant gases. These are chosen to react in a self-limiting way. This results in the growth of a (sub-) monolayer of material during each ALD step. [1, 2]

The ALD concept was first developed during the 1960's in the USSR, but it was only in the 1970s that the technique was developed further by Dr. Tuomo Suntola in Finland for scientific and industrial use. [2–4] ALD (or atomic layer epitaxy (ALE) as it was then known) saw its first application in the manufacturing of electroluminescent (TFEL) flat-panel displays in the 1980s. [4] During the 1990s en 2000s the interest from the microelectronics industry in ALD increased, as ALD proved to be an effective tool to deposit high-k materials. This resulted, for example, in the integration of an ALD step in the 45 nm node CMOS technology by Intel. [5] Currently, a wide variety of ALD processes has been developed for the depostion of oxides, nitrides, sulfides and metals. These are used for a wide range of application, e.g. in catalysis [6–10], sensors [11], fuel cells [12–15] and photovoltaics [16–18].

To illustrate the basic working principle of ALD, we will briefly discuss the most simple and widely used ALD process, the thermal growth of Al_2O_3. As already mentioned, an ALD process typically consists of the sequential exposure of a surface to reactant gases (see Fig 1.1). In the case of the growth of Al_2O_3, we

use trimethyl aluminum (TMA) and water. Usually a silica starting surface is used. Silica is typically terminated by hydroxyl groups (OH). One ALD cycle consists of four steps. In a first step, we expose the surface to TMA. A surface reaction will take place between the hydroxyl groups and the TMA molecules. In this process, the TMA will be bound to the surface by forming a bond between the oxygen atom from a hydroxyl group and the aluminum from the TMA. The hydrogen and one of the methyl ligands get removed as methane. This is a self limiting reaction, as the reaction will halt when all hydroxyl groups have been consumed. The unreacted TMA molecules and the formed methane are then removed from the reaction chamber during a purge or pump step. In a third step, the surface is exposed to water. The water will react with the remaining methyl ligand on the surface. This recreates surface hydroxyl groups and removes the ligands under the form of methane. This is again a self limiting reaction, as the reaction will only occur while methyl ligands remain on the surface. In the final step, the residual water and the formed methane are removed. After these four steps, a (partial) monolayer of Al_2O_3 is formed and due to the hydroxyl surface termination, a new ALD cycle can be started.

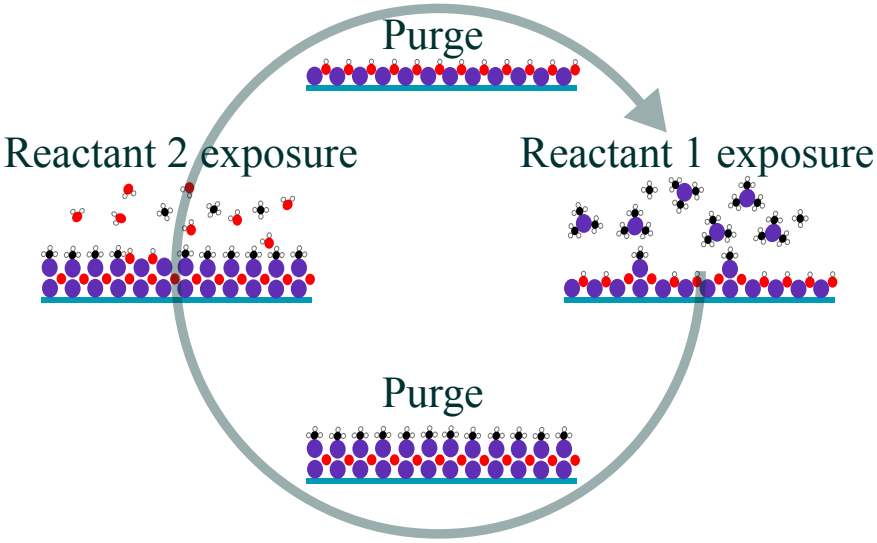

Figure 1.1: Schematic representation of the basic principle of ALD. A typical ALD cycle is shown consisting of the sequential exposure to a first reactant (e.g. TMA), purging of the chamber of byproducts and unreacted precursor molecules, exposure to a second reactant(e.g. water) and a second purging of the chamber. After this ALD cycle a (sub-)monolayer of material has been deposited.

By choosing the number of ALD cylces, a very exact thickness of Al_2O_3 can be targeted. The thermal Al_2O_3 ALD process at a temperature of 200°C has a growth rate of about 1 Å/cycle. In this case the activation energy for the surface reactions is provided by the temperature of the substrate, making this a thermal ALD process. Other processes exist, that use a plasma excitation of the gas during one or both reactant steps. In this case, part of the energy is provided by the radicals of the plasma. These processes are denoted as plasma-enhanced ALD (PEALD) processes.

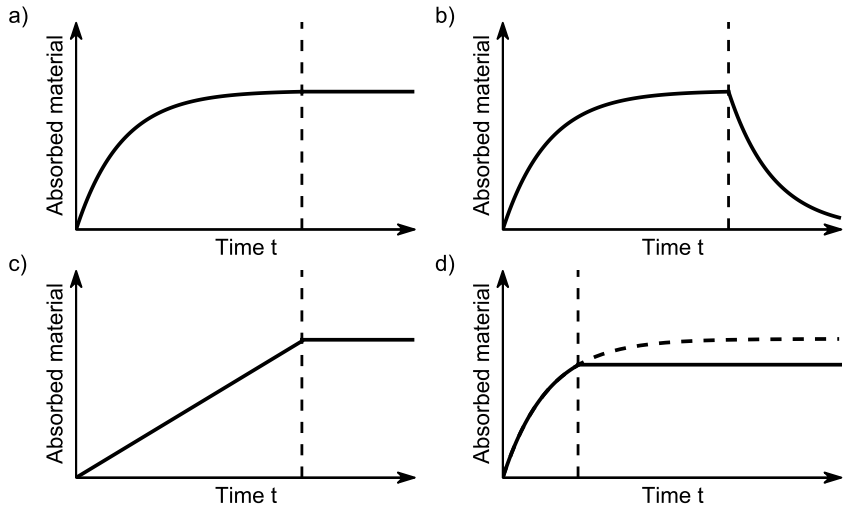

Figure 1.2: Classification of gas-solid surface reactions, based on the amount of adsorbed material. (a) irreversible saturating adsorption or self-limiting reaction, (b) reversible saturating adsorption, (c) irreversible non-saturating adsorption or deposition and (d) irreversible saturating adsorption not allowed to saturate. The dotted vertical line indicates the end of the reactant exposure and the start of the following purge step.

The ALD process heavily relies on the self-limiting nature of each reaction during each ALD step. Gas-solid surface reactions can be classified into different classes based on the amount of material adsorbed over time. In figure 1.2 the relevant cases are depicted. Saturation is the first condition for a good ALD reaction. However both reversible (Fig 1.2(a)) and irreversible (Fig 1.2(b)) reactions can saturate. In order to have a true self-limiting process, usable for ALD, the adsorbed material may not desorb from the surface during the purge step. This limits possible reactions to irreversible adsorption on the time scale of the experiment. Since physisorption is always reversible, ALD reactions are always chemisorption reactions. The ALD process also needs to take care that the chemisorption reaction

has enough time to saturate. If the exposure time during an ALD step is to short, the amount of adsorped material will be lower and this will lead to a lower growth per cycle (see Fig 1.2(d)).

Generally, an ALD process will only be self-limiting within a certain temperature range. This temperature range, the so called ALD window, is defined by the temperatures in between both ALD steps are self-limiting as can be seen in figure 1.3. It should be noted that within the ALD window, the GPC can still vary due to differences in equilibrium states during each half cycle. Below this ALD window, the growth per cycle can be higher, due to condensation (non-saturating reaction, see Fig 1.2(c)) or lower, due to lower reactivity (not saturated reaction, see Fig 1.2(d)). Similarly, at too high temperature, the growth per cycle can be higher due to decomposition (non-saturating reaction, see Fig 1.2(c)) or to low due to desorption (reversible adsorption, see Fig 1.2(b)).

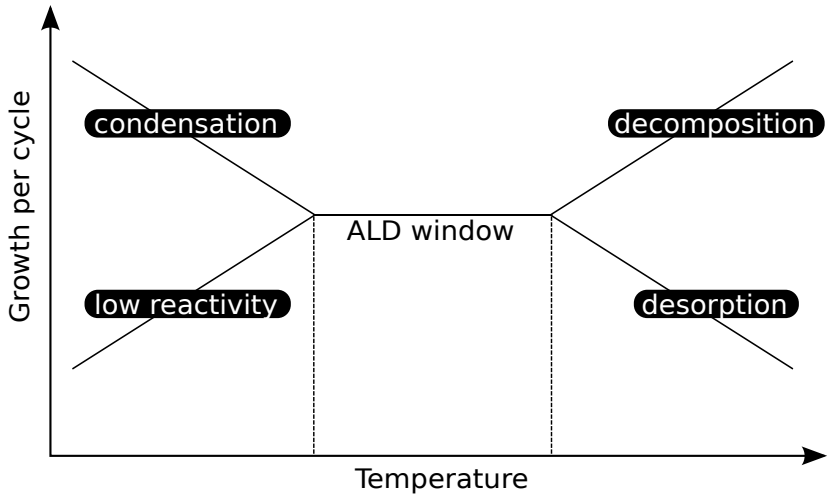

Figure 1.3

Due to the specific reaction path, ALD has several advantages over other film deposition techniques. The main advantage is the control of the film thickness at the Ångstrom level. A second advantage results from the self limiting nature of ALD. This allows the conformal coating of high aspect ratio structures. A last advantage is the chemical selectivity. As growth will only occur on areas terminated with the right surface groups, area selective growth can be achieved. The major drawback of ALD is the relatively slow deposition rate, limiting practical applications to the 1Å-1 μm layer-thickness range.

1.2 Goals and Outline of This Thesis

This thesis is divided into two main parts. In the first part, the focus is on the introduction of various synchrotron based x-ray techniques and their corresponding possibilities in ALD research. The second part focuses on the study of the ALD encapsulation of quantum dots, illustrating the use of synchrotron based x-ray techniques, to obtain information that would otherwise not be accessible using conventional techniques. This thesis is article-based. The results are presented as reformatted papers that have been published in or will be submitted to peer-reviewed journals. Introduction and framing is added, preceding the relevant chapter(s).

In chapter 2, a few experimental aspects are discussed. This should provide the reader with all the basic information needed to tackle the following chapters. Part I consists of chapter 3, 4 and 5. In chapter 3, a brief introduction is given to *in situ* characterization during ALD. The chapter finishes with a short introduction to synchrotron light sources (section 3.3). The following chapter, chapter 4, is based on a review article, published in Journal of Vacuum Science & Technology A. A broad introduction is given concerning the various possibilities when using synchrotron based x-rays. The chapter is intended as a tutorial review of in situ x-ray techniques as monitoring tool during ALD. The chapter will first introduce scattering based techniques, XRR and GISAXS, followed by x-ray diffraction and conclude with a discussing of x-ray based elemental analysis using XRF and XPS. At the end of the chapter, some practical considerations are mentioned on performing ALD experiments at synchrotron facilities.

Chapter 5, is based on a letter, published in Applied Physics Letters. In situ XRF and GISAXS are demonstrated as tools to study the initial growth of HfO_2 on Si and Ge substrates. This enables a detailed characterization of the evolution of amount of deposited material and the evolution of surface roughness during the very first ALD cycles.

Part II consists of chapter 6, 7 and 8. This second part focuses on the use of *in situ* synchrotron based x-ray techniques to study the encapsulation of quantum dots. In chapter 6 a brief introduction is given to the field of quantum dots, next to a discription of the specific quantum dots used in this work. At the end of the chapter, a brief overview is given of the known literature combining ALD and quantum dots.

In chapter 7 the encapsulation CdSe/CdS/ZnS core/shell/shell QDs in a ZnO matrix is studied in detail. *in situ* XRF and GISAXS are used to gain insight in the interaction between the QDs and the ALD precursors and the resulting metal oxide coating. The use of these *in situ* techniques allows us to show the inhibition of ZnO growth on as-deposited QDs. The growth can however be triggered by exposing the QDs to a single pulse of TMA. Accuracy of the *in situ* XRF enables us to

identify an Al-for-Zn cation exchange at the QD surface, involving the substitution of approximately one third of the original Zn by Al. This in turn causes a reduction of the photoluminescence quantum yield. *In situ* GISAXS is used to study the ordering of the QDs and monitor changes during the encapsulation process. These measurements uncover an important interplay between the highly reactive ALD precursors and the QD surface.

In the subsequent chapter, chapter 8, the encapsulation of the same QDs is attempted by ALD of Al_2O_3 and TiO_2. Here a distinctive difference can be found in the photoluminescence response after encapsulation. We employ *in situ* XRF and GISAXS to study the difference in nucleation behavior and surface interaction during the start of the encapsulation process. This again points to an important difference in precursor chemistry. Here we show that the widely used ALD process for Al_2O_3 growth is not always the optimal choice, even-tough Al_2O_3 encapsulation is often considered as a universal solution to all encapsulation problems within the ALD community.

In the final chapter, chapter 9, the main results from this work are summarized and I offer my outlook on some of the future possibilities these results my lead into.

The following papers are included in this thesis.

Paper I **In situ synchrotron based x-ray techniques as monitoring tools for atomic layer deposition. (Chapter 4)**
Devloo-Casier K., Ludwig K. F., Detavernier C., & Dendooven J.
Journal of Vacuum Science & Technology A: Vacuum, Surfaces, and Films, 32(1), 010801.(2014)
http://doi.org/10.1116/1.4851716

Paper II **In situ synchrotron based x-ray fluorescence and scattering measurements during atomic layer deposition: Initial growth of HfO_2 on Si and Ge substrates. (Chapter 5)**
Devloo-Casier K., Dendooven J., Ludwig K. F., Lekens G., D'Haen J., & Detavernier C.
Applied Physics Letters, 98(23), 231905. (2011)
http://doi.org/10.1063/1.3598433

Paper III **A case study of ALD encapsulation of quantum dots: embedding supported CdSe/CdS/ZnS quantum dots in a ZnO matrix. (Chapter 7)**
Devloo-Casier K., Geiregat P., Ludwig K. F., van Stiphout K., Vantomme A., Hens Z., Detavernier C., Dendooven J.
Manuscript in preparation.

Paper IV **ALD encapsulation of supported CdSe/CdS/ZnS nanocrystals in a metal oxide matrix: TiO_2 vs Al_2O_3 (Chapter 8)**
Devloo-Casier K., Geiregat P., Ludwig K. F., van Stiphout K., Vantomme A., Rijckaert H., Van Driessche I., Hens Z., Detavernier C., Dendooven J.
Manuscript in preparation.

References

[1] S. M. George. *Atomic Layer Deposition: An Overview.* Chemical reviews, 110(1):111–31, jan 2010.

[2] R. L. Puurunen. *Surface Chemistry of Atomic Layer Deposition: A Case Study for the Trimethylaluminum/Water Process*. Journal of Applied Physics, 97(12):121301, 2005.

[3] A. Shevjakov, G. Kuznetsova, and V. Aleskovskii. In Chemistry of High-Temperature Materials, Proceedings of the Second USSR Conference on High-Temperature Chemistry of Oxides, Leningrad, USSR, 2629 November 1965, pages 149–155, 1987.

[4] T. Suntola. *Method for Producing Compound Thin Films*, November 15 1977. US Patent 4,058,430.

[5] K. Mistry, C. Allen, C. Auth, B. Beattie, D. Bergstrom, M. Bost, M. Brazier, M. Buehler, A. Cappellani, R. Chau, C. Choi, G. Ding, K. Fischer, T. Ghani, R. Grover, W. Han, D. Hanken, M. Hattendorf, J. He, J. Hicks, R. Huessner, D. Ingerly, P. Jain, R. James, L. Jong, S. Joshi, C. Kenyon, K. Kuhn, K. Lee, H. Liu, J. Maiz, B. Mcintyre, P. Moon, J. Neirynck, S. Pae, C. Parker, D. Parsons, C. Prasad, L. Pipes, M. Prince, P. Ranade, T. Reynolds, J. Sandford, L. Shifren, J. Sebastian, J. Seiple, D. Simon, S. Sivakumar, P. Smith, C. Thomas, T. Troeger, P. Vandervoorn, S. Williams, and K. Zawadzki. *A 45 Nm Logic Technology With High-K Plus Metal Gate Transistors, Strained Silicon, 9 Cu Interconnect Layers, 193 Nm Dry Patterning, and 100% Pb-Free Packaging*. 2007 IEEE International Electron Devices Meeting, pages 247–250, 2007.

[6] P. C. Stair, C. Marshall, G. Xiong, H. Feng, M. J. Pellin, J. W. Elam, L. Curtiss, L. Iton, H. Kung, M. Kung, and H.-H. Wang. *Novel, Uniform Nanostructured Catalytic Membranes*. Topics in Catalysis, 39(3-4):181–186, oct 2006.

[7] J. Li, X. Liang, D. M. King, Y.-B. Y.-B. Jiang, and A. W. Weimer. *Highly Dispersed Pt Nanoparticle Catalyst Prepared by Atomic Layer Deposition*. Applied Catalysis B: Environmental, 97(1-2):220–226, jun 2010.

[8] Y. Zhou, D. M. King, X. Liang, J. Li, and A. W. Weimer. *Optimal Preparation of Pt/TiO2 Photocatalysts Using Atomic Layer Deposition*. Applied Catalysis B: Environmental, 101(1-2):54–60, nov 2010.

[9] C. Detavernier, J. Dendooven, S. P. Sree, K. F. Ludwig, and J. A. Martens. *Tailoring Nanoporous Materials by Atomic Layer Deposition.* Chemical Society reviews, 40(11):5242–53, dec 2011.

[10] E. Verheyen, S. Pulinthanathu Sree, K. Thomas, J. Dendooven, M. De Prins, G. Vanbutsele, E. Breynaert, J.-P. Gilson, C. E. A. Kirschhock, C. Detavernier, and J. A. Martens. *Catalytic Activation of OKO Zeolite With Intersecting Pores of 10- And 12-Membered Rings Using Atomic Layer Deposition of Aluminium*. Chemical Communications, 50(35):4610, 2014.

[11] H. Kim, H.-B.-R. Lee, and W.-J. Maeng. *Applications of Atomic Layer Deposition to Nanofabrication and Emerging Nanodevices*. Thin Solid Films, 517(8):2563–2580, feb 2009.

[12] Y. Chen, J. Wang, X. Meng, Y. Zhong, R. Li, X. Sun, S. Ye, and S. Knights. *Atomic Layer Deposition Assisted Pt-SnO2 Hybrid Catalysts on Nitrogen-Doped CNTs With Enhanced Electrocatalytic Activities for Low Temperature Fuel Cells*. International Journal of Hydrogen Energy, 36(17):11085–11092, 2011.

[13] E. Balee, A. Ringuedé, M. Cassir, M. Putkonen, L. Niiniso, E. Ballee, A. Ringuede, M. Cassir, M. Putkonen, and L. Niinisto. *Synthesis of a Thin-Layered Ionic Conductor, CeO2 Y2O3, by Atomic Layer Deposition in View of Solid Oxide Fuel Cell Applications*. Chemistry of Materials, 21(19):4614–4619, oct 2009.

[14] X. Jiang and S. F. Bent. *Atomic Layer Deposition of Platinum for Solid Oxide Fuel Cells*. ECS Transactions, 3(15):249–259, 2007.

[15] J. H. Shim, C.-C. Chao, H. Huang, and F. B. Prinz. *Atomic Layer Deposition of Yttria-Stabilized Zirconia for Solid Oxide Fuel Cells*. Chemistry of Materials, 19(15):3850–3854, jul 2007.

[16] J. W. Elam, A. B. F. Martinson, M. J. Pellin, and J. T. Hupp. *Atomic Layer Deposition of In2O3 Using Cyclopentadienyl Indium: A New Synthetic Route to Transparent Conducting Oxide Films*. Chemistry of Materials, 18(15):3571–3578, jul 2006.

[17] P. Poodt, A. Lankhorst, F. Roozeboom, K. Spee, D. Maas, and A. Vermeer. *High-Speed Spatial Atomic-Layer Deposition of Aluminum Oxide Layers for Solar Cell Passivation.* Advanced materials, 22(32):3564–7, aug 2010.

[18] J. A. van Delft, D. Garcia-Alonso, and W. M. M. Kessels. *Atomic Layer Deposition for Photovoltaics: Applications and Prospects for Solar Cell Manufacturing*. Semiconductor Science and Technology, 27(7):074002, jul 2012.

2 Experimental Methods

In this chapter experimental aspects related to the research performed for this thesis are summarized. In section 2.1 some details are given concerning the used ALD processes. This includes a description of the used ALD setups in section 2.1.1 and some experimental details on the used processes and substrates in section 2.1.2 and 2.1.3.

2.1 Depostion by Atomic Layer Deposition

2.1.1 ALD Setup

The data presented in the following chapters are the result of ALD experiments performed both at Ghent University and Brookhaven National Lab. The following sections will briefly introduce both setups.

2.1.1.1 ALD Setup at Ghent University

The ALD experiments at Ghent University were carried out in a home built ALD reactor, known within the lab as ALD III (see Fig. 2.1). The main chamber consists of a heated stainless steel vessel. The chamber walls are heated to 95 °C to avoid condensation of precursor vapors. The ALD chamber is continuously being pumped, using a turbomolecular pomp, allowing a base pressure in the 10^{-7} mbar range. A loadlock is connected to the main chamber, allowing the transfer of samples, without breaking the vacuum of the main chamber. The samples are

transfered from the loadlock, to a heated sample stage inside the main chamber. Sample temperature is PID controlled and can be set to a maximum of 400 °C. Various gases (e.g. O_2 and N_2) and precursor vapors can be admitted to the chamber, using computer controlled pneumatic valves. The chamber is also equipped with a remotely placed radio frequency (RF) inductively coupled plasma (ICP) source, allowing the generation of an inductively coupled plasma. The power is provided using a CESAR 136 RF power generator, operating at 13.56 MHz. This makes the chamber suitable for both thermal ALD and plasma-enhanced ALD. Various viewports and access flanges are available on the chamber, allowing in situ measurements like spectroscopic ellipsometry (SE), infrared spectroscopy (FTIR) and mass spectroscopy. The various windows, quartz for SE and KBr for FTIR, are protected by valves during precursor exposures to prevent deposition.

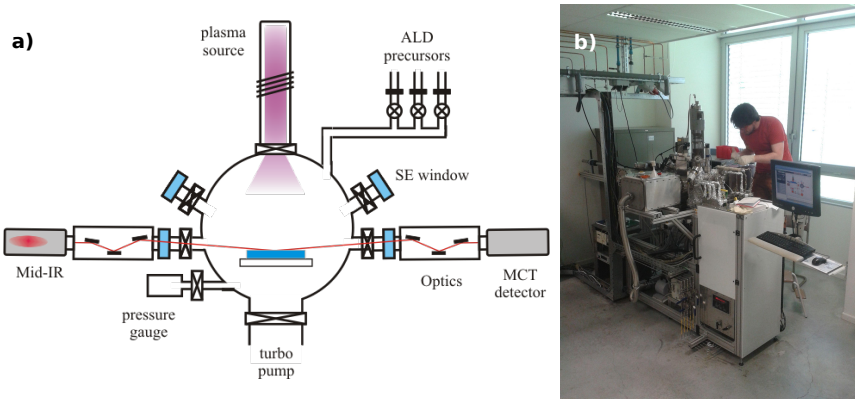

Figure 2.1: (a) Schematic representation of ALD III, showing the basic design and in situ measurement possibilities. (b) Photograph of ALD III in the ALD lab of CoCooN at Ghent University.

2.1.1.2 ALD Setup at Brookhaven National Lab

The in situ synchrotron based x-ray experiments, presented in the following chapters, have been performed in the UHV thin film growth facility installed at beamline X21 of the National Synchrotron Light Source at Brookhaven National Laboratory. [1] This setup consists of a stainless steel reaction chamber pumped by a turbo molecular pump to a base pressure of 10^{-6} mbar (see Fig 2.2). Samples can be introduced via a loadlock and are mounted vertically in front of a resistive heating plate. The chamber is equipped with an entrance beryllium window for the transmission of the x-rays provided by the synchrotron, and two exit beryllium windows for the transmission and detection of the reflected, scattered and fluorescent x-rays from the sample. The x-ray beam was defined to have a width

of 1 mm in the lateral and 0.5 mm in the transversal direction. A Vortex silicon drift detector mounted perpendicular to the sample surface is available to collect the fluorescence, while 2D scattering intensity maps can be recorded using a Dectris, Pilatus 100k, 2D area detector. The whole chamber is mounted on a rotatable table, to allow tuning of the incidence angle to fit the experiment.

A collaboration with the group of Prof. Karl Ludwig (Boston University) allowed us to have access to this setup and, more importantly, allowed us to adapt this setup to enable thermal ALD. Enabling thermal ALD of oxides required, amongst other things, the connection of precursor supply lines. The delivery lines were equipped with needle valves and pneumatic valves to control the gas flow into the reactor. A small home built controller was used to control the various pneumatic valves during an ALD process. All unnecessary parts were removed, both to protect them from ALD coating and to avoid having any dead volume, that can trap gases. To avoid condensation of the precursors, the delivery lines and chamber walls were heated to 60°C and 80°C, respectively.

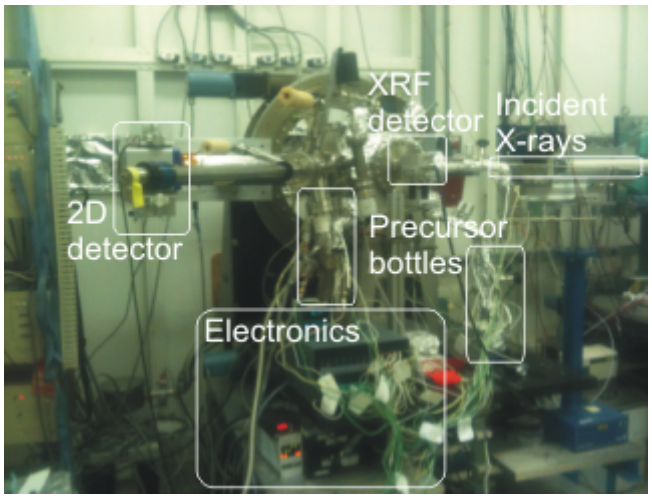

Figure 2.2: (Photograph of the UHV film growth facility, adapted for thermal ALD, installed at beamline X21 of the National Synchrotron Light Source at Brookhaven National Laboratory.

2.1.2 ALD Processes

The experiments included in this thesis are mostly limited to experiments involving thermal ALD process due to the incompatibility of the setup at X21 with PEALD. Al_2O_3, TiO_2, ZnO, HfO_2 and Pt are grown using the following organometallic precursors as metal source:

- trimethyl aluminum (TMA, $Al(CH_3)_3$)
- diethyl zinc (DEZ, $Zn(C_2H_5)_2$)
- tetrakis(dimethylamino) titanium (TDMAT, $Ti(N(CH_3)_2)_4$)
- tetrakis(ethylmethylamino) hafnium (TEMAH, $Hf(N(CH_3)(C_2H_5))_4$)
- (methylcyclopentadienyl)trimethyl platinum ($MeCpPtMe_3$, $C_5H_4CH_3Pt(CH_3)_3$)

The chemical structure of these molecules is shown in figure 2.3. All ALD processes to deposit metal oxides use water as a reactant gas. To deposit Pt, ozone is used as a reactant gas. [2]

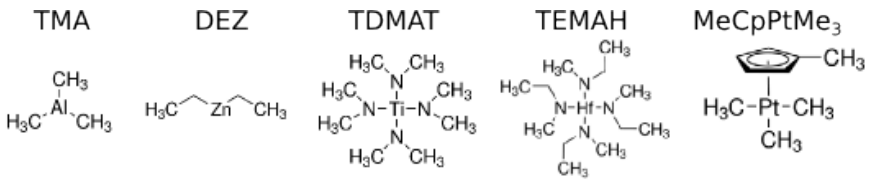

Figure 2.3: Chemical structure of the organometallic precursors used in this work.

2.1.3 Substrate Preparation

A wide variety of substrates has been used in this work. All substrates were placed in the reactor suffciently in advance of deposition, in order to achieve a stable sample temperature and allow degassing of porous materials. In chapter 4 most experiments were performed using SiO_2 (RCA cleaned Si) as starting surface. Some examples included large surface area substrates, MWCNTs and anodized alumina (AAO), for XRF experiments. In chapter 5, HfO_2 growth on Si based substrates (H-terminated Si and RCA cleaned Si) and Ge based substrates (H-terminated Ge and PECVD grown GeO_2) is compared. In chapter 7 and 8, the focus is on ALD encapsulation of quantum dots. Details for these starting systems can be found in section 6.1.2.

References

[1] G. Ozaydin, A. S. Ozcan, Y. Wang, K. F. Ludwig, H. Zhou, R. L. Headrick, and D. P. Siddons. *Real-Time X-Ray Studies of Mo-Seeded Si Nanodot Formation During Ion Bombardment*. Applied Physics Letters, 87(16):163104, 2005.

[2] J. Dendooven, R. K. Ramachandran, K. Devloo-Casier, G. Rampelberg, M. Filez, H. Poelman, G. B. Marin, E. Fonda, and C. Detavernier. *Low-Temperature Atomic Layer Deposition of Platinum Using (Methylcyclopentadienyl)trimethylplatinum and Ozone*. The Journal of Physical Chemistry C, 117(40):20557–20561, oct 2013.

Part I

X-ray Techniques for In Situ Monitoring of ALD

3

Introduction to In Situ Characterization

3.1 Why use In Situ Characterization?

To start this chapter, let us have a look at, maybe, the most important question driving almost all the work in this thesis. *Why use in situ characterization methods to study ALD?* This question can be answered both from a practical point of view and a more fundamental point of view.

From a practical point of view, in situ characterization provides a gain in time. ALD is a rather slow deposition technique. For example, when characterizing or optimizing an ALD process, a large amount of test depositions is needed. When, however in situ techniques, like spectroscopic ellipsometry are used, the influence of various parameters can be checked during a single ALD experiment. This greatly reduces the total deposition time needed to optimize an ALD process.

From a more fundamental point of view, in situ characterization can provide an unique insight in ALD processes. Since the sample remains in vacuo during in situ measurements, surface contamination can be avoided. In situ characterization also offers the ability to monitor film properties and study the reaction mechanisms during ALD growth.

In short, in situ characterization offers the operator access to a wide range of information that would otherwise require a lot more experiments or would even be unattainable with ex situ post deposition analysis.

3.2 Standard Lab Based Techniques

In the setup used in Gent (see section 2.1.1.1) various in situ characterization methods are implemented. The easiest in situ characterization methods, are light based techniques, since they allow remote probing of the sample, without physical contact. The only requirement is entrance and exit windows, to allow the light to reach the sample. In the following section, two of the most commonly used techniques will be discussed, namely spectroscopic ellipsometry (SE) and infrared spectroscopy (FTIR).

3.2.1 Spectroscopic Ellipsometry

3.2.1.1 Introduction

Spectroscopic ellipsometry (SE) is an optical technique that measures the change in polarization of light reflected from a surface. [1] These changes in polarization can then be used to determine the thicknesses and optical constants of the thin films on a substrate. The changes in polarization are normally described in function of Ψ and Δ:

$$\rho = \frac{R_p}{R_s} = tan(\Psi)e^{i\Delta} \tag{3.1}$$

with ρ the complex ellipsometric parameter and R_p and R_s the complex Fresnel coefficients of the sample for p- (in the plane of incidence) and s- (perpendicular to the plane of incidence) polarized light, respectively. Here, tan(Ψ) is the amplitude ratio and Δ is the phase shift between both polarizations upon reflection. Normally the Ψ and Δ parameters are measured in a wide wavelength range (typically UV and/or visible light). These parameters have to be fitted to optical models to obtain the desired physical film properties. Here lies the weakness of the technique, since these optical models need to make certain assumptions about the material in order to be able to extract thickness information and other optical parameters.

To perform in situ SE, only three things are needed. First of all a light source and a polarizer to define the incoming light. Secondly, a polarization analyzer and detector unit to determine the polarization of the reflected light. And thirdly, entrance and exit windows (e.g. quartz) to allow the light to reach the sample in the ALD reactor. A schematic representation is shown in figure 3.1.

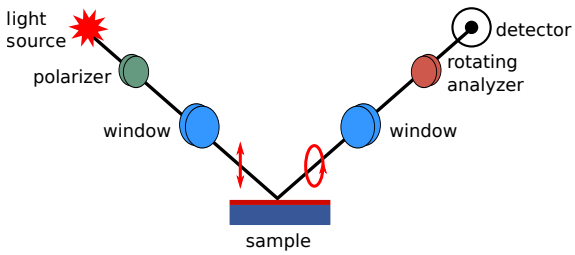

Figure 3.1: Schematic representation of a basic in situ ellipsometry system.

3.2.1.2 Example

A brief example will be discussed, in order to show the relevance of SE to ALD research. [2] As a typical example the growth of Al_2O_3 by thermal ALD, using trimethyl aluminum (TMA) and water, will be discussed. The SE measurements were carried out using a Woollam M2000U ellipsometer that was mounted on the ALD setup.

In Figure 3.2 the result from the in situ SE measurements during growth is shown. Both the Ψ and Δ parameters change during the film growth. When these parameters are fitted over the wide wavelength range, the thickness of the film can be obtained with a relatively high accuracy. The resulting thickness obtained after each ALD cycle clearly shows the nice linear thickness increase of the Al_2O_3 layer, due to the constant GPC of about 1.5 Å per cycle during the ALD process.

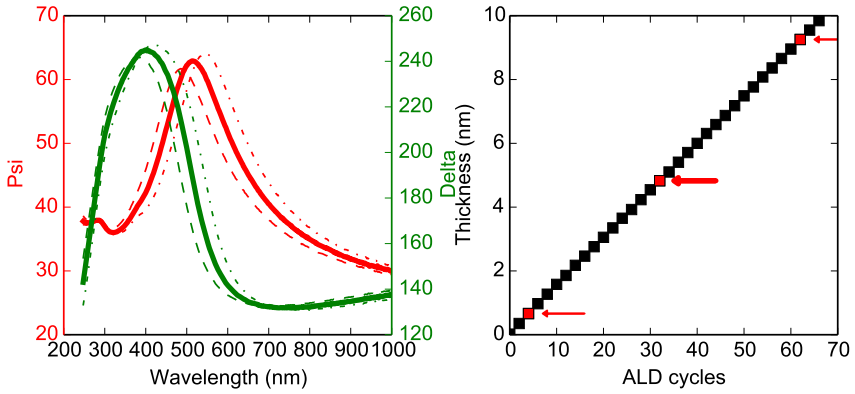

Figure 3.2: In situ SE measurement obtained during ALD growth of Al_2O_3. The left graph shows the raw Ψ and Δ parameters, as measured at 3 distinctive point during growth. The right graph shows the linear increase in film thickness as obtained from the optical SE model. The arrows show the corresponding thickness to the raw data on the left.

3.2.2 Infrared Spectroscopy

3.2.2.1 Introduction

Infrared spectroscopy is an optical technique that monitors the absorption of IR-light by materials. The energy of IR-light corresponds to the typical energy correlated with molecular vibrations. Usually the mid infrared range, spanning a wavenumber range from 4000 cm^{-1} to 400 cm^{-1} (or a wavelength range from 2.5 μm to 25 μm) is used to study the vibrations and associated rotational-vibrational structure in molecular bonds. Infrared spectroscopy has evolved from a technique to analyse gas or liquid samples to a real surface technique. This allows the study of chemical surface groups and the dynamics and kinetics of surface reactions. [3]

Infrared spectroscopy is usually denoted as fourier transformed infrared spectroscopy (FTIR) as most modern IR setups use an interferometer to measure an interferogram. This can be done very fast and by fourier transforming the interferogram, an absorption spectrum can be obtained over a wide wavenumber range. To study surfaces, a wide range of optical geometries are used and have been applied to ALD research. The classical and most simple geometry is a transmission measurement. Here the change in transmitted IR-light through the substrate and ALD film is measured. [4, 5] (see Fig. 3.3) A more surface specific geometry is used in attenuated total reflection (ATR) infrared spectroscopy. Here, an ATR crystal is chosen as the substrate and the IR-light is coupled into the crystal. By total internal reflection, the light is allowed to reflect at the internal surface. The corresponding evanescent wave will interact with the material deposited on the crystal. [6] A final geometry is used in infrared reflection absorption spectroscopy (IRRAS). In this case, the IR-light is reflected from the sample surface and the light will interact with the top surface, allowing the study of the ALD process. [7]

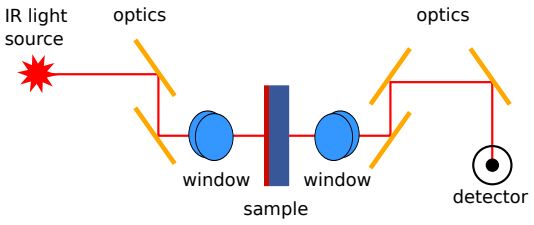

Figure 3.3: Schematic representation of an in situ FTIR setup in transmission geometry.

3.2.2.2 Example

Here we will again discuss the growth of Al_2O_3 by thermal ALD, using trimethyl aluminum (TMA) and water as a typical example of FTIR in ALD research. [8, 9] The results shown in figure 3.4 have been obtained by performing an FTIR measurement after each precursor exposure, using a Vertex 70v equiped with an MCT detector.

By comparing the IR absorption spectrum after precursor exposure to before the exposure, a difference spectrum can be obtained. The peaks and dips in this difference spectrum correspond, respectively, to the creation and removal of surface groups. In our example, we can clearly see that during the TMA exposure, hydroxyl groups get consumed and methyl groups are added, while during the water exposure hydroxyl groups get regenerated and the methyl groups are removed. This nicely corresponds to the known ligand-exchange reaction for the thermal Al_2O_3 ALD process.

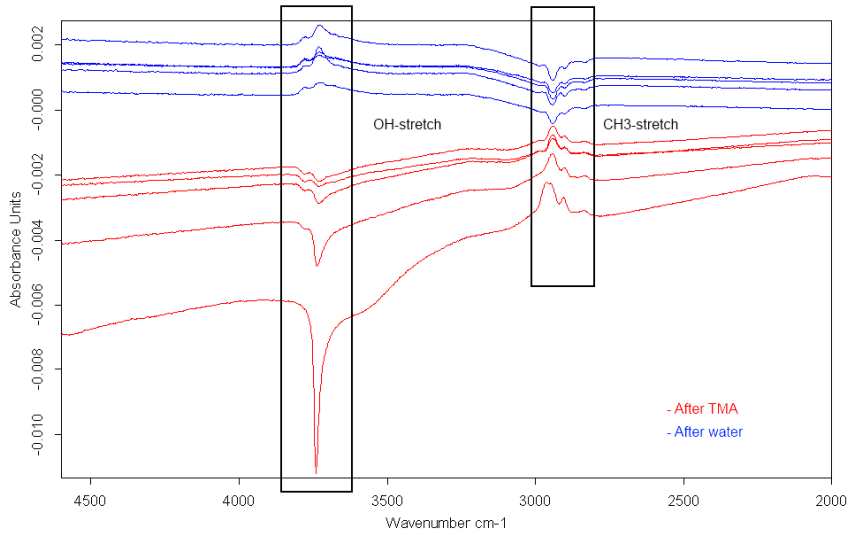

Figure 3.4: Difference spetra obtained during thermal ALD of Al_2O_3. The red and blue spectra correspond to the change in absorption during a TMA and water exposure respectively.

3.3 Introduction to Synchrotron Light Sources

In the previous sections, we introduced two light based characterization techniques, SE and FTIR. If we now expand the wavelength range from the UV and visible, used in SE, and the IR, used in FTIR, to the x-ray range, a large number of additional techniques become available. Most of these techniques need a high brilliance and energy tunability. These constrains are either inherent to the type of measurement (eg. XAS) or are desirable when performing in situ measurement.

Over the past decades, there has been a constant need for better x-ray sources, which is still ongoing today. In the following sections, we will briefly discuss the evolution of the x-ray source.

3.3.1 Early History and Discovery of X-rays

X-rays were first discovered by Wilhelm Röntgen in 1895. He labeled the new type of radiation as X-radiation, signifying an unknown type of radiation. The x-rays he created, were a byproduct of his experiments with electron discharge in an evacuated glass tube, known as a Geisler discharge tube. He noticed that when he placed his hand in between the tube and a fluorescent screen, he could see the bones inside his hand. This resulted in a worldwide sensation within weeks, as it was now possible to see the inside of the human body.

It was only in 1912, that x-rays become more than a medical party trick and the diffraction phenomena of crystalline matter were first studied by Max von Laue. A year later, William Lawrence Bragg and William Henry Bragg (father and son) formulated Bragg's law and laid the foundations of crystallography. It was only at this point, by interpreting diffraction patterns, that William Henry Bragg could unambiguously prove that x-rays are just a form of electromagnetic radiation with a short wavelength.

3.3.2 The Standard X-ray Tube and the Rotating Anode

The original x-ray source used by Röntgen remained the only practical source of x-rays for almost 20 years. The discharge tube, however, proved to be very tricky to operate in a reliable fashion. It was only when, in 1913, William D. Coolidge introduced the concept of using a glowing filament to produce electrons and subsequently accelerated them towards a water-cooled metal anode that a more reliable source became available. The operational power of these tubes was mainly limited by the cooling efficiency. The, so called, Coolidge tube became the standard x-ray source in the following decades and its working principles are still the basis of most modern lab based x-ray sources. People quickly realized that by rotating the anode, the heat could dissipate over a larger volume. It took, however until the 1960s before the first rotating anode sources were available, due to the difficulties

in producing a vacuum tight rotating shaft. This slightly increased the available x-ray intensities. The preceding sources are not only limited in intensity, but are also limited to specific x-ray energies. The most intense x-rays are produced in the anode by x-ray fluorescence. The energy of these x-rays corresponds to the Kα line of the anode material. The need for higher intensities and energy tunability was only met by the introduction of synchrotron sources.

3.3.3 A Synchrotron Light Source

A synchrotron light source is a source of EM-radiation produced by bending charged particles, moving at relativistic speeds, in a magnetic field. Synchrotron radiation was first observed as an unwanted side effect, when accelerating electrons in a synchrotron. The name stuck, even-tough currently, synchrotron radiation is mainly produced at specialized particle storage rings. Particles, usually electrons, are accelerated to relativistic speeds and then stored in a storage ring. Synchrotron radiation is generated as the electrons pass through bending magnets, needed to keep the electrons in a closed orbit, or insertion devices, wigglers and undulators, that are introduced in the straight sections of the storage ring. The produced x-rays are used in a wide range of experiments located in beamlines, along the storage ring (see Fig. 3.5).

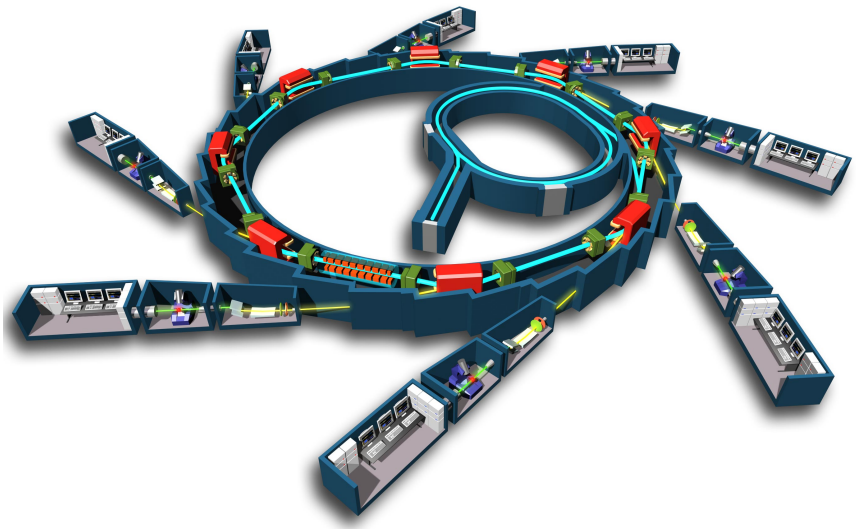

Figure 3.5: Schematical representation of a synchrotron light source. The center shows a linear accelerator and an accelerator ring, used to accelerated the electrons, before injection in the, outer storage ring. Along specific places of the ring, x-rays are generated and directed to beamlines. Courtesy of EPSIM 3D/JF Santarelli, Synchrotron Soleil.

Synchrotron light sources have a high brilliance, typically several orders of magnitude larger than a conventional x-ray source. Based on the x-ray optics available at the specific beamlines, the energy can be tuned over a wide range and a high level of monochromatization can be achieved. For certain measurements, high frequency x-ray pulses can be achieved, based on the bunching of electrons in the storage ring.

Synchrotron facilities are a very costly undertaking. Newest generation synchrotrons have a construction cost of several hundreds millions of euros (e.g. NSLS II construction cost US$912,000,000). They are, therefore, built by larger nations (e.g. USA and China) or as a collaboration between various countries (e.g. ESRF: European Synchrotron Radiation Facility). A map, showing all currently operated synchrotron facilities worldwide, is shown in figure 3.6.

Figure 3.6: Available synchrotron facilities worldwide. Courtesy of http://www.veqter.co.uk.

Currently, the free electron laser (FEL) is being explored as next step in x-ray generation. [10] At the moment a few FEL are being operated. These are slowly making experiments possible, that were previously not even conceivable using a synchrotron facility.

3.3.4 X-ray Source Brilliance

To compare the quality of various x-ray sources, the most commonly used quantity is the brilliance of the source. [11] Brilliance combines several important aspects in the source in one single measure, namely:

1. Number of photons emitted per second
2. Collimation of the beam (usually in milli-radians for both horizontal and vertical divergence)
3. Size of the source (usually in mm^2)
4. Spectral distribution (usually a fixed relative energy bandwidth (BW) of 1%)

This results in the following formula for the brilliance:

$$brilliance = \frac{photons/second}{(mrad)^2(mm^2\ source\ area)(0.1\%\ BW)} \tag{3.2}$$

Greater brilliance translates to a higher number of photons that can be concentrated in a spot. In figure 3.7 the rapid increase of the peak brilliance of x-ray sources over time is shown.

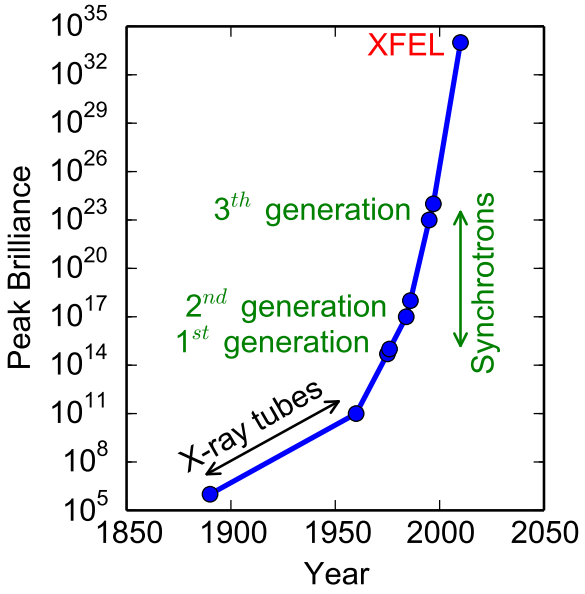

Figure 3.7: Evolution of the peak brilliance of x-ray sources over time.

3.4 This work

3.4.1 Characteristics of the X21 Beamline at NSLS

The synchrotron based experiments presented in this work were conducted at beamine X21 at the National Synchrotron Light Source (NSLS) in Brookhaven National Lab (BNL).* NSLS was a second generation synchrotron constructed in 1986 and decommissioned at the end of 2014. Beamline X21 housed two experimental stations. The first was devoted to the study of elastic x-ray scattering under high magnetic fields and the second focused on in-situ thin film growth. This latter station was adapted during our ALD studies. The hutch was located at a wiggler beam, delivering x-rays between 6 keV and 16 keV.

3.4.2 General Review of Synchrotron Based Techniques During ALD

In this work we aim to show the advantage of using a synchrotron light source, to perform in situ measurements during ALD. In chapter 4, a broad introduction will be given concerning the various possibilities when using synchrotron based x-rays. The chapter is intended as a tutorial review of in situ x-ray techniques as monitoring tool during ALD. The chapter will first introduce scattering based techniques, XRR and GISAXS, followed by x-ray diffraction and conclude with a discussion of x-ray based elemental analysis using XRF and XPS. At the end of the chapter, some practical considerations are mentioned on performing ALD experiments at synchrotron facilities.

3.4.3 Specific Applications Included in This Work

In the following text various applications of synchrotron based x-ray techniques will be discussed in detail. In chapter 5, in situ XRF and GISAXS are demonstrated as tools to study the initial growth of HfO_2 on Si and Ge substrates. This enables a detailed characterization of the evolution of amount of deposited material and the evolution of surface roughness during the very first ALD cycles.

In part II, in situ XRF and GISAXS will be further used as tools to study the encapsulation of quantum dots. These characterization methods will prove to provide information that would remain inaccessible using more conventional techniques.

*A detailed description of the beamline can be found at following location:
`http://beamlines.ps.bnl.gov/beamline.aspx?blid=X21`

3.4.4 Other Examples of Recent Synchrotron Experiments

As synchrotron-campagnes are team efforts and require close collaboration between all people involved, I was involved in various studies. These collaboration resulted in multiple publications which I co-authored (see also 9.2). These further illustrate the power of synchrotron based techniques during ALD . Therefor, some highlights are included with the references to the corresponding published work.

3.4.4.1 Atomic Layer Deposition of TiO_2 on Surface Modified Nanoporous Lowk Films [12]

The effects of different plasma treatments on low dielectric constant (low-k) materials influences growth behavior of ALD on these modified substrates. An O_2 and a He/H_2 plasma treatment were performed on SiCOH low-k films to modify their chemical surface groups. In situ X-ray fluorescence (XRF) was used to characterize ALD growth of TiO_2 on these substrates. The initial growth of TiO_2 was found to be inhibited in the original low-k film containing only $Si\text{-}CH_3$ surface groups, while immediate growth was observed in the hydrophilic O_2 plasma treated film. For the He/H_2 plasma treated film, containing both Si-OH and $Si\text{-}CH_3$ groups, the in situ XRF data showed that TiO_2 could no longer be deposited in the He/H_2 plasma treated film after 8 ALD cycles.

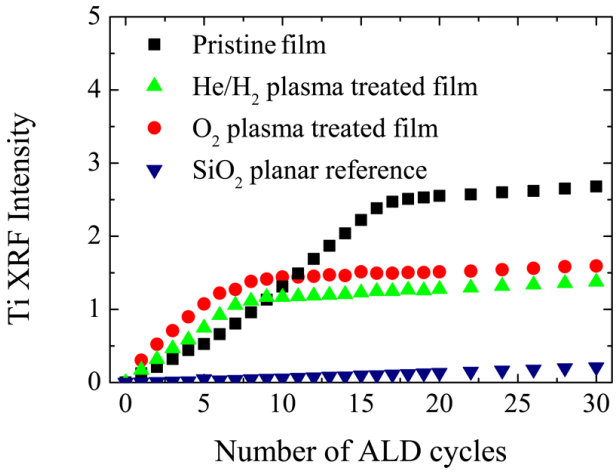

Figure 3.8: In situ XRF measurements during ALD of TiO_2 on a planar SiO_2 reference substrate and on the three surface modified nanoporous low-k films. The Ti Kα (4.5 keV) peak area is proportional to the number of Ti atoms deposited.

3.4.5 Tuning the Pore Size of Ink-Bottle Mesopores by Atomic Layer Deposition [13]

The ALD processes of TiO_2 and HfO_2 in ink-bottle shaped mesopores is studied by a combination of in situ XRF, EP and advanced electron tomography. This demonstrate that ALD is an excellent technique for tuning the pore size of ink-bottle shaped mesopores at the atomic level. Furthermore, our study proves that in situ XRF is an ideal approach to control the ALD process cycle-per-cycle. The methodology presented here is very attractive for the synthesis of novel molecular separation systems and catalyst supports.

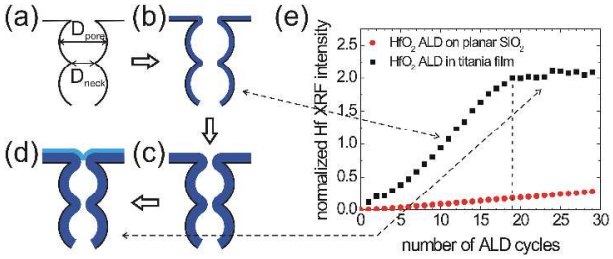

Figure 3.9: (a-d) Schematic representation of conformal ALD in ink-bottle mesopores. (e) In situ XRF during HfO_2 ALD on a planar SiO_2 substrate and on a mesoporous titania film: Hf Lα (7.9 keV) peak area against the number of ALD cycles.

3.4.5.1 Atomic layer deposition-based tuning of the pore size in mesoporous thin films studied by in situ grazing incidence small angle X-ray scattering [14]

Atomic layer deposition (ALD) enables the conformal coating of porous materials. It is, however, not straightforward to obtain information about the conformality of ALD coatings deposited in pores with diameters in the low mesoporous regime ($<$10 nm). *In situ* synchrotron based grazing incidence small angle X-ray scattering is used to gain information on the change in density and internal surface area during ALD of TiO_2 in a porous titania film with small mesopores (3-8 nm). The results are shown to be in good agreement with in situ X-ray fluorescence data representing the evolution of the amount of Ti atoms deposited in the porous film. Analysis of both datasets indicates that the minimum pore diameter that can be achieved by ALD is determined by the size of the Ti-precursor molecule.

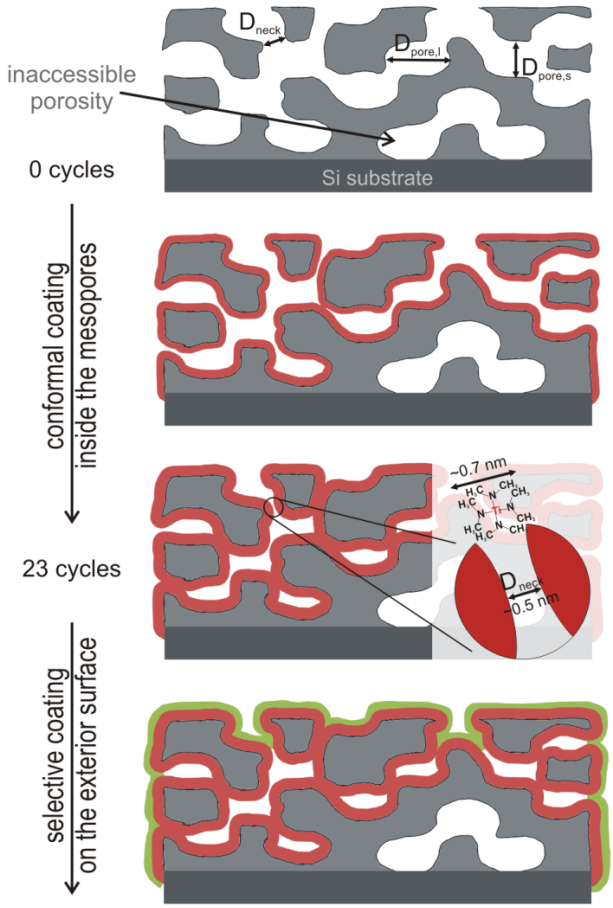

Figure 3.10: Schematic representation of the mesoporous titania film and the pore filling by ALD of TiO_2.

3.4.5.2 In situ XAS and XRF study of nanoparticle nucleation during O_3-based Pt deposition [15]

X-ray absorption spectroscopy (XAS) and X-ray fluorescence (XRF) were combined in situ to study the ALD-based synthesis of Pt catalysts. This first time combination of synchrotron-based techniques was applied during the (methylcyclopentadienyl)trimethylplatinum/ozone deposition process executed at 150°C on a silica support. XAS and XRF were recorded simultaneously at different catalyst loadings in this nucleation regime. Analysis of the combined in situ data yielded a quantitative picture of the evolution of the diameter, shape, lattice packing and density of the deposited Pt clusters. Additionally, the degree of oxidation at the

cluster surface after the ozone pulse could be monitored. At the early start of the deposition process, Pt adatoms cluster together to form stable nuclei. By crosslinking the XRF and XAS data, a linear increase in cluster diameter with Pt loading is observed. The surface of the Pt clusters is shown to be oxidized immediately after the ozone exposure. The combined application of in situ XRF and XAS thus allowed for an advanced identification of the ALD-deposited Pt nanoparticles.

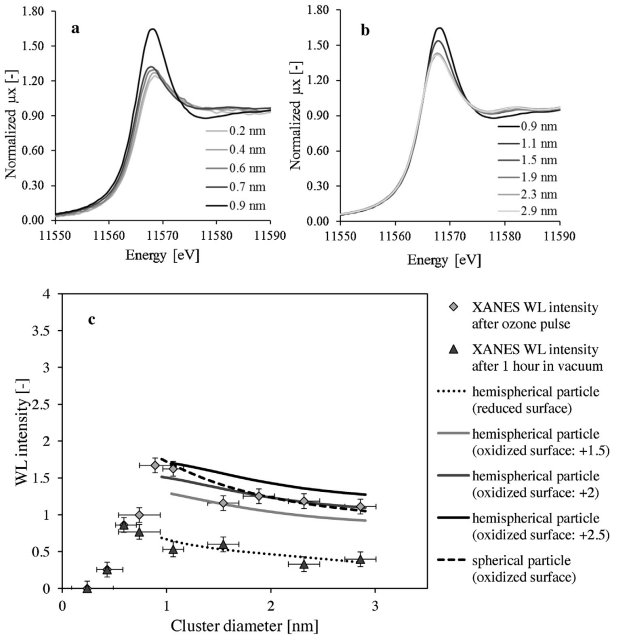

Figure 3.11: (a) Normalized XANES spectra immediately after the O_3 pulse during the deposition process for sizes ranging from 0.2 nm to 0.9 nm and (b) 0.9 nm to 2.9 nm. (c) White line intensity as a function of particle diameter during deposition. Two datasets are shown: one immediately after the ozone pulse and one after 1h in vacuum. These trends are modeled by different cluster models. The resulting fits to the data series are plotted too. Finally, two additional curves are shown which possess different cluster surface oxidation states for the hemispherical cluster model. These are represented in order to give the reader a feeling on the sensitivity of the applied XANES methodology to the degree of cluster surface oxidation.

References

[1] H. Fujiwara. *Spectroscopic Ellipsometry: Principles and Applications*. 2008.

[2] E. Langereis, S. B. S. Heil, H. C. M. Knoops, W. Keuning, M. C. M. van de Sanden, and W. M. M. Kessels. *In Situ Spectroscopic Ellipsometry as a Versatile Tool for Studying Atomic Layer Deposition*. Journal of Physics D: Applied Physics, 42(7):073001, apr 2009.

[3] Y. J. Chabal. *Surface Infrared Spectroscopy*. Surface Science Reports, 8(January):211–357, 1988.

[4] M. Dai. *In Situ Infrared Spectroscopy Study of Atomic Layer Deposition of High-K M Metal Oxide and Metal on Passivated Silicon Surfaces*. PhD thesis, 2008.

[5] J. Kwon, M. Dai, M. D. Halls, E. Langereis, Y. J. Chabal, and R. G. Gordon. *In Situ Infrared Characterization During Atomic Layer Deposition of Lanthanum Oxide*. The Journal of Physical Chemistry C, 113(2):654–660, jan 2009.

[6] V. R. Rai and S. Agarwal. *In Situ Diagnostics for Studying Gas-Surface Reactions During Thermal and Plasma-Assisted Atomic Layer Deposition*. Journal of Vacuum Science & Technology A: Vacuum, Surfaces, and Films, 30(1):01A158, 2012.

[7] B. A. Sperling, W. A. Kimes, and J. E. Maslar. *Reflection Absorption Infrared Spectroscopy During Atomic Layer Deposition of HfO2 Films From Tetrakis(ethylmethylamido)hafnium and Water*. Applied Surface Science, 256(16):5035–5041, jun 2010.

[8] A. Dillon, A. Ott, J. Way, and S. George. *Surface Chemistry of Al2O3 Deposition Using Al(CH3)3 and H2O in a Binary Reaction Sequence*. Surface Science, 322(1-3):230–242, 1995.

[9] L. G. Gosset, J.-F. Damlencourt, O. Renault, D. Rouchon, P. Holliger, A. Ermolieff, I. Trimaille, J.-J. Ganem, F. Martin, and M.-N. Séméria. *Interface and Material Characterization of Thin Al2O3 Layers Deposited by ALD Using TMA / H2O*. Journal of Non-Crystalline Solids, 303:17–23, 2002.

[10] A. Hasegawa. *Free Electron Laser*. Bell System Technical Journal, 57(8):3069–3089, oct 1978.

[11] J. Als-nielsen and D. McMorrow. *Elements of Modern X-Ray Physics*. John Wiley & Sons, Ltd, second edition, 2011.

[12] E. Levrau, K. Devloo-Casier, J. Dendooven, K. F. Ludwig, P. Verdonck, J. Meersschaut, M. R. Baklanov, and C. Detavernier. *Atomic Layer Deposition of TiO 2 on Surface Modified Nanoporous Low- K Films*. Langmuir, 29(39):12284–12289, oct 2013.

[13] J. Dendooven, B. Goris, K. Devloo-Casier, E. Levrau, E. Biermans, M. R. Baklanov, K. F. Ludwig, P. V. D. Voort, S. Bals, and C. Detavernier. *Tuning the Pore Size of Ink-Bottle Mesopores by Atomic Layer Deposition*. Chem. Mater., 24(11):1992–1994, jun 2012.

[14] J. Dendooven, K. Devloo-Casier, M. Ide, K. Grandfield, M. Kurttepeli, K. F. Ludwig, S. Bals, P. Van Der Voort, and C. Detavernier. *Atomic Layer Deposition-Based Tuning of the Pore Size in Mesoporous Thin Films Studied by in Situ Grazing Incidence Small Angle X-Ray Scattering*. Nanoscale, 6(24):14991–14998, oct 2014.

[15] M. Filez, H. Poelman, R. R. K. Ramachandran, J. Dendooven, K. Devloo-Casier, E. Fonda, C. Detavernier, and G. B. Marin. *In Situ XAS and XRF Study of Nanoparticle Nucleation During O 3-Based Pt Deposition*. Catal. Today, 229:2–13, jun 2014.

4

Paper I: In situ synchrotron based x-ray techniques as monitoring tools for atomic layer deposition.*

4.1 Abstract

Atomic layer deposition (ALD) is a thin film deposition technique that has been studied with a variety of in situ techniques. By exploiting the high photon flux and energy tunability of synchrotron based x-rays a variety of new in situ techniques become available. X-ray reflectivity, Grazing Incidence Small Angle X-ray Scattering, X-ray diffraction, X-ray fluorescence, X-ray absorption spectroscopy and X-ray photoelectron spectroscopy are reviewed as possible in situ techniques during ALD. All these techniques are especially sensitive to changes on the (sub-) nanometer scale, allowing a unique insight into different aspects of the ALD growth mechanisms.

* Published as: Devloo-Casier, K., Ludwig, K. F., Detavernier, C., & Dendooven, J.In situ synchrotron based x-ray techniques as monitoring tools for atomic layer deposition. Journal of Vacuum Science & Technology A: Vacuum, Surfaces, and Films, 32(1), 010801. (2014)
http://doi.org/10.1116/1.4851716

4.2 Introduction

Atomic layer deposition (ALD) is a thin film deposition technique which enables thickness control at the atomic level and conformal deposition on high aspect ratio structures. [1–4] The unique properties of ALD are achieved by using self-terminating reactions between precursor molecules and the surface. Typically two different precursor vapors or gases are used. They are sequentially introduced to the reaction chamber. Between the exposures, the chamber is either purged with an inert gas or evacuated. This prevents unwanted gas phase reactions and removes reaction products from the chamber. The precursor chemistry is optimized to ensure saturation of the surface with precursor molecules after every half cycle. Because an ALD process consists of very well defined steps, it is a process that allows for a detailed study of the involved mechanisms during growth.

A wide range of characterization techniques have been implemented on ALD reactors, enabling in situ monitoring of growth. They can be grouped into different categories, based on the properties that are measured. A first category directly monitors physical changes. Examples are quartz crystal microbalance (QCM) [5–8] measuring mass change, 4-point probe [9] measuring electronic resistivity and thermopile [10] measuring the reaction enthalpies. A second category of techniques probes the gas species that are being consumed and formed during the various chemical reactions involved in the ALD process. Examples are quadrupole mass spectrometry (QMS) [7, 8, 11], optical emision spectroscopy (OES) [12, 13] and fourier transformed infrared absorption spectroscopy (FTIR) [14]. A last category uses light from either the infrared or visual range, to monitor the optical properties of the surface and/or the deposited layer. Examples are surface photoabsorption (SPA) [15, 16], fourier transformed infrared absorption (FTIR) [17–19], spectroscopic ellipsometry (SE) [20] and ellipsometric porosimetry (EP) [21]. These optical techniques are the easiest to use in practice, since no measuring equipment needs to be incorporated within the ALD chamber. They can remotely probe the sample surface and only require an entry and exit window to pass light into and out of the reactor chamber.

The relatively easy incorporation of light based techniques into ALD research has encouraged the exploration of the possibilities for wavelengths from the IR to the UV. The aim of this paper is to show that this wavelength range can be expanded to x-rays, opening up an even wider variety of characterization possibilities. Although standard x-ray based analysis techniques like x-ray reflectivity and diffraction using lab-based x-ray sources have proven valuable for ex situ characterization of ALD deposited thin films, most in situ experiments during ALD require synchrotron-based x-rays. To enable in situ studies during ALD, it is important to limit the impact of the prolonged purge or evacuation times that are introduced between subsequent ALD (half-)cycles to perform the measurements.

The high photon flux at a synchrotron facility is beneficial in this respect, because it allows for shorter acquisition times compared to lab-based x-ray sources. The high intensity x-ray flux also lowers the detection limit, enabling the study of layer growth from the very first ALD cycle onward. A second main advantage of synchrotron sources is its unique ability to tune the photon energy to a specific experiment and material system. Additionally, as shown in table 4.1, the use of synchrotron based x-rays broadens the available tool box of in situ methods to a number of techniques which are synchrotron specific, like x-ray absorption spectroscopy (XAS) and grazing incidence small angle x-ray scattering (GISAXS). The table also includes the most important references reporting the in situ use of the respective technique during ALD.

Technique	Accessible information	References
XRR	Thickness Roughness Electron density	22–27
GISAXS	Morphology Roughness	28 29
XRD	Phase and size of crystalline grains	30, 31
XRF	Composition	26, 29, 32–35
EXAFS(in vacuo)	Local atomic environment	36–41
XPS(in vacuo)	Chemical state	37, 38, 42–45

Table 4.1: Available in situ characterization methods when using synchrotron radiation and the primary sample properties, important to ALD research, that become accessible.

This manuscript is intended as a tutorial review of in situ x-ray techniques as monitoring tool for ALD. In the following sections, the techniques mentioned in table 4.1 will be briefly introduced and their possibilities will be illustrated with examples. Note that we do not intend to review the methods in detail, but rather want to demonstrate the specific advantages of these techniques as in situ analysis tool for ALD growth. Also certain practical constraints and difficulties will be addressed.

4.3 Experimental

The in situ experiments presented in this paper have been performed in the UHV thin film growth facility installed at beamline X21 of the National Synchrotron Light Source at Brookhaven National Laboratory. [46] This setup consists of a stainless steel reaction chamber pumped by a turbo molecular pump to a base pressure of 10^{-6} mbar (figure 4.1). Samples can be introduced via a loadlock and mounted vertically in front of a resistive heating plate. The chamber is equipped with an entrance beryllium window for the transmission of the x-rays provided by the synchrotron, and two exit beryllium windows for the transmission and detection of the reflected, scattered and fluorescent x-rays from the sample. A Vortex silicon drift detector mounted perpendicular to the sample surface is available to collect the fluorescence, while 2D scattering intensity maps can be recorded using a Dectris, Pilatus 100k, 2D area detector mounted parallel to the sample. The whole chamber is mounted on a rotatable table, to allow tuning of the incidence angle to fit the experiment.

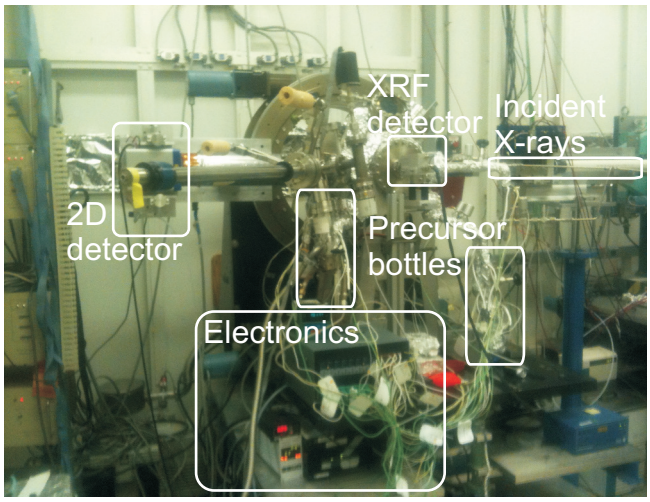

Figure 4.1: UHV film growth facility, adapted for thermal ALD, installed at beamline X21 of the National Synchrotron Light Source at Brookhaven National Laboratory.

Enabling thermal ALD of oxides in this setup required, amongst other things, the connection of precursor supply lines. H_2O vapor was used as oxygen source, while table 4.2 lists the precursors that were used as metal source for the respective oxides. The delivery lines were equipped with needle valves to control the flow and pneumatic valves to regulate the gas inlet. For all processes, the exposure and pumping times were chosen long enough to ensure saturation and prevent CVD reactions, respectively. During the exposures, the pressure in the chamber was

usually ca. $5\,10^{-3}$ mbar. In the case of TEMAH and TDMAT, Ar was used as a carrier gas to compensate for the low vapor pressure of these materials. Finally, to avoid condensation of the precursors, the delivery lines and chamber walls were heated to 60°C and 80°C, respectively.

Oxide	Metal source
Al_2O_3	Trimethylaluminium (TMA)
ZnO	Diethylzinc (DEZ)
HfO_2	Tetrakisethylmethylaminohafnium (TEMAH)
TiO_2	Tetrakisdimethylaminotitanium (TDMAT)

Table 4.2: Deposited oxides with the used metal source. For TEMAH and TDMAT, argon is used as a carrier gas

Besides for the study of metal oxide ALD processes, synchrotron-based x-ray techniques are extremely useful to investigate ALD of metals. To demonstrate this, and because of the incompatibility of the setup at beamline X21 with metal ALD, ex situ proof-of-principle experiments were performed on home-deposited Pt samples. These samples were prepared using the earlier reported (methylcyclopentadienyl)trimethylplatinum ($MeCpPtMe_3$) / ozone process. [47]

4.4 Scattering Based Techniques

4.4.1 X-ray Reflectivity

X-ray reflectivity (XRR) is widely used in the determination of thickness, roughness and density of thin films. [48] XRR measures the intensity of an x-ray beam that is specularly reflected from a surface as a function of the incident angle (typically from 0 to 3°). The complex refractive index (n) for x-rays is slightly smaller than 1.

$$n = 1 - \delta + i\beta \tag{4.1}$$

Hence, total external reflection occurs at low angles and when passing from a less dense to a more dense material. This is opposite to the visible light behavior. This allows the determination of the critical angle of the studied material. The critical angle (α_c) is directly linked to the electron density (n_e) of the reflecting medium.

$$\alpha_c = \sqrt{2\delta} \approx \sqrt{2\frac{r_0\lambda^2}{2\pi}n_e} \tag{4.2}$$

where r_0 is the Bohr atomic radius and λ the x-ray wavelength. Above the critical angle, the incident x-rays penetrate the film and the intensity of the reflected beam rapidly decreases with the angle. The use of synchrotron radiation increases the

intensity of the incident and corresponding reflected beam. Therefore, compared to a lab based system, the maximum angle accessible will be increased with a couple degrees. The x-rays that penetrate the thin film will be reflected at the thin film/substrate interface. Together with the x-rays reflected at the air/film interface, this will create an interference pattern. These periodic oscillations in the XRR pattern, also known as Kiessig fringes, allow the determination of the film thickness (order 1 nm to 100 nm). If the surface is rough, the intensity of the reflected x-rays will drop off faster for increasing angles. The interface roughness will reduce the amplitude of the fringes. The difference in density between the film and the support will also influence the amplitude of the fringes. [49] Film thickness, roughness and density are normally determined by fitting the measured curve to a theoretical model, like Parratt's formalism. [50] Since thin films grown by ALD are in most cases only a few nm thick and relatively smooth, XRR is ideally suited to study properties of growing ALD films. Because of the obvious link to thin film research, XRR was the first synchrotron based technique that has been utilized in ALD research to study high dielectric constant alumina thin films. [22] Since then several groups have adopted the technique into ALD research. [23–27]

In order to be useful as an in situ technique, XRR needs to be sensitive to changes in thickness and roughness on the order of Ångstroms and changes to the density of a few percent. Figure 4.2 aims to demonstrates the sensitivity of XRR. The simulations show that changes in the thickness of the Al_2O_3 film of the order of 1 Å can easily be distinguish by their change in oscillation period. The influence of a small roughness variation and a small change in layer density are shown to have a noticeable effect on the XRR pattern. From the simulations it is also clear that a lab source, with a typical range up to 3°, is not sufficient to study layers with a thickness of 25 Å(or less). The higher intensity and corresponding larger angular range of synchrotron radiation is therefore needed for in situ studies of the very first stages of growth during ALD. [26]

To illustrate the possibilities of XRR as an in situ technique during ALD, we will discuss results obtained during the growth of Al_2O_3 on native SiO_2, followed by the growth of TiO_2 on top of the alumina. In figure 4.3 the measured XRR pattern is shown for the bare substrate, after 30 and 80 ALD cycles of Al_2O_3 and subsequently 40 ALD cycles of TiO_2. From the decrease of the period of the fringes, it is clear that the layer is getting thicker with increasing ALD cycles. In table 4.3 the thickness, roughness and density are given for each step, based on a fit to a theoretical model. It is important to note that the measurement after 30 ALD cycles of Al_2O_3 would not give the desired information if a lab based source would be used instead of the used synchrotron radiation as the angular range available at a lab based setup is limited to about 3°.

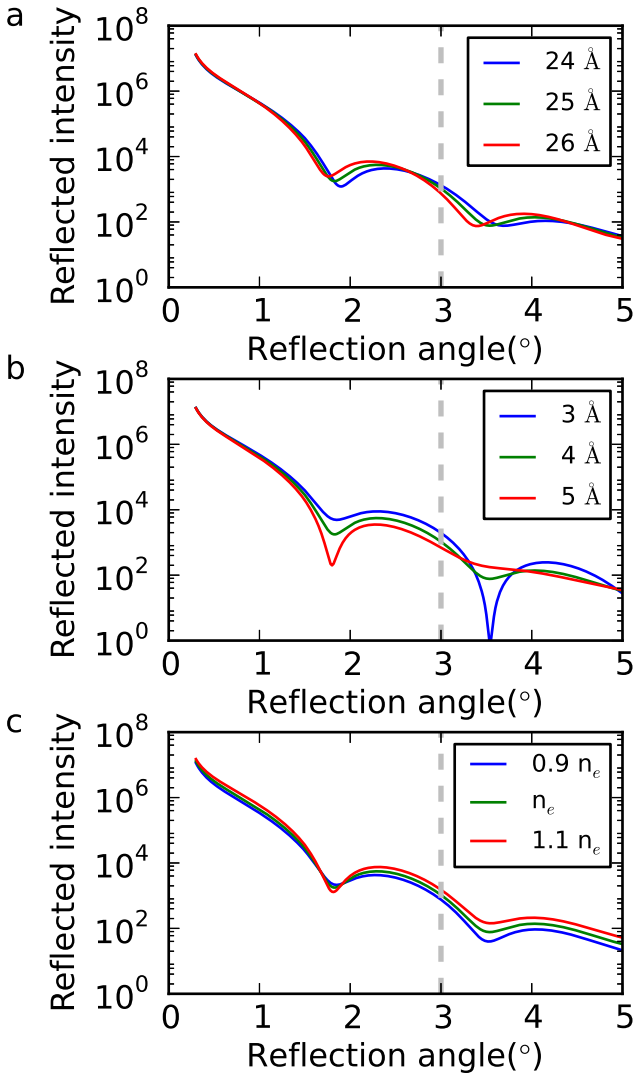

Figure 4.2: Simulated XRR patterns for Al_2O_3 on silicon. The parameters of the Al_2O_3 are changed to show the sensitivity to changes of interest during an ALD experiment. The angular range available to a lab based setup is marked with the dashed line indicating the need for synchrotron radiation at low layer thicknesses. Figure 4.2a shows the sensitivity of XRR to thickness variations, figure 4.2b shows the sensitivity of XRR to roughness variations and figure 4.2c shows the sensitivity of XRR to density variations in respect to the bulk density of Al_2O_3 (n_e).

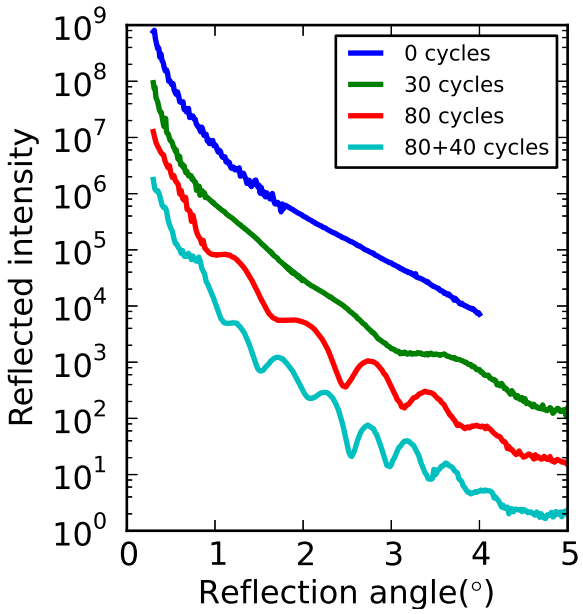

Figure 4.3: XRR pattern measured after respectively 30 and 80 ALD cycles of Al_2O_3 and subsequently 40 ALD cycles of TiO_2. The measurements are shifted vertically with respect to each other for clarity.

ALD cycles	30 cycles	80 cycles	80 + 40 cycles
Interface Roughness(Å)	2.5	1.4	1.4
Al_2O_3 Thickness(Å)	15.5	55.3	55.3
Al_2O_3 Roughness(Å)	2.4	2.5	2.5
Al_2O_3 Density(g/cm^3)	2.68	3.67	3.67
TiO_2 Thickness(Å)			33.0
TiO_2 Roughness(Å)			3.1
TiO_2 Density(g/cm^3)			4.39

Table 4.3: Values for thickness, roughness and density obtained by fitting the XRR patterns shown in figure 4.3.

From the obtained values, one can see a clear increase in thickness, as can be expected from the standard Al_2O_3 process. The growth per cycle (GPC) can be calculated to be about 0.8 Å per cycle between ALD cycle 30 and 80. During the first 30 ALD cycles, however, the growth rate is lower and the film density is low compared to bulk values for Al_2O_3. This points to nucleation effects related to the starting surface. During the following cycles, the film densifies to the expected

value. Both the interface and surface roughness are low and do not change a lot during deposition. The data here is only shown as an example, but an experiment with a higher frequency in measurements could provide a lot of extra insight in the evolution of thickness, roughness and density.

When determining the properties of the TiO_2 layer, an added advantage of in situ XRR to ex situ XRR becomes apparent. An XRR pattern for a multilayer of materials is in most cases rather complex, since it contains contributions from every layer. The analysis can therefore be very difficult. Here the values obtained for the Al_2O_3 can be used as input parameters for the model of the multilayer. For even more complex multilayers, when an in situ XRR measurement is performed after the completion of every layer, the parameters for that layer can be determined and used as input parameters for the analysis of the more complex structure with an additional layer. This makes the analysis of the final structure a lot more straightforward and increases the accuracy, since only a limited set of parameters needs to be fitted at a time.

4.4.2 Grazing Incidence Small Angle X-ray Scattering

Grazing incidence small angle x-ray scattering (GISAXS) is a powerful technique for the morphological characterization of nanoscale objects (particles, pores, ...) at surfaces, at buried interfaces, or in thin films. Although the technique was originally introduced in 1989, [51] it was only in the past decade with the increasing interest in nanostructured surfaces and films that GISAXS has gained popularity as a structural characterization technique, as illustrated in a recent review paper. [52] GISAXS yields nanometer scale information averaged over a macroscopic sample area, and allows to asses buried structures in a non-destructive way. Because no special sample preparation is required, GISAXS is also suitable for in situ experiments. High-brilliance synchrotron radiation is, however, almost a prerequisite. One of the main drawbacks of the technique is that the morphological information is obtained in reciprocal space. In order to be able to make an interpretation of the GISAXS images in real-space, a model, taken into account the distorted wave born approximation (DWBA), which includes 4 different scattering effects, has to be used. [52]

A GISAXS experiment essentially consists of measuring the diffuse scattering around the specularly reflected beam at a fixed angle of incidence (figure 4.4). In order to reduce the unwanted bulk scattering from the substrate and to enhance the near-surface scattering, the incident angle, α_i, is kept very small with respect to the sample surface. In this geometry, any kind of roughness or electron density contrast in the (sub)surface region of the sample leads to scattering in off-specular directions. The scattered intensity is usually recorded by a 2D detector (located at 1-4 m from the sample) as a function of the out-of-plane angle α_f and the in-plane

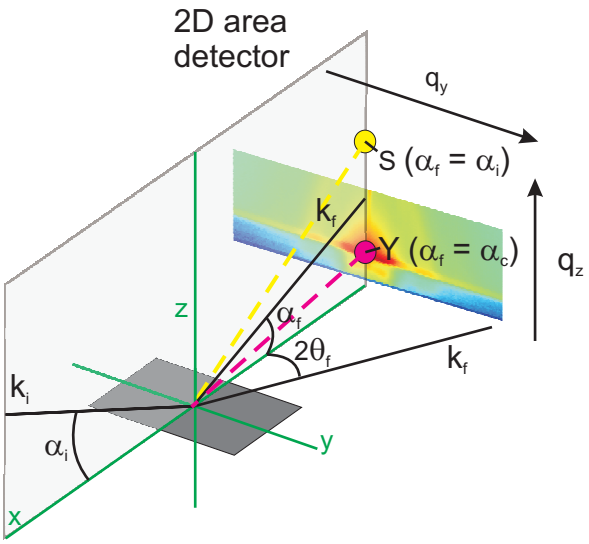

Figure 4.4: Schematics of the GISAXS geometry. Incident x-rays have a wavevector $\mathbf{k}_i$. Due to scattering the wavevector changes to $\mathbf{k}_f$. The momentum transfer due to scattering is denoted as $\mathbf{q}$. The position of the Yoneda peak has been marked with Y and the position of the reflected beam has been marked with S.

angle $2\theta_f$. To prevent saturation, or even damage, of the detector, the direct and specularly reflected beam, which have an intensity of several orders of magnitude higher than the diffuse scattering, are masked by slits or beamstops. Because the scattered x-rays are low in intensity, scattering from the direct beam at the entrance window to the chamber needs to be blocked with a carefully-positioned knife edge between the entrance window and the sample. Similarly, the specularly reflected beam is preferably blocked prior to hitting the exit window.

In order to deduce morphological information from the measured 2D scattering patterns, the scattering vector **q** is defined as $\mathbf{k}_f$ - $\mathbf{k}_i$, with $\mathbf{k}_i$ and $\mathbf{k}_f$ the wavevectors of the incident and scattered beams, respectively. The scattering vector components q_x, q_y and q_z are related to the angles α_i, α_f and $2\theta_f$ by:

$$\begin{aligned} q_x &= k_0 \left[\cos\left(2\theta_f\right)\cos\left(\alpha_f\right) - \cos\left(\alpha_i\right)\right] \\ q_y &= k_0 \left[\sin\left(2\theta_f\right)\cos\left(\alpha_f\right)\right] \\ q_z &= k_0 \left[\sin\left(\alpha_f\right) + \sin\left(\alpha_i\right)\right] \\ k_0 &= |\mathbf{k}_i| = |\mathbf{k}_f| = 2\pi/\lambda \end{aligned} \tag{4.3}$$

Because the angles are limited to a few degrees, the scattering vector components are also small, i.e. between 0 and a few nm^{-1}, meaning that dimensions from a few up to hundreds of nanometers are probed in real space. [53] Variation in the scattering intensity with q_y provides in-plane (lateral) structural information,

while intensity variation with q_z provides out-of-plane (normal) structural information. Full analysis of the 2D GISAXS spectra can provide information on the geometry, size distribution and spatial correlation of the scattering features.

If the exit angle equals the critical angle, an enhancement of the scattered intensity arises. [54] The so-called Yoneda peak is a typical dynamic feature of diffuse scattering. Because the critical angle is related to the electron density of the scattering medium, the Yoneda peak is a material dependent feature.

GISAXS can be useful in ALD research to study a range of very different problems. Firstly, GISAXS can be used to study thin film growth on planar surfaces. In this case the scattering can provide information on the evolution of surface roughness during growth. This has already been shown in a study of the initial growth of HfO_2 on Si and Ge substrates. [29] Secondly, in the case of for example metal ALD, where islands of material are being formed during the initial stages of growth, GISAXS allows for the analysis of the size, shape and interparticle spacing. This can be very important in e.g. the determination of particle size and dispersion for catalyst preparation by ALD. Thirdly, GISAXS is frequently used to study nanostructured features at surfaces, such as nanoporous layers or quantum dots. [55, 56] These structures will have a very distinctive GISAXS pattern. When ALD is used in combination with these materials, the changes in scattering can be used to study e.g. conformality and pore filling.

To show the power of GISAXS in ALD research, three examples will be discussed. All experiments used a similar geometry, working at an incident angle α_i of 0.8° in the first two examples and at an incident angle α_i of 1° for the third example. A PILATUS 100K, 2D detector was used to measure the scattered x-rays, positioned approximately 1 m away from the sample. All measurements were performed at an x-ray energy of 10 keV.

In a first example, in situ GISAXS is used to study the evolution of the surface roughness during growth of a HfO_2 layer on a ALD grown Al_2O_3 surface. The evolution of the scattered intensity for low q_z (α_f=0.2°, q_z=0.88 nm^{-1}) during ALD is displayed in figure 4.5.

In the low q_z limit, the weighted integral of the GISAXS intensity can be used as a measure for the square of the rms roughness. [57]

$$\sigma^2_{\mathrm{rms}} \propto \int q_y I(q_y) dq_y \tag{4.4}$$

This enables a qualitative view on the roughness evolution during ALD deposition. In figure 4.6 the square root of the integral from equation 4.4 is shown as a function of ALD cycles. A clear evolution in roughness can be seen. During the first ALD cycles the surface roughness increases and stabilizes after several ALD cycles.

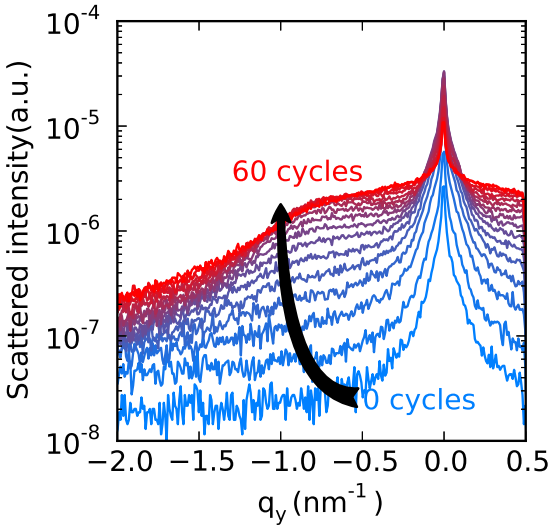

Figure 4.5: Evolution of the scattering intensity for low q_z (α_f=0.2°, q_z=0.88 nm^{-1}), as measured every 4 ALD cycles during ALD of HfO_2 on an Al_2O_3 surface.

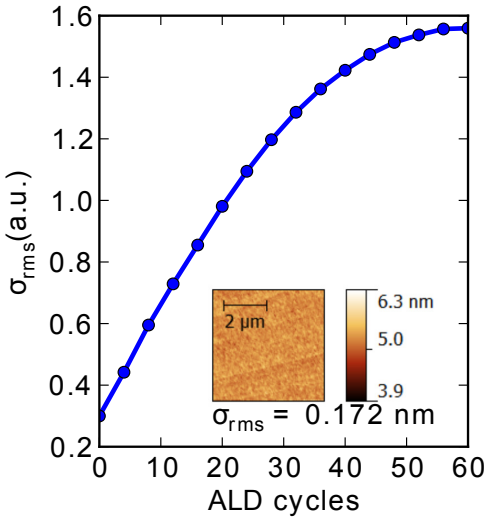

Figure 4.6: Qualitative evolution of roughness during HfO_2 growth based on the scattered intensity, calculated using equation 4.4. The AFM image at the end of the growth is included as an inset, with the corresponding σ_{rms} as determined from the AFM image.

The second example concerns a proof of principle. Until now, no in situ GISAXS measurements have been reported during metal ALD. Here we will discuss the GISAXS pattern obtained for various stages of Pt growth on native SiO_2. These measurement were not performed during ALD growth itself, but were measured on a set of preprepared samples. The Pt has been grown using a thermal ALD process at 150°C. [47] Similar experiment have already been reported for the growth of Pt on $SrTiO_3$. [58]

Platinum is known to form islands during the very first stages of growth, due to slow nucleation on non-metallic surfaces. These islands or clusters will be distributed over the surface at random intervals and have a certain size distribution. As GISAXS looks at a macroscopic sized area of the substrate, the scattering contributions of many individual islands will get averaged out to show a mean distance and/or size of the island. In figure 4.7 the scattering pattern is shown for 30, 60 and 100 ALD cycles. A qualitative analysis of the patterns can already offer some insight. The GISAXS pattern for 30 ALD cycles only shows the Yoneda peak around the critical angle of silicon (α_c = 0.18°, q_z = 0.86 nm^{-1}), indicating that the silicon substrate is responsible for most scattering and hence that not a lot of growth has occurred. After 60 ALD cycles, two lobes appear, which hint in the direction of particle formation on the surface. Finally after 100 ALD cycles the lobes have shifted to smaller q_y values, indicating that larger particles have been formed. The position of the Yoneda wing has also shifted to higher q_z (in other words also higher α_f), corresponding to the higher critical angle for a platinum layer (α_c = 0.46°, q_z = 1.12 nm^{-1}). The position of the lobes can be used to determine the average interparticle spacing and shape of the particles. To obtain these values, patterns can be modeled using specific software (e.g. isGISAXS [59]), but this is out of the scope of this article.

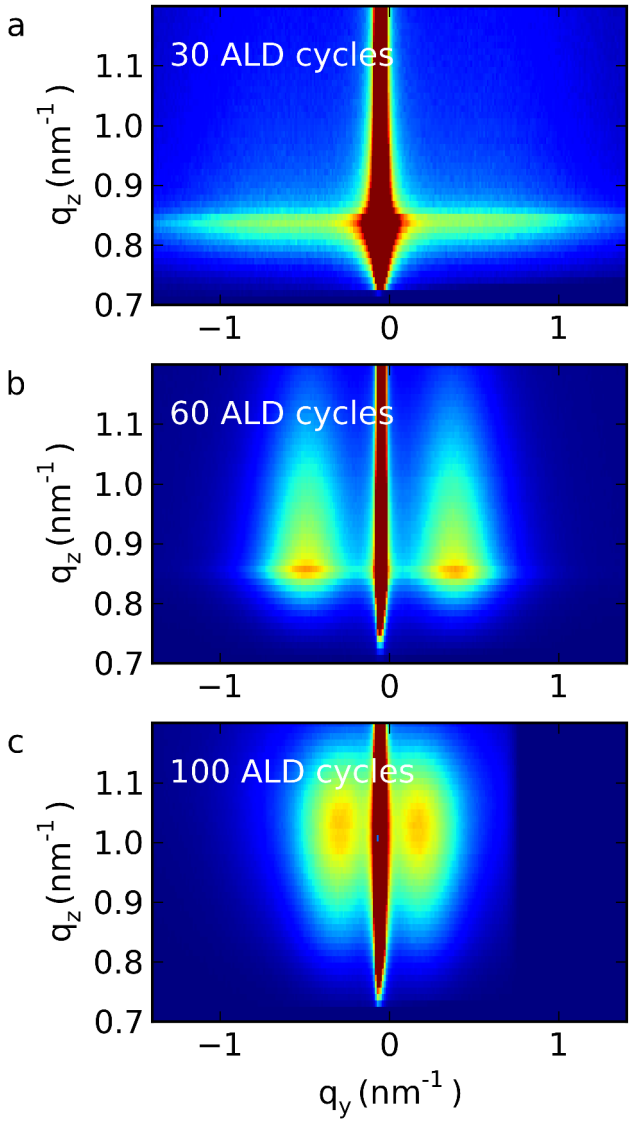

Figure 4.7: GISAXS patterns measured after respectively 30 ALD cycles (a), 60 ALD cycles (b) and 100 ALD cycles (c) of ozone based Pt deposition on Si. The appearance of lobes in the scattering pattern indicates the formation of islands. A shift of the critical angle can also be seen. The samples were prepared in the lab and studied ex situ in the setup at beamline X21 at Brookhaven National Laboratory.

A third example illustrates the use of GISAXS to study conformal ALD in complex nanostructures. Here, GISAXS was used to analyze the growth of ZnO in a porous silica film on a silicon support. The porous silica film has mesopores of the order of several nm. As has already been shown in literature [21, 34, 60], these structures can be either conformally coated with ALD or the pores can be sealed. To ensure a large enough penetration depth for the x-rays, and incident angle of 1° was chosen for these experiments, instead of the previously used incident angle of 0.8°. When we look at the GISAXS pattern of the uncoated porous silica film (see figure 4.8) we see a very distinctive pattern. The Yoneda peak is clearly visible, as is a semicircle. This semicircle can be attributed to the ordered pores in the substrate. This is due to an interference effect of x-rays scattering at the pores' internal surface, due to the difference in refractive index. As the film gets gradually filled with ZnO, the Yoneda peak shifts to higher q_z values. This indicates a densification of the film as more and more ZnO gets incorporated into the porous structure. A change in the intensity corresponding to the scattering of the internal surface can be observed. As the contrast in refractive index changes due to the higher electron density of ZnO, the scattering pattern is influenced. After the ZnO deposition, the Yoneda peak has shifted to a value corresponding with the higher electron density of ZnO and the semicircle is still present indicating the change from open pores to filled pores.

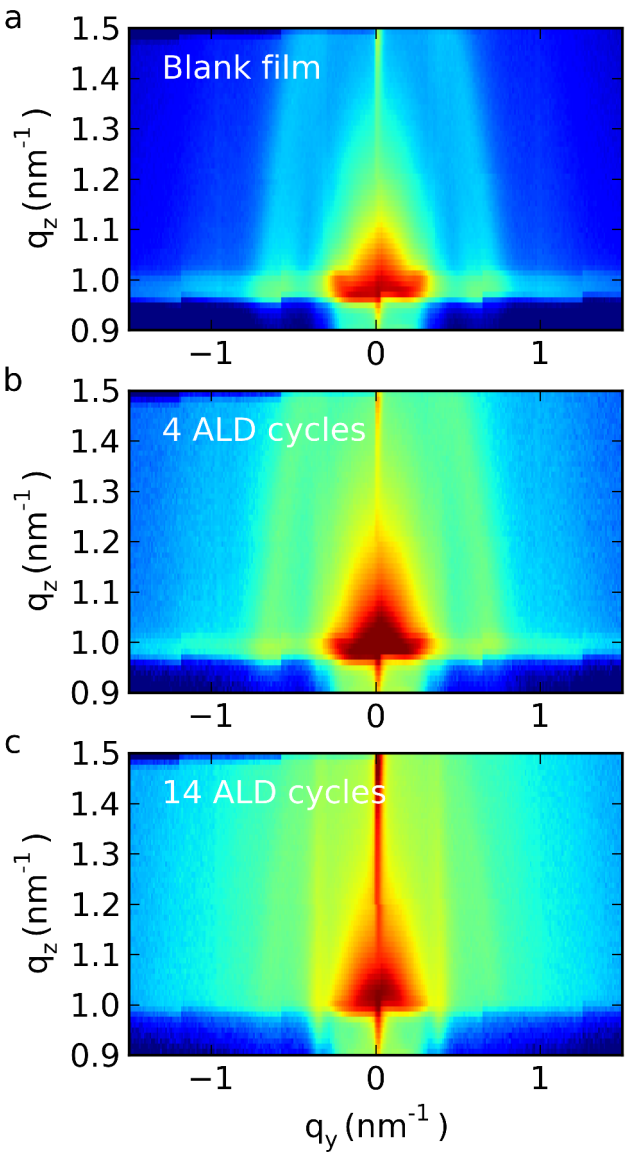

Figure 4.8: In situ GISAXS pattern for a porous silica film before deposition (a), after 4 ALD cycles (b) and after 14 ALD cycles (c) of DeZ and H_2O respectively. A scattering pattern corresponding to the porous film can be seen. The shift of the critical angle shows the densification of the film by filling the porous structure.

4.5 X-ray Diffraction

X-ray diffraction (XRD) is one of the most widely used techniques in solid state sciences and materials research. The use of XRD enables the study of crystalline materials. As most materials deposited with ALD are amorphous during deposition, in situ XRD is limited to certain ALD processes. The most well-known oxide deposited with ALD that is crystalline during deposition is ZnO. [61] Most metals can also readily be studied with XRD. XRD has only been used a few times as an in situ technique. [24, 31] There are however numerous examples of synchrotron based ex situ XRD studies on ALD grown layers. [30, 62–66] This indicates that synchrotron based XRD has several advantages to lab based XRD. The main advantage is the lower detection limit. As the signal to noise ratio can be greatly increased when using the high photon flux at a synchrotron, even very small amounts of crystalline material can be detected. The lower divergence of the x-ray beam is also a prerequisite when performing grazing incidence XRD. GIXRD is especially beneficial when studying thin films. In situ XRD can be used to identify crystalline phases, grain orientation and grain size of crystalline materials. If the crystallites are randomly orientated in the film, the intensity of the diffraction peaks can be used as a measure of the amount of deposited material. Detailed analysis of the peakwidths in the XRD pattern with the Scherrer equation can yield grain sizes within the deposited film.

$$\tau = \frac{K\lambda}{\beta \cos\theta} \tag{4.5}$$

Here, τ is the mean size of the ordered crystalline domains, K is a dimensionless shape factor, with a value close to unity depending on the shape of the crystallites, λ is the x-ray wavelength, β is the line broadening at half the maximum intensity (FWHM) in radians and θ is the Bragg angle.

The use of XRD as an in situ technique during ALD allows for a detailed study of for example the nucleation of metals, the evolution of grain sizes during growth, the influence of growth conditions on the crystallinity and the influence of the support(epitaxial growth).

To illustrate the technique, we will again discuss a proof of principle experiment. The ex situ XRD patterns for Pt grown on native SiO_2 for 60, 100 and 200 ALD cycles are shown in figure 4.9. The XRD measurements were performed with a Bruker D8 discover system. The Pt has been grown using a thermal ALD process at 150°C, as described earlier. [47]

The measurements clearly show an increase in intensity of the diffraction peak corresponding with the (111) plane of Pt. A smaller diffraction peak corresponding to the (200) plane is also observed. In the table in figure 4.9 the values for the calculated mean size of the ordered crystalline domains are given for the (111) peak. A clear increase in domain size can be seen. As both the 60 and 100 cycle

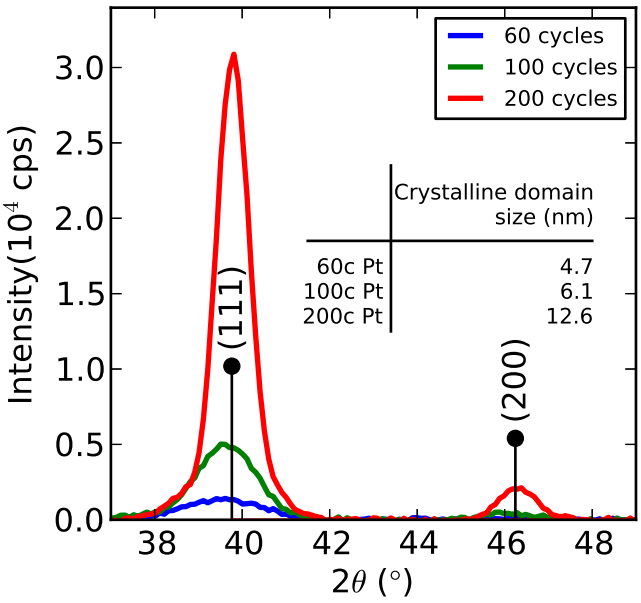

Figure 4.9: XRD pattern for respectively 60, 100 and 200 ALD cycles of Pt growth, showing the (111) and (200) diffraction peak. The inset displays a table of the domain sizes for the (111) peak calculated with the Scherrer equation (eq. 4.5). A clear increase in domain size can be seen.

sample are the exact same samples studied with GISAXS (as seen in figure 4.7), there is a nice correspondence between both techniques. Both GISAXS and XRD suggest that after 60 ALD cycles, not a lot of platinum is present (low XRD intensity, Yoneda peak at low q_z, corresponding to the critical angle of bare Si) and after 100 ALD cycles the XRD intensity is much larger, indicating platinum has been grown, as is also seen in the shift of the Yoneda peak in the GISAXS pattern to higher q_z values.

4.6 Elemental Analysis

4.6.1 X-ray Fluorescence

X-ray fluorescence(XRF) is a spectroscopy technique that is based on the excitation of core electrons by x-rays. If the energy of the incident photons is larger than the binding energy of a core electron, that electron can be emitted by the atom. This creates a vacancy, which leaves the atom in an excited state. To relax to a more stable state, an electron from an outer shell will be transfered to the vacancy. This will result in the emission of either an x-ray or an Auger electron. The emitted x-ray will have an energy corresponding to the difference in binding energy between the two shells involved. Because every element has a different set of energy levels, each element will have a specific set of fluorescence peaks. These can be used to identify the elements that are being exposed to the x-rays. This in turn allows determination of sample composition.

Because the creation of an Auger electron instead of a fluorescent x-ray is more favorable in lighter elements, the use of XRF is typically limited to elements with an atomic number larger than 11. Moreover, most window materials (Be, kapton) are only sufficiently transparent to x-rays above a certain x-ray energy. This again limits the use of XRF to heavier elements. The efficiency of x-ray absorption is greatly improved when the incident x-ray energy is slightly above the binding energy of the core electrons. The tunability of the x-ray energy at a synchrotron allows tailoring to the specific elements involved in an experiment.

In situ XRF is an interesting tool to study nucleation behavior during ALD and the growth on complex, non-planar structures. [32, 33] The high intensity of the synchrotron beam enables the detection of a very small amount of material. Therefore in situ XRF can be used to study the very first stages of ALD growth, even on planar surfaces. This has been demonstrated for the nucleation of ZnO [26] and TiO_2 [32, 33] on Si, and the growth of HfO_2 on Ge and Si [29]. Since XRF directly detects the amount of deposited material, the substrate shape has little to no influence on the measurement. This allows quantification of the amount of deposited material on high aspect ratio surfaces, where other techniques can not be used to monitor e.g. film thickness. This was shown for the growth of TiO_2 in porous silica films. [32–34]

The penetration depth of x-rays for energies typically used during XRF is on the order of microns. If the thickness of the studied layers is larger than a few 100 nm, the reabsorption of fluorescent x-rays needs to be taken into account, since this changes the relation between the intensity of the fluorescent x-rays and the amount of material. For the study of planar ALD grown thin films, this is usually not a problem, since the layers are typically much thinner than 100 nm. In the case of complex 3D structures on a support, attention has to be given to this effect, as these structures can have thicknesses of the order of several microns. Special

attention also has to be given to the substrate or support itself. If the substrate is excitable by the used x-rays, a lot of fluorescent x-rays will be created related to the substrate, which can saturate the detector. Additionally, some of the x-rays will get scattered on the sample. These elastic (Rayleigh scattering) and inelastic (mostly Compton scattering) scatted x-rays increase the death time of the detector. Both contributions can be minimized by setting the angle between the incident x-rays and the detector to 90°. To optimize the amount of fluorescence reaching the detector, the detector needs to be placed perpendicular to the sample, since the fluorescence will follow Lambert's cosine law. If we take both geometrical conditions into account, a detector position perpendicular to the sample in combination with a small incident angle is to be preferred, ensuring an angle between the incident x-rays and the detector close to 90°. However, a small incident angle creates a large footprint of the x-ray beam on the sample. To limit the loss of signal and unwanted background signals due to illumination of an area larger than the studied sample, the incident angle is usually chosen based on the maximum footprint size in relation to the sample size.

As a first example the nucleation and growth of HfO_2 is monitored for two different starting surfaces. The two studied surfaces are thermally grown SiO_2 and ALD grown Al_2O_3. HfO_2 is grown by thermal ALD at a sample temperature of 250°C.

A typical XRF spectrum after several cycles of HfO_2 deposition is shown in figure 4.10. This clearly shows that the spectrum consists of lines corresponding to the substrate (Si K_α), the HfO_2 layer (Hf L_α), scattered x-rays (10 keV) and various smaller signals from the sample holder (Co K_α and Fe K_α). The use of synchrotron based x-rays enables the detection of these small quantities of materials.

In figure 4.11 the evolution of the Hf L_α emission line is shown during the first ALD cycles on the SiO_2 surface. By integrating this peak, a measure of the deposited amount of Hf atoms can be obtained. The integrated intensities obtained for both starting surfaces are shown in figure 4.12. On the ALD grown Al_2O_3 surface substrate-enhanced growth is observed during the first 10 cycles, likely because the starting surface has a higher density of hydroxyl groups than the growing HfO_2 layer. In contrast the initial growth on the SiO_2 surface is substrate-inhibited, due to nucleation effects because the starting surface mainly contains oxygen bridges. [1] If we look at the final slope of the growth curves, linear growth is observed, as is expected for ALD. The slope of the growth curve on SiO_2 is almost twice the slope for the growth on Al_2O_3. This means that the GPC is larger on the SiO_2 surface. This can be linked to a higher surface roughness due to the delayed nucleation, which is known to result in rougher films.

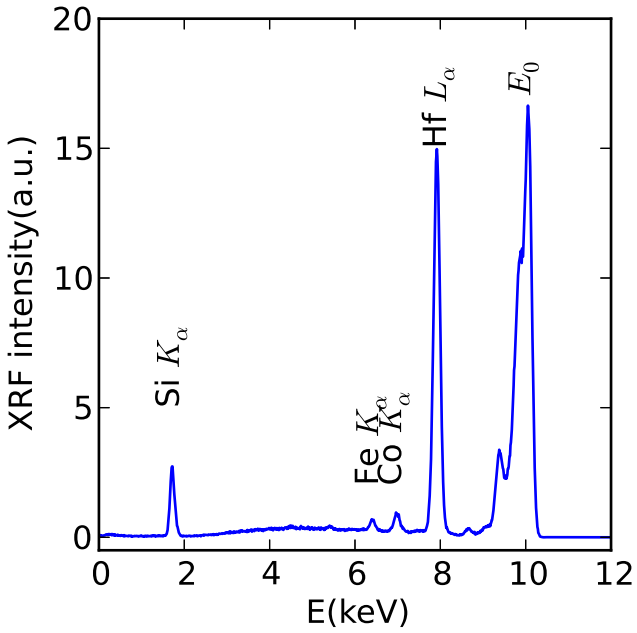

Figure 4.10: XRF spectrum for 10 ALD cycles of HfO_2 on SiO_2. Lines corresponding to the substrate (Si K_α), the HfO_2 layer (Hf L_α), scattered x-rays (10 keV) and various smaller signals from the sample holder (Co K_α and Fe K_α) can be seen. The use of synchrotron based x-rays enables the detection of these small quantities of materials.

Since XRF probes the elemental composition of a material, independent of surface morphology, the technique is ideally suited to study ALD growth on 3D structures. As an example, the thermal growth at 200° of TiO_2 on multi walled carbon nanotubes (MWCNTs) is shown. In figure 4.13 the integrated intensity of the Ti K_α peak is shown. As a reference, the growth of TiO_2 on native SiO_2 is shown. The data clearly shows that a lot more material is deposited on the MWCNTs, compared to a planar reference. This is to be expected, as the surface area of the MWCNTs is several times larger. One can also see that the growth on the MWCNTs has a nucleation period of about 20 ALD cycles. When we now compare the slope for the growth on MWCNTs and the planar reference, the apparent GPC is 55 times larger. The slope can be interpreted as a direct measure for the effective surface area. This allows an estimate of the density of MWCNTS on the sample. The diameter and length of the MWCNTs is known to be 10 nm and 6 μm respectively. If we assume that the MWCNTs are uniformly coated, a density of $3\,10^{10}$ cm^{-2} is obtained. This is a realistic value suggesting that the MWCNTs are indeed fully coated, as confirmed by cross-sectional SEM.

The use of XRF is not limited to monitoring material that gets added during

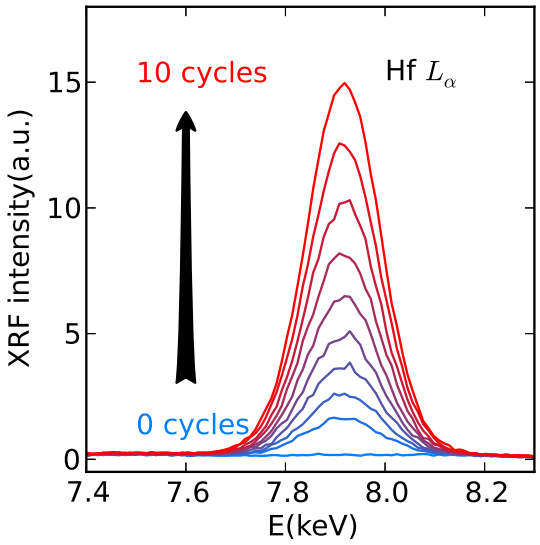

Figure 4.11: Evolution of the Hf L_α emission line measured during the 10 first ALD cycles of HfO_2 growth on SiO_2.

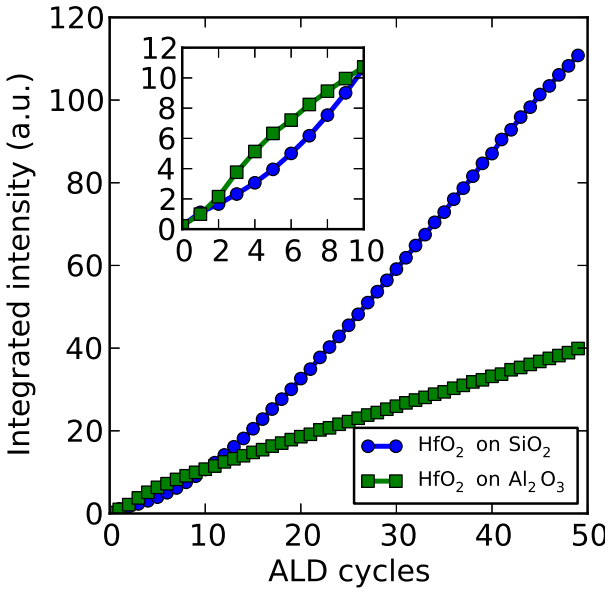

Figure 4.12: Integrated intensity of the Hf L_α emission line as a function of ALD cycles for the growth of HfO_2 on SiO_2 and Al_2O_3.

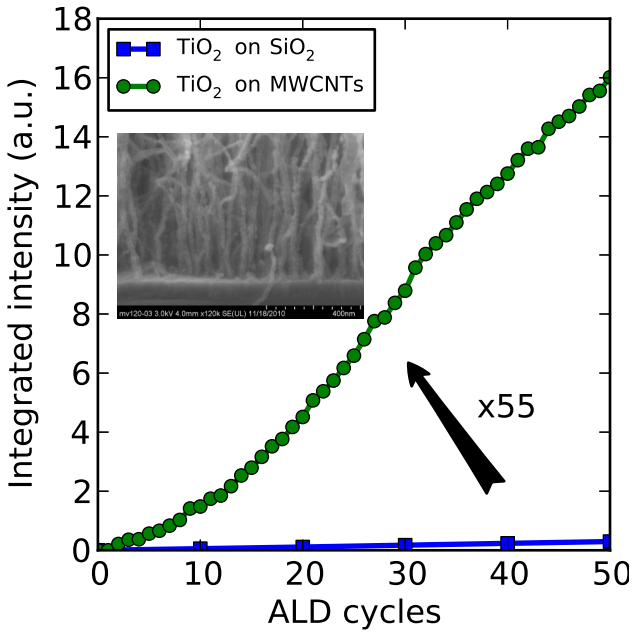

Figure 4.13: Integrated intensity of the Ti K_α emission line, measured during TiO_2 growth on MWCNTs and a silicon reference. The growth on the MWCNTs has a nucleation period of about 20 ALD cycles. The final slope of the growth curve on the MWCNTs is 55 times larger than the slope of the reference curve, indicating a surface area increase for the MWCNTs as compared to the planar reference. The inset is a SEM picture of the coated MWCNTs, showing a uniform coating on the MWCNTs up to the supporting surface at the bottom.

ALD. It can also be used to analyze etching behavior. TMA is known from literature to etch ZnO. [67] We will show this effect with in situ XRF measurements. First a ZnO layer was grown on an anodized alumina (AAO) substrate. This ensures a larger surface area, resulting in larger signals. In figure 4.14 the evolution of the intensity of the Zn K_α emission line is shown under TMA exposure at $5\,10^{-3}$ mbar. The XRF signal indicates the removal of Zn atoms by TMA.

A final example discusses in situ XRF measurements performed during the growth of ZnO in a mesoporous silica film. This is the exact same deposition that was previously discussed in the GISAXS section. The Zn K_α line is integrated to monitor the growth in the porous material, as shown in figure 4.15. From the growth curve it is clear that during the first 5 cycles a much larger surface is available for ALD growth. During these first ALD cycles the pores are accessible to the ALD precursors, making the internal surface available for growth. After 5 ALD cycle the pores are closed to the ALD precursors and growth only continues on top

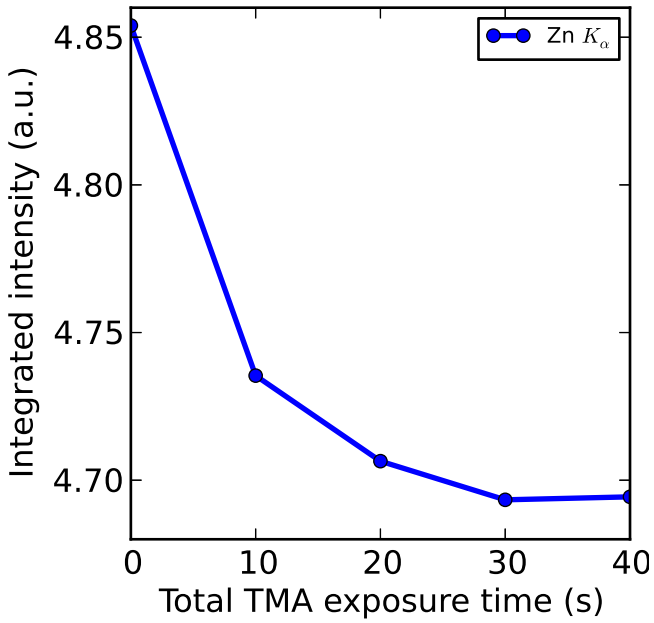

Figure 4.14: Integrated intensity of the Zn K_α emission line under TMA exposure at 5 10^{-3} mbar, showing the etching behavior of TMA on ZnO.

of the porous film, indicated by the lower slope after 5 ALD cycles.

4.7 Chemical Analysis

For completeness, X-ray absorption spectroscopy (XAS) and X-ray photoelectron spectroscopy (XPS) will be briefly introduced. These techniques can provide information about the local chemical state during ALD growth. They have so far not been reported as in situ techniques, but are instead used for 'in vacuo' experiments, where deposition and characterization are performed in separate chambers with vacuum transfer. While the vacuum transfer avoids air exposure, it does impose limitations. The most important being that the transfer of the sample from one chamber to the other obviously takes some time. Since most half reactions during ALD growth generally result in a stable state in UHV, the time in between cycles or half cycles can be increased to allow this transfer. However certain processes, where the intermediate state after a half reaction is less stable, can't be studied in this way. An example is the growth of Pt with a N_2 or NH_3 plasma. In this case the active species on the surface are removed over time. [68] This only allows for a small time window in between (half-)cycles to perform in vacuo measure-

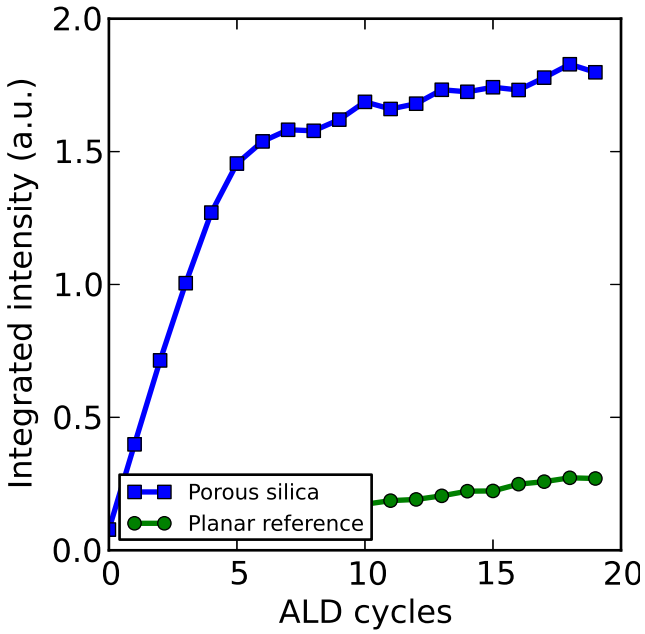

Figure 4.15: Integrated intensity of the Zn K_α emission line during growth of ZnO in a porous silica film. During the first 5 cycles growth is occurring on the internal surface, indicated by the larger slope. After 5 cycles, ZnO is grown on top of the film. The growth on a planar Si surface is shown as a reference.

ments. A second consideration has to be made with regard to sample temperature during transfer and analysis. The amount of surface groups are known to depend on the sample temperature. Most ALD processes are dependent on the interaction with these groups. This implies that changes in sample temperature during transfer and analysis can have a significant influence on the ALD process. By addressing these issues, an in vacuo experiment may provide useful insights, not accessible with true in situ techniques. The discussion of XAS and XPS will be limited to a general introduction and a brief prospect of the in situ use of these techniques.

4.7.1 X-ray Absorption Spectroscopy

In X-ray absorption spectroscopy (XAS) one measures the absorption of x-rays by a material as a function of energy to obtain detailed structural and electronic information through extended X-ray absorption fine structure (EXAFS) and X-ray absorption near edge structure (XANES) respectively [69]. Classically XAS is performed by looking at the transmitted x-ray intensity through a material. The

transmission is then given by the Beer-Lambert law,

$$I_t = I_0 e^{-\mu(E)t} \tag{4.6}$$

with the absorption coefficient $\mu(E)$ as function of the energy and the thickness of the material t. Generally x-ray absorption decreases smoothly for increasing energy. But if the energy of the x-rays become large enough, an electron from an inner shell of the material can be excited, like already explained for XRF. This will give rise to a sharp increase in absorption at the specific binding energy of the core electron. This increase is denoted as the absorption edge or threshold energy. The emitted electron will have a kinetic energy ($E_{kinetic}$) corresponding to the photoelectric effect.

$$E_{kinetic} = h\nu - E_{binding} \tag{4.7}$$

Quantum mechanically the outgoing photoelectron can be represented as a spherical wave. This wave will scatter on the surrounding atoms (specifically the electron densities), producing a backscattered wave. This outgoing and backscattered waves interfere, causing an interference pattern. The distance to the neighboring atoms determines the interference pattern. As a result, the absorption coefficient above the absorption edge is defined as

$$\mu = \mu_0 + \chi_{(EX)} \tag{4.8}$$

with μ_0 representing the atomic background. $\chi_{(EX)}$ describes the scattering of the outgoing electron against the neighboring atoms. It is called the EXAFS function. This oscillatory part of the absorption coefficient contains information about the local structure around the absorber atom. Since the electrons only get excited around a specific energy, XAS is element specific.

As an alternative to measuring the x-ray transmission, the fluorescence can be studied. Since the fluorescence intensity is closely related to the absorption coefficient, the same information can be obtained. This is important when we want to apply XAS as an in situ technique during ALD. When studying thin films, an absorption measurement will only see a very small change in transmission, due to the limited amount of absorbing material in the film. This will result in a low signal to noise ratio. The fluorescent signal on the other hand will even be available when only little material is present.

The use of XAS has been reported as an ex situ technique [70–72]. There are also reports of XAS as an in vacuo technique, where the sample can be transfered from the ALD chamber to an UHV system to allow for XAS. [36–39] To the best of our knowledge the use of XAS as an in situ technique, has been performed once on powderous supports in absorption mode [40] and once studying ALD growth on a planar support in fluorescence mode [41].

4.7.2 X-ray Photoelectron Spectroscopy

X-ray photoelectron spectroscopy (XPS) is a technique that allows the study of composition and chemical state of the elements in a material. XPS is based on the photoelectric effect (equation 4.7). The material gets illuminated with x-rays at a fixed energy (E_{photon}). These x-rays will interact with the electrons in the shells of the illuminated atoms. These electrons can get emitted if E_{photon} is larger than the electron binding energy ($E_{binding}$). The surplus in energy will be converted into kinetic energy ($E_{kinetic}$) of the photo electron. These electrons can then be collected and analyzed. This leads to the following equation used for XPS analysis.

$$E_{binding} = E_{photon} - (E_{kinetic} - \Phi) \tag{4.9}$$

Here Φ is the work function of the spectrometer. Every element has a characteristic set of peaks at specific $E_{binding}$. This allows for an elemental analysis of a sample. As $E_{binding}$ also depends on the chemical state of the involved atoms, XPS can be used to determine the local bonding of atoms.

Since only electrons created at the surface exit the material unaltered, the information depth of XPS is limited to a few nanometers. From an ALD point of view this can be considered an advantage for in situ analysis, since we are only interested in the very top surface. Because XPS is based on the collection of electrons, UHV is needed. This is a very important hurdle when it comes to implementing XPS as an in situ technique. Moreover, fragile detection electronics are in direct contact with the vacuum of the analysis chamber. If we would implement ALD inside an XPS chamber, the UHV conditions would be very hard to achieve and special care would have to be made to protect the detector from the ALD process. This directly explains why no use of XPS as in situ technique has been reported in literature. There are however several examples of the use of XPS as in vacuo technique, meaning that the sample gets transfered from an ALD chamber to an XPS analysis chamber under UHV conditions. [37, 38, 42–45] However the development of high pressure XPS and ambient pressure XPS systems, as are currently pioneered for in situ studies during catalysis, could make in situ XPS possible under ALD conditions. [73]

4.8 Practical Considerations of Synchrotron Use

The use of synchrotron radiation obviously also comes with a few disadvantages. If the flux on the sample is too high and the sample is sensitive to x-rays, the surface might get altered, changing the ALD process that is being monitored. Limiting the flux to the sample, increasing the footprint of the x-ray beam and blocking the sample from x-rays when no measurements are being performed, reduce the x-ray effects. Possible decomposition of the gas molecules by x-rays can be avoided by only allowing illumination when the reactor has been purged/pumped.

Secondly, at least two x-ray transparent windows need to be incorporated into the reactor design. Because of the conformal nature of ALD these windows either need to be protected by valves during gas exposures or need to be considered as consumables. Since in most cases the temperature of the windows will be limited, either by heating efficiency and/or the practical upper limit to the allowed temperature of the window, in practice most ALD processes will deposit very little material on the windows.

Thirdly, since synchrotron facilities only have a limited amount of available time compared to the demand from various scientific areas, a request has to be made for experimental time. Due to selection procedures and scheduling, in most cases a few months up to more than half a year can pass between application for experimental time and the actual experiment. Additionally, as a multi-user facility, safety is a key issue at a synchrotron facility, both concerning the involved chemicals and the interface between the beamline equipment and the in situ ALD reactor. Communication with beamline staff can be of great help to make an estimate of the feasibility of your experiment at a specific facility.

4.9 Reactor Design

Design of an ALD reactor that allows for in situ synchrotron studies asks for some specific adaptations and changes to a standard ALD reactor. A lot of experience exists within the field of catalysis, where a multitude of operando reaction cells have been designed over the last decades for operando EXAFS or XRD during catalytic reactions. These reaction cells typically use a heating stage to heat the catalyst up to 500°C and work under a wide range of gas ambients [74–76]. This can be translated to an ALD design, where typically similar requirements need to be met. In figure 4.16 a schematic representation of an ALD chamber, adapted for various in situ synchrotron based techniques is shown.

Currently several chambers have already been used to perform x-ray studies during ALD, both flow type reactors [24, 26], and pump type reactors [29, 32–34]. A few issues that need to be addressed when adapting or designing these chambers will be briefly discussed.

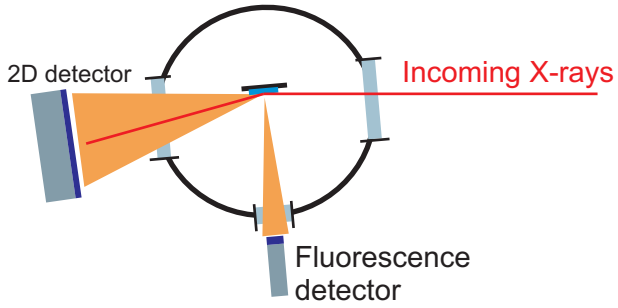

Figure 4.16: Schematic view of an ALD chamber for in situ x-ray experiments.

As the x-ray source in the case of synchrotron experiments is fixed, changing the incident angle needs to be achieved by either mounting the full ALD chamber on a movable stage and/or incorporating a movable sample stage into the design. Even if only measurements at a fixed position will be performed, still some rotational and/or translational freedom is required, in order to align the x-ray beam with the chamber.

Windows need to be incorporated into the chamber design to allow x-rays to pass from the source to the sample and back to a detector. In most cases either beryllium or kapton windows are used as these materials are sufficiently transparent in the keV energy range. The transmission of both materials is shown in figure 4.17 for typical window thicknesses. The transmission of silicon is added for comparison. In general thinner windows are preferred, because they allow for the highest transmission. However, depending on the size of the needed window, the strength of the window needs to be taken into account, as in most cases, the window needs to withstand around one atmosphere in pressure difference. This directly results in a minimal window thickness for a given diameter.

Clever use of the x-ray transmission properties of various materials isn't limited to the selection of window materials. If unwanted x-rays at a specific energy are preventing accurate in situ measurements, a filter material can be placed either directly in front of the entrance window or in front of the detector. As an example, the effect of a molybdenum filter on the fluorescent spectrum of an ALD grown HfO_2 layer on InP is shown in figure 4.18. Without the filter, the fluorescence from the indium saturates the detector, resulting in a spectrum where only indium can be detected. If a 2 μm thick Mo filter is positioned in front of the fluorescence detector, most of the x-rays at energies below 5 keV are blocked, reducing the amount of fluorescence form the In substrate reaching the detector. On the other hand, the fluorescence coming from the Hf atoms in the HfO_2 layer are only partially absorbed. This results in a detectable Hf L_α line, without saturating the detector, allowing the study of HfO_2 growth on InP with in situ XRF.

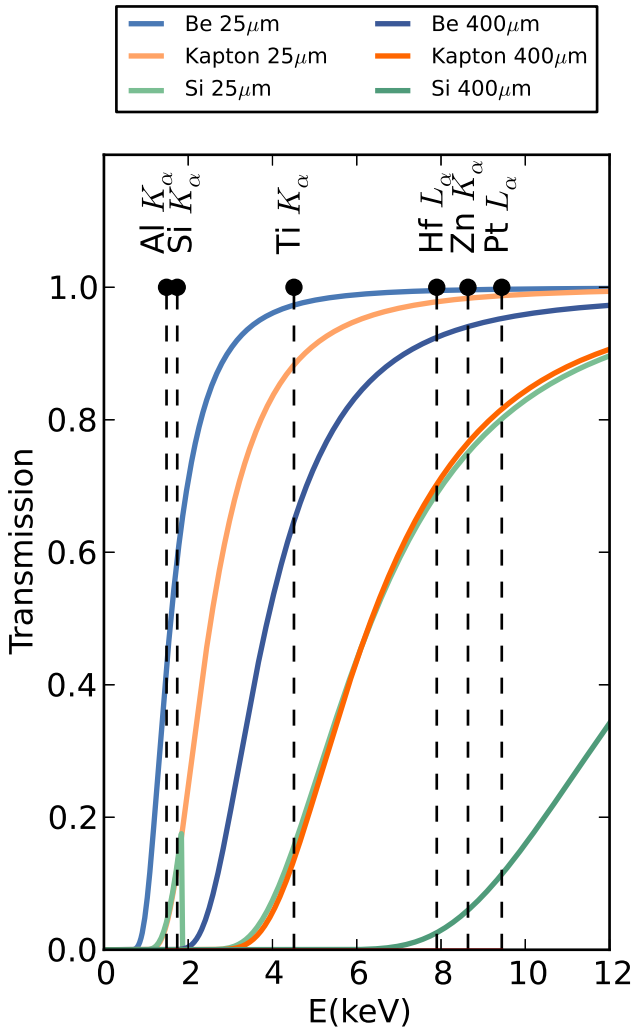

Figure 4.17: Transmission for Be, Kapton and Silicon of a thickness of 25 µm and 400 µm. Some fluorescent lines are added for materials that are frequently grown by ALD.

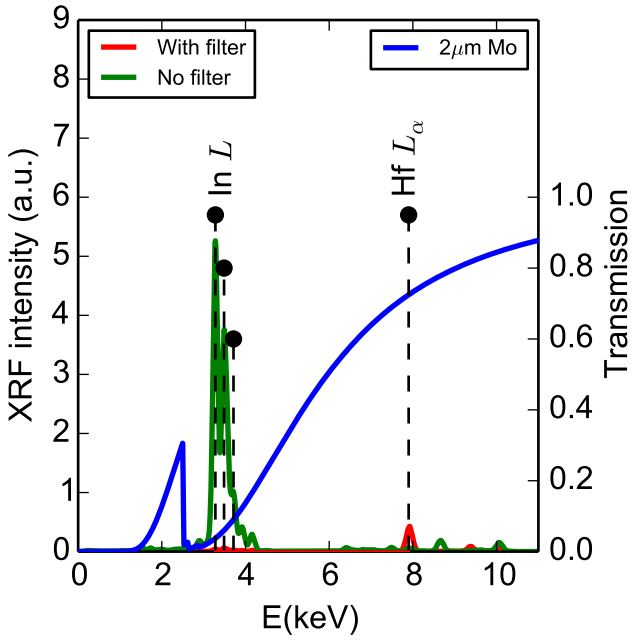

Figure 4.18: XRF spectrum for a HfO_2 layer on InP, with and without molybdenum filter. The theoretical transmission of the Mo filter is overlayed. Without filter, only indium and no hafnium can be detected. With filter, the Hf L_α line is clearly visible and the In L lines are greatly reduced.

4.10 Conclusions

Extending the wavelength range of optical in situ techniques to x-rays enables the use of XRR, XRF and XPS during ALD. This expands the information available in the study of layer growth during ALD, both on planar and on complex structures. The use of synchrotron based x-rays is beneficial to in situ studies, because of the high photon flux and the energy tunability, enabling GISAXS and XAS.

All these techniques are especially sensitive to changes on the (sub-)nanometer scale. As the changes during growth are typically of this order, they are ideally suited for in situ studies of ALD. The range of x-ray techniques available allows the study of specific facets of the processes involved in ALD. These techniques can complement well established techniques in determining e.g. thicknesses, densities and crystallinity and/or provide in situ information, unavailable to other techniques, e.g. morphology.

In short, in situ synchrotron based x-ray techniques form a new set of valuable tools in monitoring atomic layer deposition.

4.11 Acknowledgements

The research leading to these results has received funding from the European Research Council under the European Union's Seventh Framework Programme (FP7/2007-2013) / ERC grant agreement n° 239865. Christophe Detavernier and Jolien Dendooven also acknowledge funding by FWO-Vlaanderen, BOF-UGent and GOA n° 01G01513. Karl Ludwig acknowledges funding by the U.S. Department of Energy, under Contract n° DE-FG02-03ER46037. Use of the National Synchrotron Light Source, Brookhaven National Laboratory, was supported by the U.S. Department of Energy, Office of Science, Office of Basic Energy Sciences, under Contract n° DE-AC02-98CH10886.

References

[1] R. L. Puurunen. *Surface Chemistry of Atomic Layer Deposition: A Case Study for the Trimethylaluminum/Water Process*. Journal of Applied Physics, 97(12):121301, 2005.

[2] S. M. George. *Atomic Layer Deposition: An Overview.* Chemical reviews, 110(1):111–31, January 2010.

[3] C. Detavernier, J. Dendooven, S. P. Sree, K. F. Ludwig, and J. A. Martens. *Tailoring Nanoporous Materials by Atomic Layer Deposition.* Chemical Society reviews, 40(11):5242–53, December 2011.

[4] V. Miikkulainen, M. Leskela, M. Ritala, and R. L. Puurunen. *Crystallinity of Inorganic Films Grown by Atomic Layer Deposition: Overview and General Trends*. Journal of Applied Physics, 113(2):021301, 2013.

[5] J. W. Elam, M. D. Groner, and S. M. George. *Viscous Flow Reactor With Quartz Crystal Microbalance for Thin Film Growth by Atomic Layer Deposition*. Review of Scientific Instruments, 73(8):2981, 2002.

[6] M. N. Rocklein and S. M. George. *Temperature-Induced Apparent Mass Changes Observed During Quartz Crystal Microbalance Measurements of Atomic Layer Deposition*. Analytical Chemistry, 75(19):4975–4982, October 2003.

[7] A. Rahtu and M. Ritala. *Reaction Mechanism Studies on Titanium IsopropoxideWater Atomic Layer Deposition Process*. Chemical Vapor Deposition, 8(1):21, January 2002.

[8] R. Matero, A. Rahtu, and M. Ritala. *In Situ Quadrupole Mass Spectrometry and Quartz Crystal Microbalance Studies on the Atomic Layer Deposition of Titanium Dioxide From Titanium Tetrachloride and Water*. Chemistry of Materials, 13(12):4506–4511, December 2001.

[9] M. Schuisky, J. W. Elam, and S. M. George. *In Situ Resistivity Measurements During the Atomic Layer Deposition of ZnO and W Thin Films*. Applied Physics Letters, 81(1):180, 2002.

[10] O. Nilsen and H. Fjellvå g. *Measuring the Heat Evolved From Individual Reaction Steps in Atomic Layer Deposition*. Journal of Thermal Analysis and Calorimetry, 105(1):33–37, May 2011.

[11] M. Juppo, A. Rahtu, M. Ritala, and M. Leskelä. *In Situ Mass Spectrometry Study on Surface Reactions in Atomic Layer Deposition of Al_2O_3 Thin*

Films From Trimethylaluminum and Water. Langmuir, 16(8):4034–4039, April 2000.

[12] H. Kim, A. J. Kellock, and S. M. Rossnagel. *Growth of Cubic-TaN Thin Films by Plasma-Enhanced Atomic Layer Deposition*. Journal of Applied Physics, 92(12):7080, 2002.

[13] A. J. M. Mackus, S. B. S. Heil, E. Langereis, H. C. M. Knoops, M. C. M. van de Sanden, and W. M. M. Kessels. *Optical Emission Spectroscopy as a Tool for Studying, Optimizing, and Monitoring Plasma-Assisted Atomic Layer Deposition Processes*. Journal of Vacuum Science and Technology A: Vacuum, Surfaces, and Films, 28(1):77, 2010.

[14] R. K. Grubbs, N. J. Steinmetz, and S. M. George. *Gas Phase Reaction Products During Tungsten Atomic Layer Deposition Using WF_6 and Si_2H_6*. Journal of Vacuum Science and Technology B: Microelectronics and Nanometer Structures, 22(4):1811, 2004.

[15] N. Kobayashi and Y. Kobayashi. *In Situ Monitoring and Control of Atomic Layer Epitaxy by Surface Photo-Absorption*. Thin Solid Films, 225(1-2):32–39, March 1993.

[16] K. Nishi, A. Usui, and H. Sakaki. *In Situ Optical Characterization of GaAs Surfaces Under Alternating Supply of GaCl and AsH_3*. Applied physics letters, 1:31–33, 1992.

[17] J. W. Klaus, S. J. Ferro, and S. M. George. *Atomic Layer Deposition of Tungsten Nitride Films Using Sequential Surface Reactions*. Journal of The Electrochemical Society, 147(3):1175, 2000.

[18] S. Yokoyama, H. Goto, T. Miyamoto, N. Ikeda, and K. Shibahara. *Atomic Layer Controlled Deposition of Silicon Nitride and in Situ Growth Observation by Infrared Reflection Absorption Spectroscopy*. Applied Surface Science, 112:75–81, March 1997.

[19] A. C. Dillon, A. Ott, J. Way, and S. M. George. *Surface Chemistry of In_2O_3 Deposition Using $In(CH_3)_3$ and H_2O in a Binary Reaction Sequence*. Surface science, 322:230–242, 1995.

[20] E. Langereis, S. B. S. Heil, M. C. M. van de Sanden, and W. M. M. Kessels. *In Situ Spectroscopic Ellipsometry Study on the Growth of Ultrathin TiN Films by Plasma-Assisted Atomic Layer Deposition*. Journal of Applied Physics, 100(2):023534, 2006.

[21] J. Dendooven, K. Devloo-Casier, E. Levrau, R. Van Hove, S. P. Sree, M. R. Baklanov, J. A. Martens, and C. Detavernier. *In Situ Monitoring of Atomic Layer Deposition in Nanoporous Thin Films Using Ellipsometric Porosimetry.* Langmuir, 28(8):3852–9, February 2012.

[22] Y. Hwang, K. Heo, C. H. Chang, M. K. Joo, and M. Ree. *Synchrotron X-Ray Reflectivity Study of High Dielectric Constant Alumina Thin Films Prepared by Atomic Layer Deposition*. Thin Solid Films, 510(1-2):159–163, July 2006.

[23] J. P. Yong, R. L. Dong, and B. Sunggi. *Synchrotron X-Ray Reflectivity for Characterization of the Initial ALD Growth of TaN*. Journal of the Korean Physical Society, 59(21):458, August 2011.

[24] Y. J. Park, D. R. Lee, H. H. Lee, H.-B.-R. Lee, H. Kim, G.-C. Park, S.-W. Rhee, and S. Baik. *In-Situ Synchrotron X-Ray Scattering Study of Thin Film Growth by Atomic Layer Deposition.* Journal of nanoscience and nanotechnology, 11(2):1577–80, February 2011.

[25] T.-B. Hur, Y.-H. Hwang, H.-K. Kim, and H.-L. Park. *Study of the Structural Evolution in ZnO Thin Film by in Situ Synchrotron X-Ray Scattering*. Journal of Applied Physics, 96(3):1740, 2004.

[26] D. D. Fong, J. a. Eastman, S. K. Kim, T. T. Fister, M. J. Highland, P. M. Baldo, and P. H. Fuoss. *In Situ Synchrotron X-Ray Characterization of ZnO Atomic Layer Deposition*. Applied Physics Letters, 97(19):191904, 2010.

[27] H.-B.-R. Lee, Y. J. Park, S. Baik, and H. Kim. *Initial Stage Growth During Plasma-Enhanced Atomic Layer Deposition of Cobalt*. Chemical Vapor Deposition, 18(1-3):41–45, 2012.

[28] J. Dendooven, K. Devloo-Casier, M. Ide, K. Grandfield, K. F. Ludwig, S. Bals, P. Van Der Voort, and C. Detavernier. *In Situ Study of ALD Processes Using Synchrotron-Based X-Ray Fluorescence and Scattering Techniques*. ECS Transactions, 50(13):35–42, March 2013.

[29] K. Devloo-Casier, J. Dendooven, K. F. Ludwig, G. Lekens, J. DHaen, and C. Detavernier. *In Situ Synchrotron Based X-Ray Fluorescence and Scattering Measurements During Atomic Layer Deposition: Initial Growth of HfO_2 on Si and Ge Substrates*. Applied Physics Letters, 98(23):231905, 2011.

[30] S.-J. Park, W.-H. Kim, W. Maeng, Y. Yang, C. Park, H. Kim, K.-N. Lee, S.-W. Jung, and W. Seong. *Effect Oxygen Exposure on the Quality of Atomic Layer Deposition of Ruthenium From Bis(cyclopentadienyl)ruthenium and Oxygen*. Thin Solid Films, 516(21):7345–7349, September 2008.

[31] R. Methaapanon and S. Geyer. *Size Dependent Effects in Nucleation of Ru and Ru Oxide Thin Films by Atomic Layer Deposition Measured by Synchrotron Radiation X-Ray Diffraction*. Chemistry of Materials, page 130823132930007, August 2013.

[32] J. Dendooven, D. Deduytsche, S. Pulinthanathu Sree, T. Korànyi, G. Vanbutsele, J. A. Martens, K. F. Ludwig, and C. Detavernier. *In Situ X-Ray Fluorescence Measurements During ALD on Flat Substrates and in Nanoporous Catalyst Support Materials.* In AVS Topical Conference on ALD, Seoul, South Korea, 2010.

[33] J. Dendooven, S. Pulinthanathu Sree, K. De Keyser, D. Deduytsche, J. A. Martens, K. F. Ludwig, and C. Detavernier. *In Situ X-Ray Fluorescence Measurements During Atomic Layer Deposition: Nucleation and Growth of TiO_2 on Planar Substrates and in Nanoporous Films*. The Journal of Physical Chemistry C, 115(14):6605–6610, April 2011.

[34] J. Dendooven, B. Goris, K. Devloo-Casier, E. Levrau, E. Biermans, M. R. Baklanov, K. F. Ludwig, P. V. D. Voort, S. Bals, and C. Detavernier. *Tuning the Pore Size of Ink-Bottle Mesopores by Atomic Layer Deposition*. Chemistry of Materials, 24(11):1992–1994, June 2012.

[35] E. Levrau, K. Devloo-Casier, J. Dendooven, K. F. Ludwig, P. Verdonck, J. Meersschaut, M. R. Baklanov, and C. Detavernier. *Atomic Layer Deposition of TiO_2 on Surface Modified Nanoporous Low-K Films.* Langmuir : the ACS journal of surfaces and colloids, 29(39):12284–12289, October 2013.

[36] M. Tallarida, K. Karavaev, and D. Schmeisser. *The Initial Atomic Layer Deposition of HfO_2/Si(001) as Followed in Situ by Synchrotron Radiation Photoelectron Spectroscopy*. Journal of Applied Physics, 104(6):064116, 2008.

[37] M. Tallarida and D. Schmeisser. *In Situ ALD Experiments With Synchrotron Radiation Photoelectron Spectroscopy*. Semiconductor Science and Technology, 27(7):074010, July 2012.

[38] R. Methaapanon, S. M. Geyer, C. Hagglund, P. a. Pianetta, and S. F. Bent. *Portable Atomic Layer Deposition Reactor for in Situ Synchrotron Photoemission Studies.* The Review of scientific instruments, 84(1):015104, January 2013.

[39] M. Tallarida, K. Karavaev, and D. Schmeisser. *HfO_2/Si Interface Formation in Atomic Layer Deposition Films: An in Situ Investigation*. Journal of Vacuum Science and Technology B: Microelectronics and Nanometer Structures, 27(1):300, 2009.

[40] W. Setthapun, W. D. Williams, S. M. Kim, H. Feng, J. W. Elam, F. A. Rabuffetti, K. R. Poeppelmeier, P. C. Stair, E. A. Stach, F. H. Ribeiro, J. T. Miller, and C. L. Marshall. *Genesis and Evolution of Surface Species During Pt Atomic Layer Deposition on Oxide Supports Characterized by in Situ XAFS Analysis and Water-Gas Shift Reaction*. The Journal of Physical Chemistry C, 114(21):9758–9771, June 2010.

[41] M. Filez, H. Poelman, R. K. Ramachandran, J. Dendooven, K. Devloo-Casier, E. Fonda, C. Detavernier, and G. B. Marin. *In Situ XAS and XRF Study of Nanoparticle Nucleation During Ozone-Based Pt Deposition.* In European Materials Research Society (E-Mrs) Spring Meeting 2013, 2013.

[42] S. M. Geyer, R. Methaapanon, B. Shong, P. a. Pianetta, S. F. Bent, and A. Piero. *Supporting Information for : In Vacuo Photoemission Studies of Platinum Atomic Layer Deposition Using Synchrotron Radiation Acquisition of Photoemission Spectra*. The Journal of Physical Chemistry Letters, 4(1):3–4, January 2013.

[43] M. Kobayashi, P. T. Chen, Y. Sun, N. Goel, P. Majhi, M. Garner, W. Tsai, P. Pianetta, and Y. Nishi. *Synchrotron Radiation Photoemission Spectroscopic Study of Band Offsets and Interface Self-Cleaning by Atomic Layer Deposited HfO_2 on $In_{0.53}Ga_{0.47}As$ and $In_{0.52}Al_{0.48}As$*. Applied Physics Letters, 93(18):182103, 2008.

[44] K. Kolanek, M. Tallarida, M. Michling, and D. Schmeisser. *In Situ Study of the Atomic Layer Deposition of HfO_2 on Si*. Journal of Vacuum Science and Technology A: Vacuum, Surfaces, and Films, 30(1):01A143, 2012.

[45] M. Tallarida, C. Adelmann, A. Delabie, S. V. Elshocht, M. Caymax, and D. Schmeisser. *GaAs Clean Up Studied With Synchrotron Radiation Photoemission*. IOP Conference Series: Materials Science and Engineering, 41:012003, December 2012.

[46] G. Ozaydin, A. S. Ozcan, Y. Wang, K. F. Ludwig, H. Zhou, R. L. Headrick, and D. P. Siddons. *Real-Time X-Ray Studies of Mo-Seeded Si Nanodot Formation During Ion Bombardment*. Applied Physics Letters, 87(16):163104, 2005.

[47] J. Dendooven, R. K. Ramachandran, K. Devloo-Casier, G. Rampelberg, M. Filez, H. Poelman, G. B. Marin, E. Fonda, and C. Detavernier. *Low-Temperature Atomic Layer Deposition of Platinum Using (Methylcyclopentadienyl)trimethylplatinum and Ozone*. The Journal of Physical Chemistry C, 117(40):20557–20561, October 2013.

[48] P. Croce, G. Devant, M. Sere, and M. Verhaeghe. *Thin Film Surface Studies by X-Ray Reflection*. Surface Science, 22(April 1969):173–186, 1970.

[49] E. Chason and T. M. Mayer. *Thin Film and Surface Characterization by Specular X-Ray Reflectivity*. Critical Reviews in Solid State and Materials Sciences, 22(1):1–67, March 1997.

[50] L. Parratt. *Surface Studies of Solids by Total Reflection of X-Rays*. Physical Review, 95(2):359–369, July 1954.

[51] J. R. Levine, J. B. Cohen, Y. W. Chung, and P. Georgopoulos. *Grazing-Incidence Small-Angle X-Ray Scattering: New Tool for Studying Thin Film Growth*. Journal of Applied Crystallography, 22(6):528–532, December 1989.

[52] G. Renaud, R. Lazzari, and F. Leroy. *Probing Surface and Interface Morphology With Grazing Incidence Small Angle X-Ray Scattering*. Surface Science Reports, 64(8):255–380, August 2009.

[53] D. Heggie and R. Mathieu. *X-Ray and Neutron Reflectivity*, volume 770 of *Lecture Notes in Physics*. Springer Berlin Heidelberg, Berlin, Heidelberg, 2009.

[54] Y. Yoneda. *Anomalous Surface Reflection of X Rays*. Physical review, 131(5), 1963.

[55] S. Dourdain, J.-F. Bardeau, M. Colas, B. Smarsly, A. Mehdi, B. M. Ocko, and A. Gibaud. *Determination by X-Ray Reflectivity and Small Angle X-Ray Scattering of the Porous Properties of Mesoporous Silica Thin Films*. Applied Physics Letters, 86(11):113108, 2005.

[56] G. Renaud, R. Lazzari, C. Revenant, A. Barbier, M. Noblet, O. Ulrich, F. Leroy, J. Jupille, Y. Borensztein, C. R. Henry, J.-P. Deville, F. Scheurer, J. Mane-Mane, and O. Fruchart. *Real-Time Monitoring of Growing Nanoparticles.* Science, 300(5624):1416–9, May 2003.

[57] G. Ozaydin, K. F. Ludwig, H. Zhou, L. Zhou, and R. L. Headrick. *Transition Behavior of Surface Morphology Evolution of Si(100) During Low-Energy Normal-Incidence Ar^+ Ion Bombardment*. Journal of Applied Physics, 103(3):033512, 2008.

[58] S. T. Christensen, J. W. Elam, B. Lee, Z. Feng, M. J. Bedzyk, and M. C. Hersam. *Nanoscale Structure and Morphology of Atomic Layer Deposition Platinum on $SrTiO_3$ (001)*. Chemistry of Materials, 21(3):516–521, February 2009.

[59] R. Lazzari. *IsGISAXS: A Tool for Grazing Incidence Small Angle X-Ray Scattering Analysis for Nanostructures*. Journal of Applied Crystallography, 35:406–421, 2002.

[60] J. Dendooven. *Modeling and in Situ Characterization of the Conformality of Atomic Layer Deposition in High Aspect Ratio Structures and Nanoporous Materials*. PhD thesis, Ghent University, 2012.

[61] V. Lujala, J. Skarp, M. Tammenmaa, and T. Suntola. *Atomic Layer Epitaxy Growth of Doped Zinc Oxide Thin Films From Organometals*. Applied surface science, 4332(94):0–6, 1994.

[62] N. Terasawa, K. Akimoto, Y. Mizuno, A. Ichimiya, K. Sumitani, T. Takahashi, X. Zhang, H. Sugiyama, H. Kawata, T. Nabatame, and A. Toriumi. *Crystallization Process of High-K Gate Dielectrics Studied by Surface X-Ray Diffraction*. Applied Surface Science, 244(1-4):16–20, May 2005.

[63] H.-B.-R. Lee and H. Kim. *High-Quality Cobalt Thin Films by Plasma-Enhanced Atomic Layer Deposition*. Electrochemical and Solid-State Letters, 9(11):G323, 2006.

[64] W.-H. Kim, H.-B.-R. Lee, K. Heo, Y. K. Lee, T.-M. Chung, C. G. Kim, S. Hong, J. Heo, and H. Kim. *Atomic Layer Deposition of Ni Thin Films and Application to Area-Selective Deposition*. Journal of The Electrochemical Society, 158(1):D1, 2011.

[65] P. Alén. *Atomic Layer Deposition of TaN , NbN , and MoN Films for Cu Metallizations*. PhD thesis, University of Helsinki, 2005.

[66] L. Borgese, M. Gelfi, E. Bontempi, P. Goudeau, G. Geandier, D. Thiaudière, and L. Depero. *Young Modulus and Poisson Ratio Measurements of TiO_2 Thin Films Deposited With Atomic Layer Deposition*. Surface and Coatings Technology, 206(8-9):2459–2463, January 2012.

[67] J. W. Elam and S. M. George. *Growth of ZnO/Al_2O_3 Alloy Films Using Atomic Layer Deposition Techniques*. Chemistry of Materials, 15(4):1020–1028, February 2003.

[68] D. Longrie, K. Devloo-Casier, D. Deduytsche, S. Van den Berghe, K. Driesen, and C. Detavernier. *Plasma-Enhanced ALD of Platinum With O_2, N_2 and NH_3 Plasmas*. ECS Journal of Solid State Science and Technology, 1(6):Q123–Q129, October 2012.

[69] D. Koningsberger and B. Mojet. *XAFS Spectroscopy; Fundamental Principles and Data Analysis*. Topics in catalysis, 10:143–155, 2000.

[70] M. Han, Y. Luo, J. Moryl, R. Osgood, and J. Chen. *A Near-Edge X-Ray Absorption Fine Structure Study of Atomic Layer Epitaxy: The Chemistry of the Growth of CdS Layers on ZnSe(100)*. Surface Science, 415(3):251–263, October 1998.

[71] S. T. Christensen, H. Feng, J. L. Libera, N. Guo, J. T. Miller, P. C. Stair, and J. W. Elam. *Supported Ru-Pt Bimetallic Nanoparticle Catalysts Prepared by Atomic Layer Deposition.* Nano letters, 10(8):3047–51, August 2010.

[72] S. T. Christensen, J. W. Elam, F. a. Rabuffetti, Q. Ma, S. J. Weigand, B. Lee, S. Seifert, P. C. Stair, K. R. Poeppelmeier, M. C. Hersam, and M. J. Bedzyk. *Controlled Growth of Platinum Nanoparticles on Strontium Titanate Nanocubes by Atomic Layer Deposition.* Small, 5(6):750–7, March 2009.

[73] D. Teschner, A. Pestryakov, E. Kleimenov, M. Havecker, H. Bluhm, H. Sauer, A. Knopgericke, and R. Schlogl. *High-Pressure X-Ray Photoelectron Spectroscopy of Palladium Model Hydrogenation catalysts.Part 1: Effect of Gas Ambient and Temperature*. Journal of Catalysis, 230(1):186–194, February 2005.

[74] T. Shido and R. Prins. *Application of Synchrotron Radiation to in Situ Characterization of Catalysts*. Current Opinion in Solid State and Materials Science, pages 330–335, 1998.

[75] X. Wang, J. a. Rodriguez, J. C. Hanson, M. Pérez, and J. Evans. *In Situ Time-Resolved Characterization of Au-CeO_2 and AuO_x-CeO_2 Catalysts During the Water-Gas Shift Reaction: Presence of Au and O Vacancies in the Active Phase.* The Journal of chemical physics, 123(22):221101, December 2005.

[76] G. Sankar and J. M. Thomas. *In Situ Combined X-Ray Absorption Spectroscopic and X-Ray Diffractometric Studies of Solid Catalysts*. Topics in Catalysis, 8:1–21, 1999.

5

Paper II: In situ synchrotron based x-ray fluorescence and scattering measurements during atomic layer deposition: initial growth of HfO_2 on Si and Ge substrates.*

5.1 Abstract

The initial growth of HfO_2 was studied by means of synchrotron based in situ x-ray fluorescence (XRF) and grazing incidence small angle x-ray scattering (GISAXS). HfO_2 was deposited by atomic layer deposition (ALD) using TEMAH and H_2O on both oxidized and H-terminated Si and Ge surfaces. XRF quantifies the amount of deposited material during each ALD cycle and shows an inhibition period on H-terminated substrates. No inhibition period is observed on oxidized substrates. The evolution of film roughness was monitored using GISAXS. A correlation is found between the inhibition period and the onset of surface roughness.

*Published as: Devloo-Casier, K., Dendooven, J., Ludwig, K. F., Lekens, G., D'Haen, J., & Detavernier, C. In situ synchrotron based x-ray fluorescence and scattering measurements during atomic layer deposition: Initial growth of HfO_2 on Si and Ge substrates. Applied Physics Letters, 98(23), 231905. (2011)
http://doi.org/10.1063/1.3598433

5.2 Introduction

Atomic layer deposition (ALD) is a thin film growth technique which enables thickness control at the atomic level and conformal deposition on high aspect ratio structures. [1, 2] These features make the technique ideally suited for microelectronics applications, mainly for the deposition of high-κ gate dielectrics. ALD processes are characterized by a layer-by-layer type growth, i.e. the thickness increases proportionally to the amount of ALD cycles. This linear regime is, however, only reached after a couple of ALD cycles. During the first cycles, the film growth is determined by chemisorption of precursor molecules on the substrate and, therefore, pretreatment of the substrate surface is critical. It is important to obtain an in depth understanding of the initial nucleation phase as it has a large influence on the characteristics of the deposited film. For high-κ dielectrics one looks for a fast nucleation with a subsequent linear growth, because this results in a closed layer after a few ALD cycles, enabling the deposition of gate structures with a low equivalent oxide thickness (EOT) [3].

5.3 Results and Discussion

In this study, we propose the use of synchrotron radiation to study the initial growth phase of ALD processes in real time. Probing the sample with x-rays enables to perform x-ray fluorescence (XRF) and grazing incidence small angle x-ray scattering (GISAXS) measurements. XRF allows to monitor the atomic composition of the film and thus the amount of material deposited during each ALD cycle [4–6]. GISAXS is sensitive to both the surface morphology and the internal structure of thin films and is used to monitor the developing surface roughness [7]. The depositions and measurements were performed in the UHV film growth facility, adapted for thermal ALD, installed at beamline X21 of the National Synchrotron Light Source (NSLS) at Brookhaven National Laboratory (BNL).

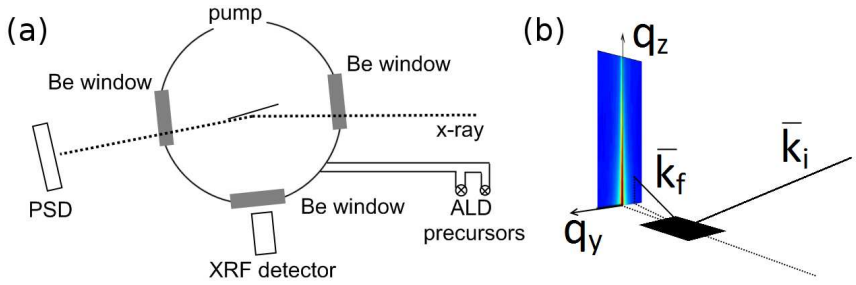

Figure 5.1: (a) Schematic top view representation of the UHV setup, adapted for ALD. X-rays hit the sample at a variable incidence angle. Scattered x-rays are observed with a position sensitive detector (PSD) and fluorescent x-rays are observed by a silicon drift detector. (b) Schematics of the GISAXS geometry. Incident x-rays have a wavevector $\boldsymbol{k}_i$. Due to scattering the wavevector changes to $\boldsymbol{k}_f$. The momentum transfer due to scattering is denoted as $\boldsymbol{q}$.

The initial growth of HfO_2 on two Si based substrates (H-terminated Si and RCA cleaned Si) and two Ge based substrates (H-terminated Ge and PECVD grown GeO_2) was investigated. Tetrakis(ethylmethylamino)hafnium (TEMAH) and deionized water were used as Hf and O source, respectively. For Si-based devices, the main focus has been on $HfCl_4$ as Hf source, but promising results have been reported on the use of TEMAH for the growth of HfO_2 on Ge [8–12]. Because of the low vapor pressure of the TEMAH precursor, Ar was used as carrier gas. All experiments were carried out at a substrate temperature of 200 °C. An ALD cycle consisted of 8 s TEMAH (and Ar) exposure at 1.5 10^{-3} mbar, 20 s pumping, 8 s water exposure at 10^{-3} mbar and again 20 s pumping. The lengths of the precursor steps were chosen so to ensure saturation.

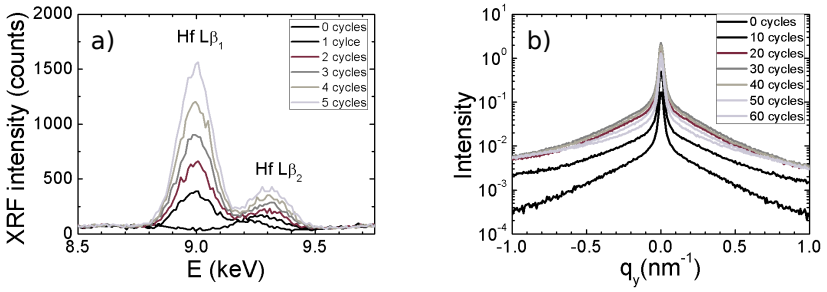

Figure 5.2: (a) Evolution of the Hf $L_{\beta 1}$ (9.0 keV) and Hf $L_{\beta 2}$ (9.3 keV) intensity as measured during the first ALD cycles on RCA cleaned Si. The Hf XRF intensity is proportional to the number of Hf atoms deposited. (b) Evolution of the GISAXS signal as measured every 10 ALD cycles on RCA cleaned Si.

The use of synchrotron-based x-rays allows for tuning of the x-ray energy. The incident x-ray energy was chosen to minimize the fluorescence from the substrate and maximize the fluorescence from Hf excitation. For all Si and Ge based experiments 10.8 keV and 10 keV x-rays were used, respectively. For the in situ XRF measurements, an incident angle of 5.25° was used and a silicon drift detector was positioned perpendicular to the sample, behind a Be window. XRF data were collected during the last pumping step of each ALD cycle. A XRF measurement took 20 s (figure 5.2a). For the in situ GISAXS measurements, an incident angle near the angle of total external reflection of the substrate was used and a one-dimensional position sensitive detector was mounted at an exit angle of 1°, perpendicular to the plane of incidence. GISAXS measurements were performed every 10 cycles. The GISAXS data were collected by integrating the detector signal during a 60 s interval (figure 5.2b).

The results of the XRF measurements are displayed in figure 5.3. In this figure the integrated intensity of the Hf $L_{\beta 1}$ emission line is plotted, as measured every ALD cycle (figure 5.2a). Because the penetration depth of the incident x-rays is of the order of 500 nm, i.e. much larger than the thicknesses of the grown films, the XRF intensity can be used as a direct measure of the amount of deposited Hf atoms. This in turn enables the straightforward determination of the amount of HfO_2 deposited during every single ALD cycle.

Note that in situ spectroscopic ellipsometry (SE) is often used for monitoring film growth during ALD [13]. The main advantage of the in situ XRF technique over the SE method is, especially during the very first ALD cycles, that XRF is not based on model fitting but allows for a direct characterization of the deposited (sub)monolayers, increasing the reliability of the results.

During the very first ALD cycles, hardly any growth retardation and a near-perfect linear growth is observed in the case of RCA cleaned Si and PECVD grown GeO_2 (figures 5.3 b and d). This can be explained by the fact that the starting surfaces are at least partially OH-terminated. The hydroxyl groups have no trouble reacting with the TEMAH precursor, resulting in immediate growth without nucleation effects. Through post-deposition x-ray reflectivity (XRR) measurements the final thickness could be determined, yielding a growth per cycle (GPC) of 1.2 Å per cycle on the Si substrate and 1.6 Å per cycle on the Ge substrate. It is expected that the absence of a nucleation step results in relatively smooth layers, due to nice layer-by-layer growth. This was confirmed by ex situ AFM measurements (see table 5.1).

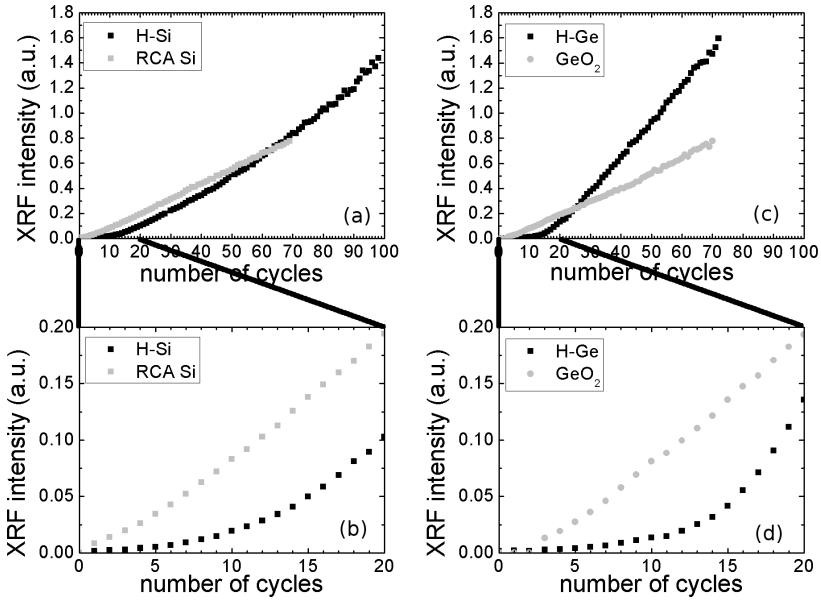

Figure 5.3: Integrated Hf $L_{\beta 1}$ fluorescence intensity measured during ALD on H-terminated Si and RCA cleaned Si (figure a and b) and on H-terminated Ge and GeO_2 (figure c and d) Figure (b) and (d) are a detail of (a) and (c) respectively, focusing on the first 20 cycles.

The growth of HfO_2 on the H-terminated Si and Ge does not follow these characteristics. The XRF measurements clearly show that the amount of HfO_2 deposited on the H-terminated Si and H-terminated Ge only starts increasing after 10 and 15 ALD cycles, respectively. This behavior corresponds to substrate-inhibited island growth as described by the model developed by Puurunen et al. [14] In this model, one assumes that ALD growth only starts at certain defects. These defects then form small islands, which after sufficient amount of ALD cycles coalesce and form a continuous layer. From the XRF measurement, we also learn that the GPC on the H-terminated surfaces is much larger compared to the GPC on the oxidized surfaces. This can be explained by an increased roughness of the surface due to the island growth. A rough surface has a large surface area, leading to a higher GPC. The roughness of the HfO_2 films after 100 and 70 ALD cycles on H-Si and H-Ge, respectively, was measured with ex situ AFM (see tabel 5.1). The AFM results are in agreement with previous ex situ studies of the nucleation of the TEMAH/H_2O process on Si based substrates under similar conditions [15].

substrate	H-Si	RCA Si	H-Ge	GeO_2
σ_{rms} (nm)	**0.717**	0.337	**1.020**	0.398

Table 5.1: Root-mean-square roughness resulting from post-depostion AFM-measurements.

The evolution of the surface roughness during growth was studied by in situ GISAXS (see figure 5.2 b). In the low q_z limit, the integral of the GISAXS intensity can be used as a measure for the square of the rms roughness. [7]

$$\sigma_{rms}^2 \propto \int q_y I(q_y) dq_y \tag{5.1}$$

This enables a qualitative view on the roughness evolution during ALD deposition. The square root of this integral is displayed in figure 5.4 for the four samples at a 10 cycle interval. In order to focus on the increase of roughness, the initial integral at 0 cycles is subtracted from every value.

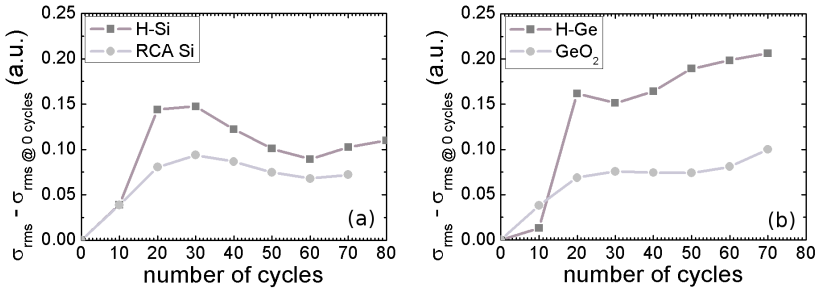

Figure 5.4: Roughness evolution based on the integrated GISAXS pattern for ALD on (a) H-terminated Si and RCA cleaned Si and on (b) H-terminated Ge and GeO_2.

From this data several conclusions can be made. One immediately notices the higher roughness for the HfO_2 films grown on the H-terminated substrates compared to the oxidized substrates, confirming the AFM data. Furthermore, one observes that the film roughness only increases significantly during the initial growth phase. This again stresses the importance of the first ALD cycles. For the H-terminated substrates, one may also note that the roughness only starts increasing after about 10 to 20 cycles, confirming the idea that during the nucleation period, as seen with XRF, no significant amount of material is deposited. The similarities observed in the growth on the RCA cleaned Si and PECVD grown GeO_2 surfaces translates to a similar roughness evolution. Furthermore, for the Si substrates, the integral seems to have a minimum around 50 ALD cycles. This effect is caused by a variation of the peak height at q_y=0. Because this peak has a non zero width, the

variation effect isn't totally eliminated by the weighing by q_y in the integral. For the Ge substrates, this effect is less pronounced.

5.4 Conclusion

In conclusion, we have studied the initial ALD growth of HfO_2 on both oxidized and H-terminated Si and Ge surfaces by in situ XRF and GISAXS. These techniques enabled detailed characterization of the evolution of the amount of deposited material and surface roughness during growth. The ALD of HfO_2 on the oxidized surfaces showed no inhibition period and a layer-by-layer type growth. The HfO_2 growth on H-terminated Si and Ge showed an inhibition period of 10 and 15 ALD-cycles, respectively. In situ GISAXS indicated a larger surface roughness for the HfO_2 films deposited on the H-terminated surfaces compared to the oxidized surfaces.

5.5 Acknowledgements

The research leading to these results has received funding from the European Research Council under the European Union's Seventh Framework Programme (FP7/2007-2013) / ERC grant agreement n 239865. JD acknowledges the FWO - Vlaanderen for a scholarship. Use of the National Synchrotron Light Source, Brookhaven National Laboratory, was supported by the U.S. Department of Energy, Office of Science, Office of Basic Energy Sciences, under Contract No. DE-AC02-98CH10886.

References

[1] S. M. George. *Atomic Layer Deposition: An Overview.* Chemical reviews, 110(1):111–31, jan 2010.

[2] R. L. Puurunen. *Surface Chemistry of Atomic Layer Deposition: A Case Study for the Trimethylaluminum/Water Process*. Journal of Applied Physics, 97(12):121301, 2005.

[3] J. Robertson. *High Dielectric Constant Oxides*. The European Physical Journal Applied, 291:265–291, 2004.

[4] J. Dendooven, S. Pulinthanathu Sree, K. De Keyser, D. Deduytsche, J. a. Martens, K. F. Ludwig, and C. Detavernier. *In Situ X-Ray Fluorescence Measurements During Atomic Layer Deposition: Nucleation and Growth of TiO2 on Planar Substrates and in Nanoporous Films*. The Journal of Physical Chemistry C, 115(14):6605–6610, apr 2011.

[5] J. Dendooven, D. Deduytsche, S. P. Sree, T. I. Kornyi, G. Vanbutsele, J. A. Martens, K. F. Ludwig, and C. Detavernier. *In Situ X-Ray Fluorescence Measurements During ALD on Flat Substrates and in Nanoporous Catalyst Support Materials. Presented at the AVS Topical Conference on ALD, Seoul, South Korea*. AVS Topical Conference on ALD, 20–23 June 2010.

[6] D. D. Fong, J. a. Eastman, S. K. Kim, T. T. Fister, M. J. Highland, P. M. Baldo, and P. H. Fuoss. *In Situ Synchrotron X-Ray Characterization of ZnO Atomic Layer Deposition*. Applied Physics Letters, 97(19):191904, 2010.

[7] G. Ozaydin, K. F. Ludwig, H. Zhou, L. Zhou, and R. L. Headrick. *Transition Behavior of Surface Morphology Evolution of Si(100) During Low-Energy Normal-Incidence Ar^+ Ion Bombardment*. Journal of Applied Physics, 103(3):33512, 2008.

[8] Q. Xie, D. Deduytsche, M. Schaekers, M. Caymax, A. Delabie, X.-P. Qu, and C. Detavernier. *Implementing TiO2 as Gate Dielectric for Ge-Channel Complementary Metal-Oxide-Semiconductor Devices by Using HfO2/GeO2 Interlayer*. Applied Physics Letters, 97(11):112905, 2010.

[9] Q. Xie, D. Deduytsche, M. Schaekers, M. Caymax, A. Delabie, X.-P. Qu, and C. Detavernier. *Implementing TiO2 as Gate Dielectric for Ge-Channel Complementary Metal-Oxide-Semiconductor Devices by Using HfO2/GeO2 Interlayer*. Applied Physics Letters, 97(11):112905, 2010.

[10] Q. Xie, D. Deduytsche, M. Schaekers, M. Caymax, and A. Delabie. *Effective Electrical Passivation of Ge (100) for HfO2 Gate Dielectric Layers Using O2 Plasma*. Electrochemical and Solid-State Letters, 14(May):G20–22, 2011.

[11] Q. Xie, J. Musschoot, M. Schaekers, M. Caymax, A. Delabie, D. Lin, X.-p. Qu, Y.-l. Jiang, and S. V. D. Berghe. *TiO2 / HfO2 Bi-Layer Gate Stacks Grown by Atomic Layer Deposition for Germanium-Based Metal-Oxide-Semiconductor Devices Using GeOxNy Passivation Layer*. Electrochemical and Solid-State Letters, 14(May):G27–31, 2011.

[12] D. W. McNeill, S. Bhattacharya, H. Wadsworth, F. H. Ruddell, S. J. N. Mitchell, B. M. Armstrong, and H. S. Gamble. *Atomic Layer Deposition of Hafnium Oxide Dielectrics on Silicon and Germanium Substrates*. Journal of Materials Science: Materials in Electronics, 19(2):119–123, jul 2008.

[13] E. Langereis, S. B. S. Heil, H. C. M. Knoops, W. Keuning, M. C. M. van de Sanden, W. M. M. Kessels, T. Review, E. Langereis, S. B. S. Heil, H. C. M. Knoops, W. Keuning, M. C. M. van de Sanden, and W. M. M. Kessels. *In Situ Spectroscopic Ellipsometry as a Versatile Tool for Studying Atomic Layer Deposition*. Journal of Physics D: Applied Physics, 42(7):073001, apr 2009.

[14] R. L. Puurunen, W. Vandervorst, W. F. a. Besling, O. Richard, H. Bender, T. Conard, C. Zhao, A. Delabie, M. Caymax, S. De Gendt, M. Heyns, M. M. Viitanen, M. De Ridder, H. H. Brongersma, Y. Tamminga, T. Dao, T. De Win, M. Verheijen, M. Kaiser, and M. Tuominen. *Island Growth in the Atomic Layer Deposition of Zirconium Oxide and Aluminum Oxide on Hydrogen-Terminated Silicon: Growth Mode Modeling and Transmission Electron Microscopy*. Journal of Applied Physics, 96(9):4878, 2004.

[15] J. C. Hackley, T. Gougousi, and J. D. Demaree. *Nucleation of HfO2 Atomic Layer Deposition Films on Chemical Oxide and H-Terminated Si*. Journal of Applied Physics, 102(3):034101, 2007.

Part II

ALD Encapsulation of Quantum Dots

6 Quantum Dots

6.1 Introduction to Quantum Dots

A quantum dot or nanocrystal is a crystalline material with dimensions in the nanometer range. Due to its dimensions, free carriers experience quantum confinement. A quantum dot typically contains a few hundreds to a few thousands of atoms. Therefore, the electronic and optical properties of these quantum dots(QDs) are mainly dictated by their shape and size and are in-between the bulk properties and the properties of single atoms of the material. [1] These extra degrees of freedom allow for an interesting range of unique properties, like localized plasmon effects in Ag and Au nanoparticles, superparamagnetism in magnetic nanocrystals and, most relevant to this work, a size dependent optical bandgap for emission and absorption in semiconductor nanocrystals (see Fig 6.1).

6.1.1 Discovery and Emerging Applications of Quantum Dots

Quantum dots are a relative young concept. It was only 30 years ago, in 1981, that the first quantum dots were discovered in a glass matrix by Alexey Ekimov [3] and later, in 1984, Louis E. Brus discovered them in a colloidal solution. [4] It was, however, only in 1988 that the term 'quantum dot' was first used by Mark Reed.

Currently quantum dots find applications within the field of biology (e.g. as fluorescent marker in bio-imaging [5]), quantum optics [6] and optoelectronics [7]. Gradually the technology is maturing and moving towards consumer applications. This resulted, for example, in the release by Sony of a flat panel display in 2013

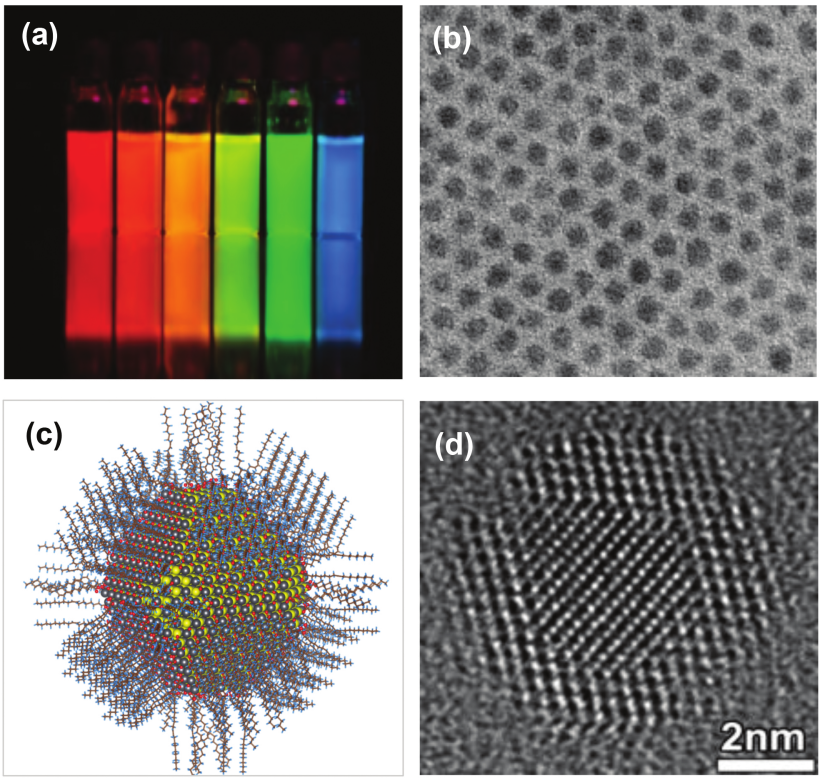

Figure 6.1: Overview of QD properties: (a) Size series of CdTe QDs under UV excitation, (b) TEM image of QDs showing size monodispersity, (c) depiction of individual QD with inorganic core and organic ligand shell and (d) HR-TEM image of a core/shell PbTe/CdTe particle showing the stacking of individual atoms building up the QD. Figure courtesy of Pieter Geiregat. [2]

that uses quantum dots to obtain higher color purity and energy efficiency, as compared to the available OLED technology. The main remaining challenge for quantum dot technology is to make cadmium and lead free quantum dots. Cadmium is banned under the EU Directive on the restriction of hazardous substances (RoHS) in electrical and electronic equipment, but there is however an exemption for its use in illumination and display lighting applications. This exemption is however currently limited until 2017. Therefore, a lot of research has focused on making cadmium free quantum dots for application in optoelectronics.

6.1.2 Colloidal Quantum Dots

In this work, the focus will be on colloidal quantum dots. The surface of colloidal quantum dots is usually passivated by long organic molecules, like fatty acids. This allows the quantum dots to remain in a stable colloidal suspension. Colloidal quantum dots are made using a wet chemical synthesis. As the quantum dots are made in solution, easy deposition methods, like spincoating and dropcasting, are available. This approach is more scalable and cost-effective than for example epitaxially grown quantum dots.

6.1.2.1 Wet Chemical Synthesis

Colloidal quantum dots are traditionally synthesized by thermal decomposition of organometallic precursors in hot reaction medium. Hot injection (HI) is currently the most widely used method. The method was developed in 1993 by C.B. Murray, D.J. Norris and M.G. Bawendi. [8] In this case anionic precursors are rapidly injected into solution, containing cationic precursors at elevated temperature (50 °C-360 °C) (see Fig. 6.2(a),left). By ensuring a fast supersaturation of reactant during injection, the quantum dots nucleate in a short period of time. This results in monodispersed quantum dots, during and after growth (see Fig. 6.2(a), right). This in turn results in a well defined absorption spectrum of the quantum dots (see Fig. 6.2(c)). [9]

6.1.2.2 Monolayer Deposition Through Langmuir-Blodgett

In most practical applications, the quantum dots need to be transfered to a support. By using a wet chemical synthesis, the quantum dots are formed as a colloidal dispersion. These solutions can be used to make quantum dot layers, using e.g. spincoating, dropcasting, doctor blading and inkjet printing. These techniques are well adapted to quickly cover large areas with a uniform film, but the morphology is difficult to control. If a more defined morphology, like eg. a perfect hexagonally packed monolayer is required, other techniques need to be used.

Langmuir-Blodgett (LB) deposition (and Langmuir-Schaeffer deposition) offer an extra degree of control, enabling the deposition of well defined monolayers of quantum dots. [10] LB is based on the hydrophobic nature of the ligand shell of the quantum dots. If a drop of the colloidal quantum dot dispersion is placed on a water surface, the volatile solvent will evaporate and the hydrophobic quantum dots will float on the surface. The quantum dots will rearrange themselves on the surface to form islands of closed packed (hexagonally or cubic) quantum dots. These islands can be compressed into a single monolayer. By pulling a substrate through the layer, the monolayer can be transferred. During this transfer the surface pressure (or isotherm) is monitored, to ensure that no gaps are formed during the transfer.

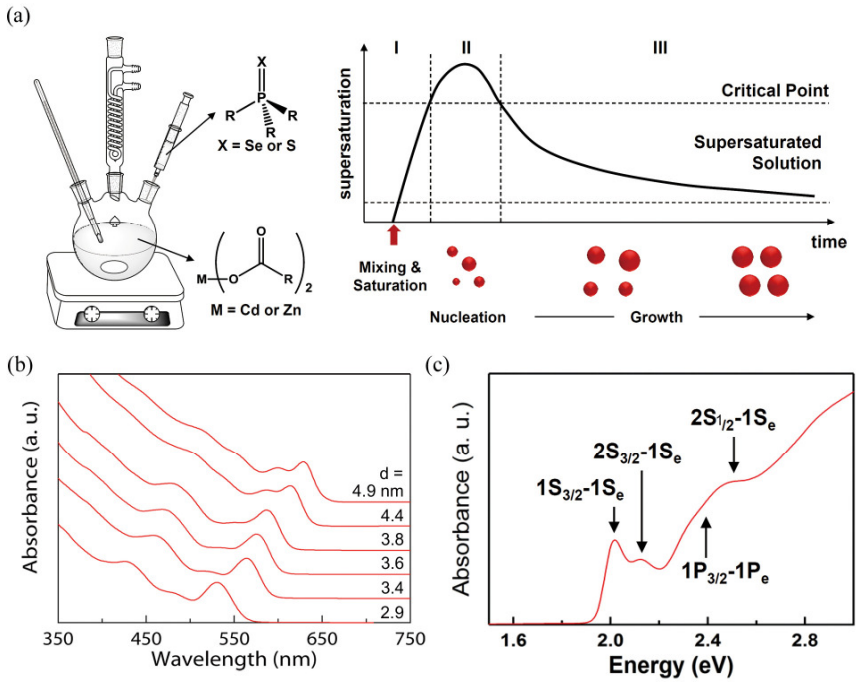

Figure 6.2: Hot injection synthesis of XY (X=Cd or Zn, Y=S or Se) colloidal quantum dots. (a) A conventional hot-injection method for group II-VI QDs and corresponding temporal change in degree of supersaturation (The LaMer plot). (b) Example of absorption spectra for monodisperse CdSe QDs and (c) the involved excitonic states. Figure courtesy of Jaehoon Lim. [9]

6.1.3 Photoluminescence of Quantum Dots

In the following chapters, we will use the photoluminescent properties of the used quantum dots to judge the effect of the encapsulation method on the change in opto-electronic properties of the monolayer of quantum dots.

Under illumination of a quantum dot, an electron-hole pair can be created by absorption of a high energy photon. This electron-hole pair will cool to the band edges and form and exciton. An exciton is a quasi-particle, formed as a bound state between an electron and a hole by coulomb attraction. The exciton will dissipate energy, either radiatively or non-radiatively. The main non-radiative mechanism is carrier trapping. Here, the electron and hole are trapped at defect states. These defect states can be located in the bulk, e.g. lattice defects, or at the surface, e.g. unpassivated surface atoms. Since quantum dots have a large surface to volume ratio, these surface defects are usually the main trap states. To improve the emission of the quantum dots, the number of non-radiative recombination paths need

to be decreased. This is typically done by increasing the crystallinity of the quantum dots and passivation of the surface. In the following chapters, changes in the PL will be attributed to the change in surface states during the ALD encapsulation process, as the encapsultation process will only affect the surface of the quantum dots.

6.2 Combining ALD and Quantum Dots

This section provides a short overview of existing literature on the ALD technique applied in relation to quantum dots. ALD has been utilized with the following goals in mind:

- Direct growth of QDs
- Encapsulation of QDs to obtain a protective barrier
- Enhancing the properties of the QDs

6.2.1 Direct Growth of QDs

Atomic layer deposition is particularly suited to grow continuous, homogeneous and smooth films. However, under the right conditions and by exploiting the nucleation behavior of some ALD processes, nanocrystals and particles can be obtained. This is especially interesting for microelectronics, where the growth of quantum dots by ALD can be easily incorporated in the process flow. For other applications, this might not be the optimal solution, and other growth and deposition methods are better suited, as they are easier to control and provide a wider range of possible materials.

Currently, QD growth by ALD is mainly explored for memory applications. Semiconductor and metallic nanocrystals show promising storage qualities. Metallic particles are considered to be the best choice, as they offer lower power consumption, better size scalability and improved endurance. At the moment, ruthenium is considered as a good option, due to its high thermal and chemical stability. (see figure 6.3) The nucleation behavior of the known Ru ALD process allows the growth of the needed particles. [11, 12]

Attempts have also been made to grow semiconductor nanocrystals for PV applications. Recently, the growth of CdS and PbS quantum dots by ALD, for the use in a solid-state quantum dot-sensitized solar cell, has been shown. (see figure 6.4) [13, 14]

ALD has also influenced the growth of QDs in a more conceptual way. Based on the core idea of self-limiting half reactions, the concept of colloidal ALD (c-ALD) was born. During the c-ALD process, either nanoparticles or molecular

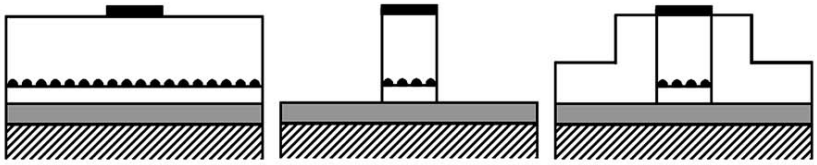

Figure 6.3: Configurations of memory cells with a continuous Ru nanocrystal array deposited by ALD. Figure courtesy of Damon B. Farmer. [11]

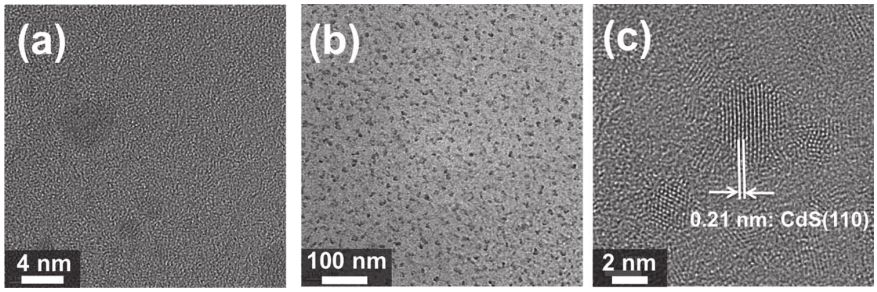

Figure 6.4: TEM images of CdS particles deposited by ALD. (a) 5 ALD cycles and (b)(c) 10 ALD cycles on a TiO_2 surface. Figure courtesy of Thomas P. Brennan. [13]

precursors are sequentially transferred between polar and nonpolar solutions. This allows a layer-by-layer growth, similar to gas phase ALD. [15]

The use of ALD to directly grow QDs is definitely being explored and has shown promising results in certain specific cases. The spatial distribution and size of ALD grown QDs is however tightly linked and thus hard to control separately. Therefor, for most applications, the wet chemical synthesis (see section 6.1.2.1) is still preferred as this allows a decoupling of the particle formation and the transfer to the support. Moreover, it has been shown that QDs in solution can be ink-jet printed, making the process more scalable to the industrial level, than the ALD based method.

6.2.2 Encapsulation of QDs to Obtain a Protective Barrier

The, by far, most important application of ALD can be found in the encapsulation of QDs. In most cases, QDs need to be protected from air and moisture to retain their properties and reduce aging effects.

Due to the wide range of applications of QDs, the encapsulation of QDs by ALD can be found in numerous applications. In non-volatile memory research, the nanocrystal memory cell is being investigated. Here, the silicon nanocrystals are being encapsulated by a 10 nm layer of Al_2O_3, to prevent oxidation. To prevent

oxygen and water diffusion, an additional 8 nm thick TiN layer is deposited on top. [16]

In PbS colloidal QD based photoconductors, an Al_2O_3 layer is used to provide air-stable operation and passivation. [17] Others have shown that the oxidation, ripening and sintering of PbS quatum dot films has been greatly suppressed by infilling the films with Al_2O_3. [18] It has also been demonstrated that the infilling of conductive PbSe nanocrystals by metal oxides, can form a nanocomposite. Locking the nanocrystals in place and protecting them against oxidation and photothermal damage, allowing the fabrication of robust nanocrystal solids for optoelectronic devices (see figure 6.5). [19]

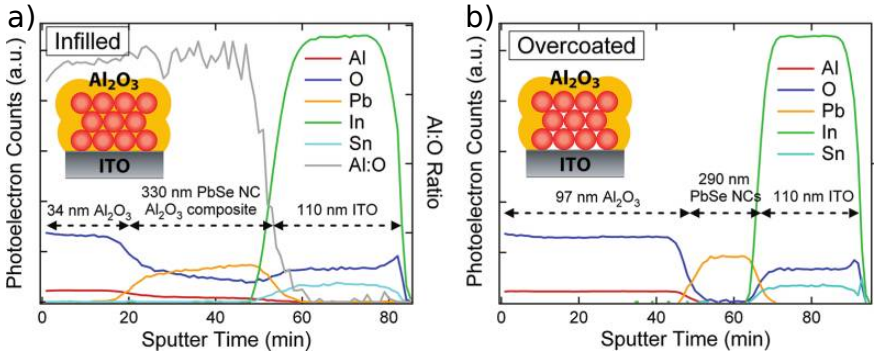

Figure 6.5: (a) Infilling a QD film with Al_2O_3 using ALD. XPS shows the deposited material penetrates the complete film. (b) Overcoating a QD film with Al_2O_3 using CVD. XPS shows that deposition is limited to the outside of the QD film. Figure courtesy of Yao Liu. [19]

The encapsulation of CdSe/ZnS coreshell nanocrystals into thin films of ZnO by thermal ALD and Al_2O_3 grown by both thermal and plasma-enhanced ALD has been studied to fabricate optoelectronic nanodevices using luminescent colloidal nanoparticles. [20, 21]

6.2.3 Enhancing the Properties of the QDs

Using ALD layers in combination with QDs, is in most cases a protective measure. In some cases, the ALD layer can improve the quality of the QDs, by for example passivation, or improve the working of the QD based device, as a whole.

For example, the use of a ultrathin TiO_2 layer by ALD on ZnO aggregates in a dye-sensitized solar cell, provides a higher power conversion efficiency, by protecting the nanocrystals from exposure to the dye electrolyte. [22]

In solid-state quantum dot-sensitized solar cell, the deposition of an Al_2O_3 barrier layer before PbS QD deposition, improves the device efficiency. The deposition of Al_2O_3 after the QD deposition, doesn't influence the working of the

device. This shows the importance of the ALD layer, not merely as a protective layer, but as an essential part of the QD device. [14]

In high-current-density CdSe/ZnS QD LEDs, the infilling of a film of quantum dots with an insulating oxide, has been shown to funnel the current through the QDs, increasing light emission yield (see figure 6.6). [23]

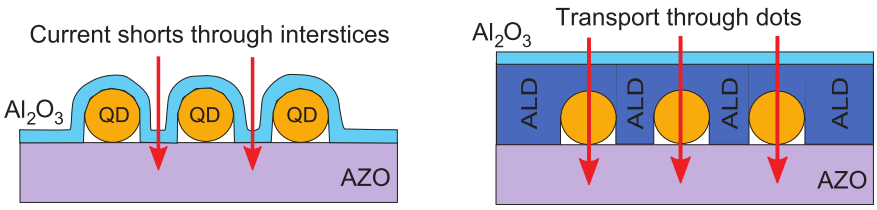

Figure 6.6: In the left device, current flows preferentially through the device interstices, preventing radiative recombination. Fabrication of the device on the right begins with an ALD treatment, which fills the interstices before overcoating the QDs. This treatment forces current to pass through the QDs, resulting in radiative recombination. Figure courtesy of Edward M. Likovich. [23]

6.3 This Work

In this work, we use *in situ* synchrotron based techniques, mainly XRF and GISAXS, to gain additional insight in the ALD encapsulation of QDs and the accompanying interaction between the ALD precursors and the surface of the QDs. Here, we study the ALD encapsulation of monolayers of CdSe/CdS/ZnS QDs. These core/shell/shell QDs are highly luminescent and provide an easy way to check the effect of the encapsulation process on the functionality of the QDs by measuring the photoluminescence response. The use of well defined monolayers of QDs instead of multilayer stacks of QDs allows us to focus of the interaction between the QDs and the ALD process, by avoiding the possibility of only partial infilling of the QD-layer or differences between the interaction at the top of the QD stack and the QDs at the bottom. In the following chapters we will study the encapsulation by respectively ZnO, Al_2O_3 and TiO_2. An overview can be seen in table 6.1. These materials can be grown with well-known ALD processes and have useful application in the design of QD-based devices.

In chapter 7 the encapsulation of CdSe/CdS/ZnS core/shell/shell QDs in a ZnO matrix is studied in detail. *in situ* XRF and GISAXS are used to gain insight in the interaction between the QDs and the ALD precursors and the resulting metal oxide coating. The use of these *in situ* techniques allows us to show the inhibition of ZnO growth on as-deposited QDs. The growth can however be triggered by exposing the QDs to a single pulse of TMA. The sensitivity of the *in situ* XRF enables

ALD process \ Pretreatment	None	TMA	$TDMAT/TiO_2$
ZnO	Chapter 7		
Al_2O_3	Chapter 8		Chapter 8
TiO_2	Chapter 8		

Table 6.1: Overview of the used ALD processes and corresponding pretreatments for the encapsulation of CdSe/CdS/ZnS core/shell/shell QDs.

us to identify an Al-for-Zn substitution-reaction at the QD surface, involving the substitution of approximately one third of the original Zn by Al. This in turn causes a reduction of the photoluminescence quantum yield. *In situ* GISAXS is used to study the ordering of the QDs and monitor changes during the encapsulation process. These measurements uncover an important interplay between the highly reactive ALD precursors and the QD surface.

In the subsequent chapter, chapter 8, the encapsulation of the same QDs is attempted by ALD of Al_2O_3 and TiO_2. Here a distinctive difference can be found in the photoluminescence response after encapsulation. We employ *in situ* XRF and GISAXS to study the difference in nucleation behavior and surface interaction during the start of the encapsulation process. This again points to an important difference in precursor chemistry. Here we show that the widely used ALD process for Al_2O_3 growth is not always the optimal choice, even-tough Al_2O_3 encapsulation is often seen as a 'universal' solution within the ALD community.

References

[1] D. V. Talapin, J. S. Lee, M. V. Kovalenko, and E. V. Shevchenko. *Prospects of Colloidal Nanocrystals for Electronic and Optoelectronic Applications*. Chemical Reviews, 110(1):389–458, 2010.

[2] P. Geiregat. *Colloidal Quantum Dots for Guided Wave Photonics: From Optical Gain to Ultrafast Modulation*. PhD thesis, Ghent University, 2015.

[3] A. Ekimov and A. Onushchenko. *Quantum Size Effect in the Optical-Spectra of Semiconductor Micro-Crystals*. Soviet Physics Semiconductors-USSR, 16(7):775–778, 1982.

[4] L. E. Brus. *Electronelectron and Electron-Hole Interactions in Small Semiconductor Crystallites: The Size Dependence of the Lowest Excited Electronic State*. The Journal of Chemical Physics, 80(1984):4403, 1984.

[5] M. Bruchez Jr. *Semiconductor Nanocrystals as Fluorescent Biological Labels*. Science, 281(5385):2013–2016, sep 1998.

[6] M. Kuno, D. P. Fromm, H. F. Hamann, A. Gallagher, and D. J. Nesbitt. *On/off Fluorescence Intermittency of Single Semiconductor Quantum Dots*. The Journal of Chemical Physics, 115(2):1028, 2001.

[7] V. I. Klimov. *Optical Gain and Stimulated Emission in Nanocrystal Quantum Dots*. Science, 290(5490):314–317, oct 2000.

[8] C. B. Murray, D. J. Norris, and M. G. Bawendi. *Synthesis and Characterization of Nearly Monodisperse CdE (E = Sulfur, Selenium, Tellurium) Semiconductor Nanocrystallites*. Journal of the American Chemical Society, 115(19):8706–8715, sep 1993.

[9] J. Lim, W. K. Bae, J. Kwak, S. Lee, C. Lee, and K. Char. *Perspective on Synthesis, Device Structures, and Printing Processes for Quantum Dot Displays*. Optical Materials Express, 2(5):594, may 2012.

[10] J. R. Heath, C. M. Knobler, and D. V. Leff. *Pressure/Temperature Phase Diagrams and Superlattices of Organically Functionalized Metal Nanocrystal Monolayers: The Influence of Particle Size, Size Distribution, and Surface Passivant*. The Journal of Physical Chemistry B, 101(2):189–197, jan 1997.

[11] D. B. Farmer and R. G. Gordon. *High Density Ru Nanocrystal Deposition for Nonvolatile Memory Applications*. Journal of Applied Physics, 101(12):124503, 2007.

[12] D.-J. Lee, S.-S. Yim, K.-S. Kim, S.-H. Kim, and K.-B. Kim. *Non-volatile Memory Characteristics of Atomic Layer Deposited Ru Nanocrystals With a SiO_2/Al_2O_3 Bilayered Tunnel Barrier*. Journal of Applied Physics, 107(1):013707, 2010.

[13] T. P. Brennan, P. Ardalan, H.-B.-R. Lee, J. R. Bakke, I.-K. Ding, M. D. McGehee, and S. F. Bent. *Atomic Layer Deposition of CdS Quantum Dots for Solid-State Quantum Dot Sensitized Solar Cells*. Advanced Energy Materials, 1(6):1169–1175, nov 2011.

[14] T. P. Brennan, O. Trejo, K. E. Roelofs, J. Xu, F. B. Prinz, and S. F. Bent. *Efficiency Enhancement of Solid-State PbS Quantum Dot-Sensitized Solar Cells With Al2O3 Barrier Layer*. Journal of Materials Chemistry A, 1(26):7566, 2013.

[15] S. Ithurria and D. V. Talapin. *Colloidal Atomic Layer Deposition (C-Ald) Using Self-Limiting Reactions at Nanocrystal Surface Coupled to Phase Transfer Between Polar and Nonpolar Media*. Journal of the American Chemical Society, 134(45):18585–18590, 2012.

[16] I. Brunets, A. Aarnink, A. Boogaard, A. Kovalgin, R. Wolters, J. Holleman, and J. Schmitz. *Low-Temperature LPCVD of Si Nanocrystals From Disilane and Trisilane (Silcore) Embedded in ALD-alumina for Non-Volatile Memory Devices*. Surface and Coatings Technology, 201(22-23):9209–9214, sep 2007.

[17] C. Hu, A. Gassenq, Y. Justo, K. Devloo-Casier, H. Chen, C. Detavernier, Z. Hens, and G. Roelkens. *Air-Stable Short-Wave Infrared PbS Colloidal Quantum Dot Photoconductors Passivated With Al2O3 Atomic Layer Deposition*. Applied Physics Letters, 105(17):171110, oct 2014.

[18] R. Ihly, J. Tolentino, Y. Liu, M. Gibbs, and M. Law. *The Photothermal Stability of PbS Quantum Dot Solids.* ACS nano, 5(10):8175–86, oct 2011.

[19] Y. Liu, M. Gibbs, C. L. Perkins, J. Tolentino, M. H. Zarghami, J. Bustamante, and M. Law. *Robust, Functional Nanocrystal Solids by Infilling With Atomic Layer Deposition*. Nano Letters, 11(12):5349–5355, dec 2011.

[20] S. H. Kim, P. H. Sher, Y. B. Hahn, and J. M. Smith. *Luminescence From Single CdSe Nanocrystals Embedded in ZnO Thin Films Using Atomic Layer Deposition*. Nanotechnology, 19(36):365202, sep 2008.

[21] K. Lambert, J. Dendooven, C. Detavernier, and Z. Hens. *Embedding Quantum Dot Monolayers in Al2O3 Using Atomic Layer Deposition*. Chemistry of Materials, 23(2):126–128, jan 2011.

[22] K. Park, Q. Zhang, B. B. Garcia, X. Zhou, Y.-H. Jeong, and G. Cao. *Effect of an Ultrathin TiO2 Layer Coated on Submicrometer-Sized ZnO Nanocrystallite Aggregates by Atomic Layer Deposition on the Performance of Dye-Sensitized Solar Cells*. Advanced Materials, 22(21):2329–2332, jun 2010.

[23] E. M. Likovich, R. Jaramillo, K. J. Russell, S. Ramanathan, and V. Narayanamurti. *High-Current-Density Monolayer CdSe/ZnS Quantum Dot Light-Emitting Devices With Oxide Electrodes*. Advanced Materials, 23(39):4521–4525, oct 2011.

7

Paper III: A Case Study of ALD Encapsulation of Quantum Dots: Embedding Supported CdSe/CdS/ZnS Quantum Dots in a ZnO Matrix.*

7.1 Abstract

We study the encapsulation of monolayers of CdSe/CdS/ZnS core/shell/shell quantum dots (QDs) in a ZnO matrix by atomic layer deposition (ALD), in order to gain insight in the interaction between quantum dots and ALD precursors and the resulting metal oxide coating. Using *in situ* XRF and GISAXS, we show the inhibition of ZnO growth on as-deposited QDs. Growth can, however, be triggered by exposing the QDs to a single pulse of trimethylaluminium (TMA) vapor. Such a TMA pretreatment results in the substitution of 35-40% of the surface Zn by Al. Whereas this drops by half the photoluminescence quantum yield of the QDs, we argue that this replacement primes the QD monolayer for ZnO growth by ALD. Finally, the evolution of the GISAXS pattern during subsequent ALD growth attests the preservation of the ordering of the QDs in the monolayer. These results illustrate the important interplay between highly reactive ALD precursors and the QD surface.

*Manuscript in preparation - Devloo-Casier K., Geiregat P., Ludwig K. F., van Stiphout K., Vantomme A., Hens Z., Detavernier C., Dendooven J.

7.2 Introduction

Colloidal semiconductor nanocrystals or quantum dots (QDs) are rapidly evolving from a scientific model system of strong quantum-confinement effects to a solution-processable building block for opto-electronic devices, nanoscale or flexible electronic components or solar energy conversion. [1] For example, the combination of a tunable and narrow photoluminescence spectrum and an adjustable absorption spectrum offered by CdSe/CdS core/shell QDs makes for a unique optical down-convertor to be used as remote phosphor or in luminescent solar concentrators. [2, 3] In addition, thin films of densely packed CdSe, PbS or PbSe QDs act as solution-cast semiconductors of use in field-effect transistors, infra-red photodetectors or solar cells. [4, 5] In all these cases, the simple fact that colloidal synthesis yields stable QD dispersions proved a key asset since it enables QDs to be combined with a wide range of material and technology platforms where anything from nanoscale QD deposits to large area QD-based coatings can be formed. A common issue faced, however, by most studies developing QD-based devices appears to be a lack of long-term functionality or performance, which is typically attributed to irreversible changes of the QD surface termination. Various studies have indeed shown that the photoluminescence quantum yield of QDs drops if surface-passivating moieties detach [6] or that the Fermi-energy in QD films shifts upon oxidation of the QD surface. [7] As a result, QD encapsulation has become an active field of research where both organic and inorganic matrices or coatings are used to save QDs for example from direct exposure to ambient conditions.

An appealing approach for QD encapsulation is the formation of an inorganic matrix or coating by atomic layer deposition (ALD). As a self-limiting, conformal growth process, ALD has been widely applied for coating irregular surfaces with high aspect ratio features with nanometer-thick films of typically metal oxides such as Al_2O_3, HfO_2, TiO_2 or ZnO. [8] In recent years, ALD grown Al_2O_3 has therefore been proposed as an encapsulation layer for complete QD-based device stacks [9, 10] that makes for air-stable devices. More interestingly however is the finding that ALD enables Al_2O_3 and ZnO films to be grown directly on QD layers, [11, 12] where it was found that depending on the growth conditions this can result in a mere overcoating or a true impregnation of the QD layer by the metal oxide. [13] These studies showed that ALD growth can protect, *e.g.*, PbS and PbSe QDs from oxidation, ripening and sintering [13–16] and CdSe QDs from deteriorating in air. [12, 17] Moreover, it was found that ALD impregnation can also improve the functionality of QDs and QD-stacks, where impregnation of close-packed PbSe QD flms with ZnO led to enhanced charge carrier mobility and charge carrier multiplication. [13, 18] Given the extensive tunability of the ALD process, such findings indicate that ALD has signficant potential as a technique for post-functionalization of QDs, well beyond encapsulation and oxidation

protection. This, however, requires more detailed insight in the way the ALD precursors and the eventually formed metal oxide coating interact with the QDs and the QD surface.

Here, we investigate the atomic layer deposition of ZnO on CdSe/CdS/ZnS core/shell/shell quantum dots from this perspective. To avoid inconclusive results due to partial infilling, ZnO is grown on QD monolayers made by Langmuir-Blodgett deposition and the variation of film composition and nanocrystal arrangement during the ALD process are monitored *in situ* using x-ray fluorescence (XRF) and grazing incidence small angle x-ray scattering (GISAXS). We find that the ZnO nucleation and growth in successive ALD cycles is inhibited on as-deposited nanocrystals, yet can be triggered by exposing the QDs to a single pulse of trimethylaluminium (TMA) vapor. We find that this comes with a self-limiting substitution of 35-40% of the Zn originally present by Al and a halving of the photoluminescence quantum yield. Since *in situ* IR spectroscopy gives no evidence of chemical modification of the originally present ligands, we propose that the presence of surface Al^{3+} prepares the ground for subsequent ZnO growth. Opposite from the QD surface composition, the evolution of the GISAXS pattern during ALD shows that the QD ordering in the monolayer is not affected by ZnO coating. These results point towards the importance of the interplay between highly reactive ALD precursors and the QD surface, thereby priming the latter for nucleation and growth but also affecting the QD properties.

7.3 Experimental

Quantum Dot Langmuir-Blodgett Layers. In this study, we use CdSe/CdS/ZnS core/shell/shell QDs with oleic acid ligands. These QDs are produced using a successive ion layer adsorption and reaction (SILAR) method. [19, 20] The CdSe core has a diameter of 3 nm. The shell consists of 3 monolayers of CdS and 2 monolayers of ZnS. The QDs are then transferred from the suspension to the silicon substrate through Langmuir-Blodgett deposition. This ensures deposition of a single monolayer of QDs, ordered (locally) in a hexagonal pattern. [21, 22] The layer quality has been analyzed using atomic force microscopy (AFM) and transmission electron microscopy (TEM).

***In Situ* Synchrotron Based X-Ray Fluorescence (XRF) and Grazing Incidence Small Angle X-Ray Scattering (GISAXS).** The encapsulation by ALD of the QDs in the ZnO matrix is studied through synchrotron based X-ray fluorescence (XRF) and grazing incidence small angle scattering (GISAXS) measurements. [23–28] The depositions and measurements were performed in the UHV film growth facility, adapted for thermal ALD, installed at beamline X21 of the National Synchrotron Light Source at Brookhaven National Laboratory. The use of

synchrotron-based x-rays allows for tuning of the x-ray energy. The incident x-ray energy was set to 10 keV, as this allows the excitation of the Kα lines of Zn at approximately 8.6 keV. For the *in situ* XRF measurements, an incident angle of 6.25° was used and a silicon drift detector was positioned perpendicular to the sample, behind a Be window. XRF data was collected during the last pumping step of each ALD cycle. The amount of fluorescent x-rays was integrated over a period of 30 s. The XRF signal has been calibrated to correspond to a number of atoms using Rutherford backscattering spectrometry (RBS) after the *in situ* experiment. For the *in situ* GISAXS measurements, an incident angle of 1 ° was used. The measurements were performed with a Dectris Pilatus 100K area detector, mounted behind a Be exit window at a distance of approximately 80 cm from the sample. The GISAXS data were collected by integrating the detector signal during a 30 s interval.

ZnO ALD Process. For the deposition of ZnO a thermal ALD process was used, using diethyl zinc (DEZ) and water as Zn and O source respectively. All experiments were carried out at a substrate temperature of 200 °C. An ALD cycle consisted of 8 s DEZ exposure at 5 10^{-3} mbar, 20 s pumping, 8 s water exposure at 5 10^{-3} mbar, and again 40 s pumping (the last pumping step also includes the measurement time for the *in situ* measurements). The lengths of the precursor steps were chosen in order to ensure saturation. During some experiments, an exposure to trimethyl aluminium (TMA) has been used to pretreat the surface, by admitting TMA to the chamber at a pressure of 5 10^{-3} mbar in 8 s long pulses.

X-ray Photoelectron Spectroscopy (XPS) Measurements. X-ray photoelectron spectroscopy (XPS) was performed on the final structure to investigate the inclusion of aluminum and carbon within the ZnO layer and at the interface with the QDs. Measurements were performed on a Theta Probe system of Thermo Scientific, operating at a base pressure of 10^{-10} mbar. The system has an Al X-ray excitation source. The surface carbon peak at 284.6 eV was used as a binding energy reference.

***In situ* infrared absorption spectroscopy (FTIR)** *In situ* infrared absorption spectroscopy (FTIR) was performed to study the effect of the pretreatment on the ligand shell. Measurements were performed on a homebuild ALD reactor, optically connected to a Vertex 70v, equipped with an MCT detector. A monolayer of QDs deposited on double side polished silicon was mounted vertically, to allow transmission measurements.

Photoluminescence Spectroscopy. Photoluminescence (PL) spectra were acquired, using a silicon PMT (Edinburgh Instruments), by exciting the samples with a wavelength of 350 nm from a Xenon discharge lamp. This excites the system well below the band gap of ZnO at 500 nm. The ZnO layer is sufficiently thin to avoid any waveguiding effects, that might alter the collection efficiency. The refractive index of ZnO (n≈2 at 550 nm) is larger than that of air (n=1) or ligands (n=1.5), which might induce a change in PL efficiency through a change in the radiative decay rate, but this effect is negligible. To minimize substrate coupling and absorption loss, samples deposited on a glass support were used.

7.4 Results and Discussion

7.4.1 CdSe/CdS/ZnS Quantum Dot Monolayers

To gain a more in-depth knowledge of the interaction between QDs and ALD precursors and the resulting metal oxide coating, we investigate the atomic layer deposition of ZnO on monolayers of CdSe/CdS/ZnS core/shell/shell quantum dots made by Langmuir-Blodgett deposition. The choice for ALD deposition on monolayers instead of on thicker films of stacked QDs avoids inconclusive results due to partial infilling of the film with ALD. As suggested by the cartoon image shown in Figure 7.1a, Langmuir-Blodgett deposition typically leads to a single monolayer of quantum dots that exhibits local hexagonal ordering. [21] This picture is confirmed by the bright field transmission electron microscopy (TEM) image (Figure 7.1b), which shows a monolayer of $\approx 6.0\,\mathrm{nm}$ QDs mostly surrounded by 6 neighboring QDs with an average QD-QD interdistance of $\approx 7.5\,\mathrm{nm}$. This superstructure is also retrieved in the GISAXS pattern, measured *in situ* just before ALD deposition, see Figure 8.1c. It features a central $q_y = 0\,\mathrm{nm}^{-1}$ peak corresponding to near specular reflection together with three side peaks that reflect the structure within the QD monolayer. Labeling the position of the first side peak as q_0, we find that the side peaks correspond to successive q_y reciprocal lattice points of q_0, $\sqrt{3}q_0$ and $2q_0$, respectively. We can thus index these peaks as the $\{10\}$, $\{11\}$ and $\{20\}$ reflections of a two-dimensional hexagonal lattice. [29] The distance between neighboring QDs can then be calculated as $2\pi/q_0$, which yields a QD spacing of $7.7\,\mathrm{nm}$ in agreement with that observed in the TEM image. We thus conclude that the local hexagonal ordering of the QD monolayer as apparent from the TEM image extends over the full area of the sample illuminated with the grazing incidence x-ray beam.

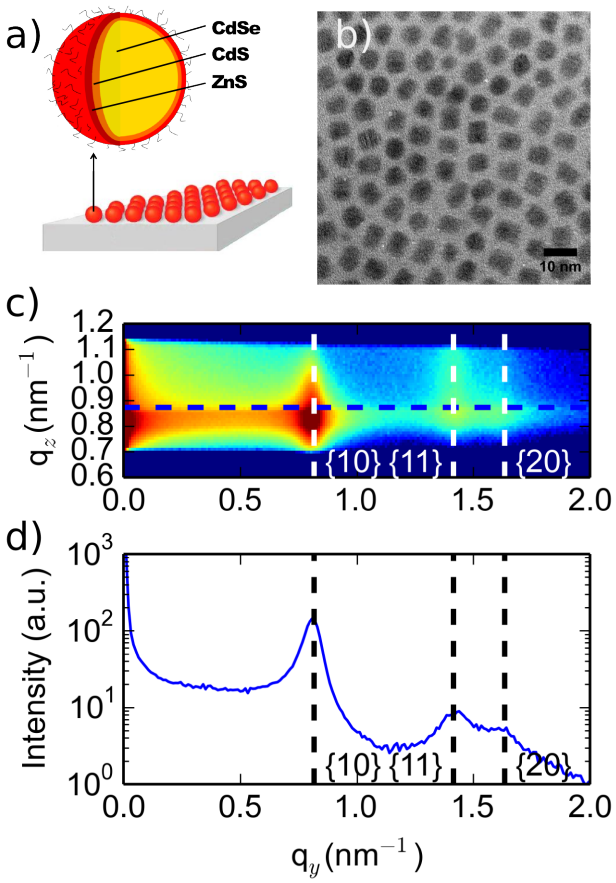

Figure 7.1: The top left (a) is a schematical representation of the monolayer of quantum dots. The top right (b) shows a TEM image of the QDs ordered in a hexagonal closed packed structure. (c) shows the GISAXS image obtained from the monolayer of QDs. The three side peaks result from the structure within the monolayer of quantum dots. These peaks can be indexed to the {10}, {11} and {20} reflections of a two-dimensional hexagonal lattice. The blue dotted line indicates a cross section near the angle of total external reflection, shown in the (d).

7.4.2 Atomic Layer Deposition of ZnO on Quantum Dot Monolayers

As outlined in the Methods section, ZnO is grown by the alternate exposure of the QD monolayer to diethyl zinc and water at 200 °C, where the ALD growth of ZnO on a SiO_2 surface is used as a reference. The possible growth of a ZnO film on the QD layer is monitored *in-situ* by x-ray fluorescence (XRF), where the amount of Zn deposited is derived from the RBS-calibrated Zn Kα fluorescence intensity.

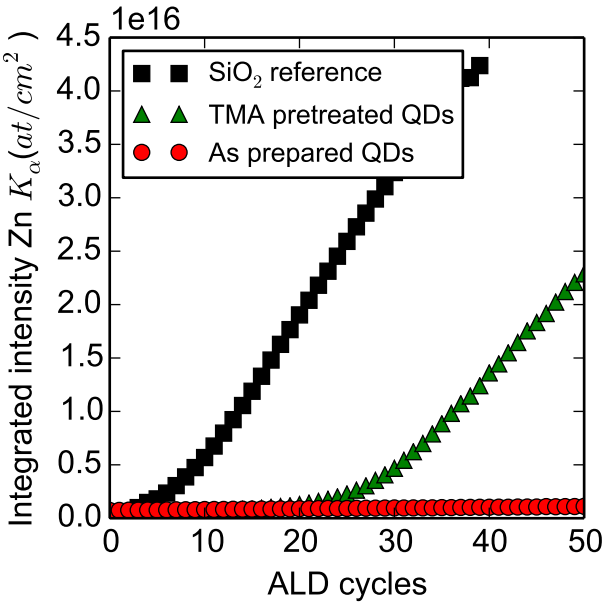

Figure 7.2: The integrated XRF intensity of the Zn Kα line indicating the amount of deposited ZnO during the encapsulation process. The growth on SiO_2 is added as a reference. No growth can be observed on the as prepared monolayer of QDs. After pretreating the layer with TMA, growth occurs after a nucleation period.

As can be seen in Figure 7.2, the ZnO layer thickness on the reference substrate increases linearly with the number of ALD cycles after a few initial nucleation cycles, a finding in line with literature. [30] The concomitant growth per cycle (GPC) as obtained by x-ray reflectivity amounts to 2 Å per cycle. This corresponds to an RBS-calibrated atom density of about $\approx 4.0\,10^{16}\,\mathrm{Zn\,atoms/cm^2}$ after 40 ALD cycles. In the case of the QD monolayer on the other hand, the XRF intensity points towards a Zn surface density of only $\approx 0.6\,10^{15}\,\mathrm{Zn\,atoms/cm^2}$ after 50 cycles. As this figure can be attributed to the Zn in the ZnS shell, we conclude that hardly any ZnO is grown on the QD monolayer during the first 50 cycles of the thermal ALD process used here. Probably, this is due to the organic ligands terminating the QD surface and thereby inhibiting ZnO ALD growth by preventing the ALD precursors to adsorb at the QD surface.

Opposite from the inhibition of ZnO growth observed here, previous studies found that thermal ALD of Al_2O_3 can be used to effectively encapsulate similar monolayers of CdSe/CdS and CdSe/CdS/ZnS QDs with an Al_2O_3 coating. [12] We therefore tried priming the QD monolayer for ALD growth of ZnO by pre-exposing it to tri-methyl aluminum (TMA), which is used as the Al precursor in

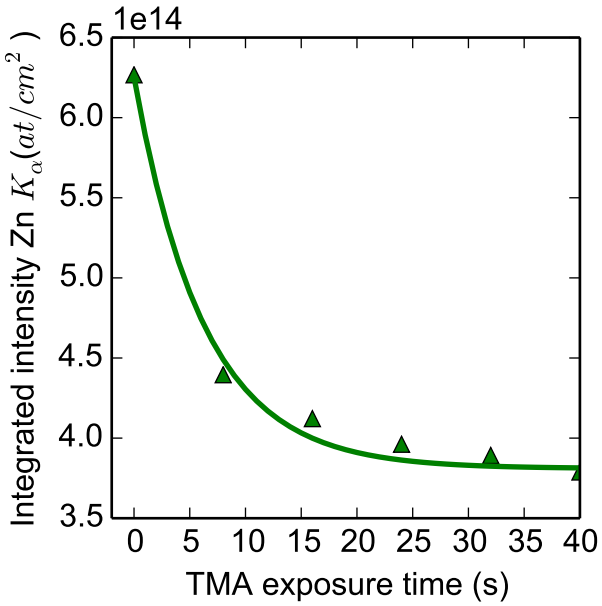

Figure 7.3: The integrated XRF intensity of the Zn Kα line indicating the amount of zinc present during the pretreatment of the monolayer of QDs with TMA. A clear reduction of the zinc content is observed, indicating etching of the ZnS shell of the QDs. The solid line is added as a guide for the reader.

thermal ALD of Al_2O_3. As shown in Figure 7.2, this pretreatment enables ZnO to be grown on the QDs during the subsequent ALD cycles, even if nucleation is still considerably delayed – taking $\approx$ 20 ALD cycles – as compared to the growth on the SiO_2 reference (see Fig. 7.2). Intriguingly, XRF also attests that the initial TMA exposure *reduces* the Zn surface density by 35-40%, see Figure 7.3. Since this pretreatment precedes any exposure to diethyl zinc and water, we attribute this to a substitution-reaction between TMA and Zn^{2+} present in the ZnS shell of the QDs or as surface adsorbed excess cations:

$$3\,Zn^{2+} + 2\,Al(CH_3)_3(g) \longrightarrow 2\,Al^{3+} + 3\,Zn(CH_3)_2(g) \tag{7.1}$$

A similar effect is known from literature, where TMA was reported to etch ZnO. [28, 31] Importantly, the evolution of the Zn Kα fluorescence intensity indicates that this is a self-limiting reaction. Most of the Zn substitution occurs during the first exposure to TMA and after multiple TMA exposures, the Zn surface density remains steady at ≈60% of its initial value. Since two ZnS monolayers were grown on these CdSe/CdS/ZnS QDs, both observations suggest that mainly surface adsorbed excess Zn is substituted for Al by exposure of the QDs to TMA.

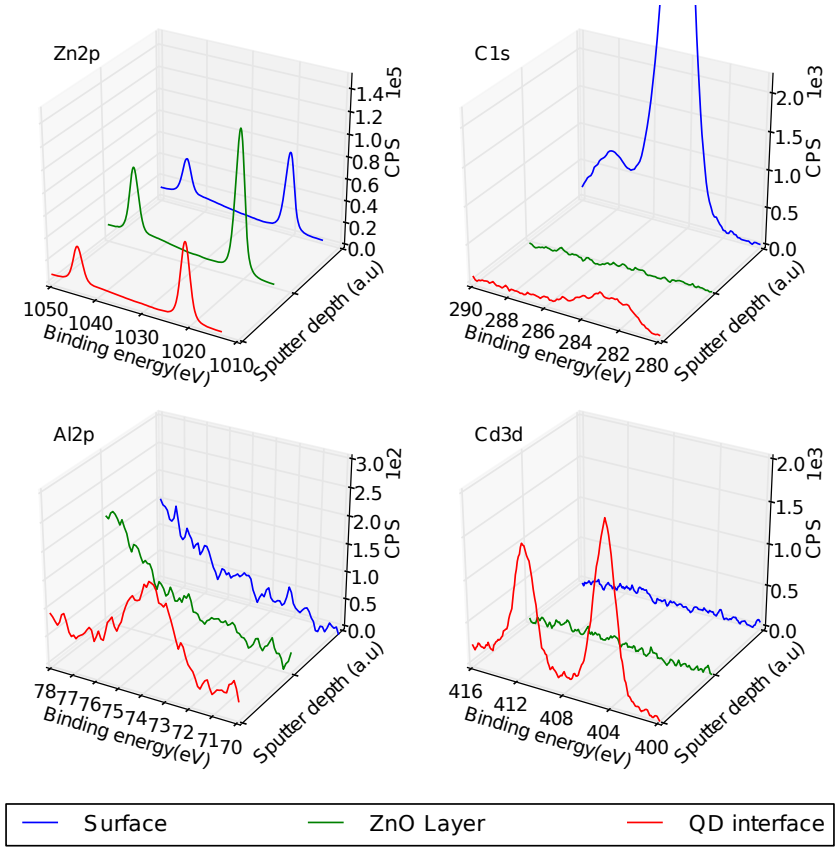

Figure 7.4: XPS spectra for Zn 2p, C 1s, Al 2p and Cd 3d. The spectra indicate the presence of Al and C near the quantum dots. This is the result of a partial substitution of the ZnS shell by Al_2S_3 during TMA pretreatment and the incorporation of the oleic acid ligands during ZnO growth.

We further analyzed the composition of the encapsulated layer by recording an XPS depth profile. Figure 7.4 represents three different XPS spectra for Zn, C, Al and Cd taken (blue) prior to any sputtering, (green) within the ZnO layer and (red) at the level of the QD monolayer. While Zn is present at each of these stages, it can be seen that aluminum is only detected together with cadmium. This indicates that Al is indeed present in the QD film, a finding supporting the above discussed partial substitution of the Zn shell by Al. A similar observation applies to carbon. Where the surface contains a considerable amount of aliphatic carbon, the ZnO layer is essentially carbon free. Near the QDs it is, however, detected again. We attribute this to the original oleate ligands of the QDs getting encapsulated by the ZnO matrix during ALD growth.

To investigate more in depth the relation between the Zn-for-Al substitution and the triggering of ZnO ALD growth, we analyzed possible changes in the QD ligand shell upon TMA exposure by *in situ* infrared spectroscopy. As shown in Figure 7.5, the as-deposited QD monolayer exhibits the infrared absorption fingerprint of oleate ligands, including the C-H and C=C stretch vibrations at around 3000 cm^{-1} and 1700 cm^{-1}, respectively, and features at around 1536 cm^{-1} that can be attributed to vibrations of the carboxylate moiety. [32] Remarkably, TMA hardly affects the appearance of the infrared spectrum. Apart from some minor variations in the carboxylate region, the C-H and C=C stretch vibrations keep their intensity and no new transitions appear. Hence, it appears that no direct chemical reaction between TMA and the oleate ligands takes place. Therefore, we have no evidence that TMA triggers ZnO ALD growth by converting oleate ligands into non-coordinating moieties and concomitantly making surface sites accessible for the ZnO ALD precursors. This suggests that rather than a release of originally blocked surface sites, it is the presence of surface-adsorbed Al^{3+} that triggers the ZnO ALD process. This is not unlikely since, opposite from Zn^{2+}, Al^{3+} is a hard Lewis acid. Moreover, it requires 3 rather than 2 oleate ligands for full coordination, such that interligand steric hindrance may leave surface adsorbed Al^{3+} less protected. Both elements can, in particular, promote the adsorption of H_2O to the QD surface after the Zn-for-Al substitution, a first step towards the complete ZnO ALD overgrowth of the QDs.

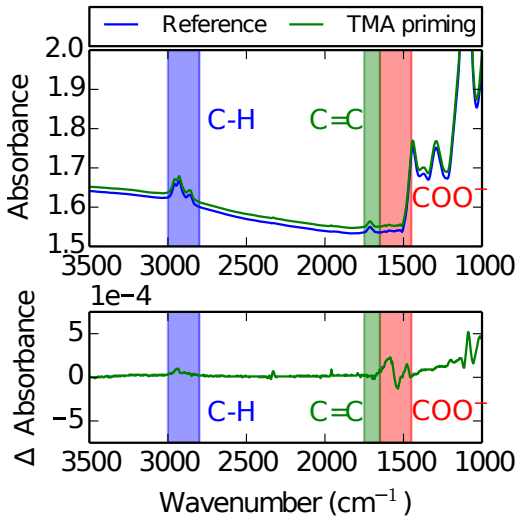

Figure 7.5: IR absorbance before and after TMA priming in the top graph shows the C-H and C=C fingerprint of the oleate ligands. The change in absorbance in the bottom graph shows no significant change in the region of C-H, C=C and COO^-, suggesting no direct chemical reaction between TMA and the oleate ligands takes place.

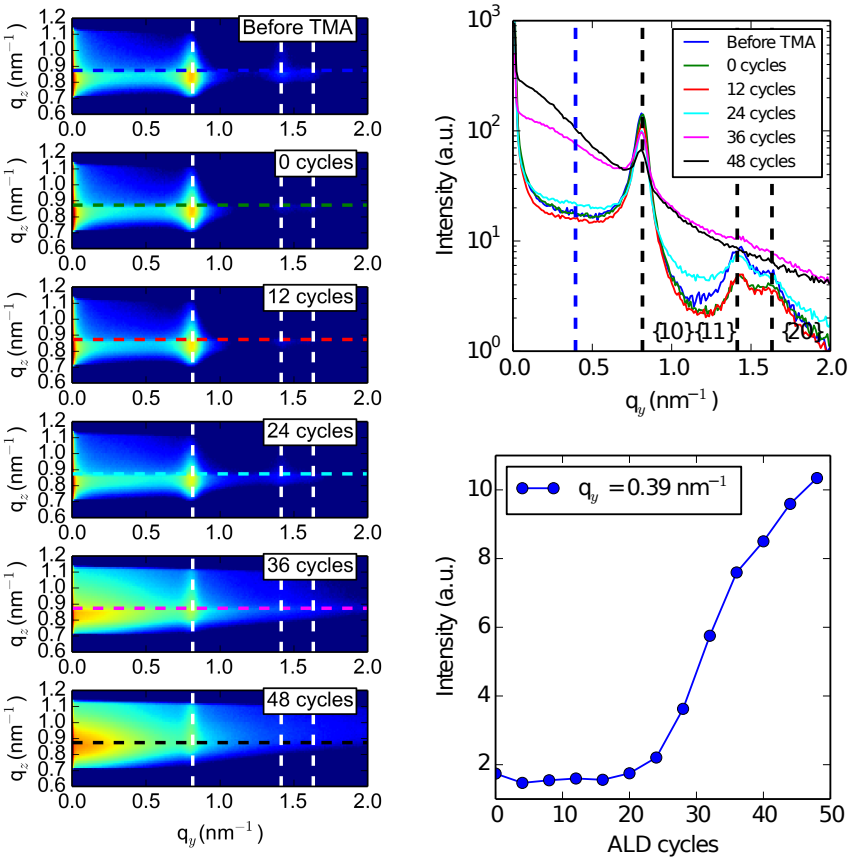

Figure 7.6: Evolution of the GISAXS pattern during TMA treatment and subsequent ZnO ALD encapsulation. The evolution of the 2D scattering pattern is shown in the left part of the figure. The top right shows the crosssections, as indicated on the right with the dotted lines and the bottom left shows the evolution of the scattering intensity at $q_y = 0.39\,nm^{-1}$. The peak positions do not change during deposition, indicating conservation of the original hexagonal order. The onset of the growth , after an incubation period of approximately 20 ALD cycles, can clearly be seen in the change of scattering intensity.

7.4.3 ZnO ALD Encapsulation and Monolayer Properties

In situ GISAXS enables us to monitor the influence of the TMA priming and the subsequent ZnO ALD on the structure of the quantum dot films. As shown in Figure 7.6 neither have an influence on the position of the scattering peaks indicating that the underlying local hexagonal ordering of the QD monolayer is not changed by the TMA treatment nor by the subsequent ZnO encapsulation. TMA exposure, on the other hand, does have a slight influence on the intensity of the scattering

features, mainly for high q_y values. This decrease in scattering intensity can be caused by a decrease in the electron density at the QD-interface in line with the replacement of Zn by Al. The evolution of the scattering intensity also shows the nucleation period of approximately 20 ALD cycles, in accordance with the evolution of the XRF-derived Zn coverage. During the first ALD cycles, the GISAXS pattern only changes slightly, as nucleation takes place and only little material is deposited. As growth progresses, we see an increase in overall scattering, which probably reflects the inherent roughness of the ZnO layer. We can, however, conclude that the pretreatment and encapsulation process do not influence the hexagonal ordering in the QD monolayer and the heating during deposition does not result in coalescence and/or melting of the individual QDs.

7.4.4 Effects on the Photoluminescence

Through the TMA pretreatment, we managed to encapsulate CdSe/CdS/ZnS QDs in a ZnO film. Analysis has shown that the 2D order within the monolayer of QDs is retained, but the composition of the outer shell is changed. The main remaining question is how this change in composition influences the properties of the QDs.

In Figure 7.7, the overall effect of the encapsulation process on the photoluminescence of the quantum dot layer is shown. Around half of the luminescent intensity remains after encapsulation. Analysis of a TMA treated monolayer of QDs without subsequent encapsulation, shows a similar drop in intensity. This suggests that the loss in quality can mainly be attributed to the alteration of the outer ZnS shell of the QDs during the TMA pretreatment, which was however required to initiate the ZnO growth.

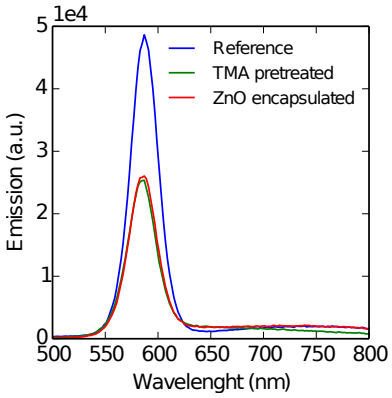

Figure 7.7: Photoluminescence response for a monolayer of QDs before deposition, after TMA pretreatment and after ZnO encapsulation. A similar change in intensity can be observed in the 2 latter cases, indicating that the loss in quality can mainly be attributed to the alteration of the outer ZnS shell during the TMA pretreatment.

7.5 Conclusions

To gain a more in-depth knowledge of the interaction between QDs and ALD precursors and the resulting metal oxide coating, we investigate the atomic layer deposition of ZnO on CdSe/CdS/ZnS core/shell/shell quantum dots. By using *in situ* XRF and GISAXS, we have shown that the ZnO nucleation and growth in successive ALD cycles is inhibited on as-deposited QDs, yet can be triggered by exposing the QDs to a single pulse of trimethylaluminium (TMA) vapor. We attribute this to the concomitant exchange of surface Zn by Al, where Al^{3+} surface sites may facilitate, *e.g.*, water absorption and thus initiate ZnO ALD growth. Additionally, the evolution of the GISAXS pattern during ALD shows that the QD ordering in the monolayer is not affected by ZnO coating. These results illustrate the important interplay between highly reactive ALD precursors and the QD surface.

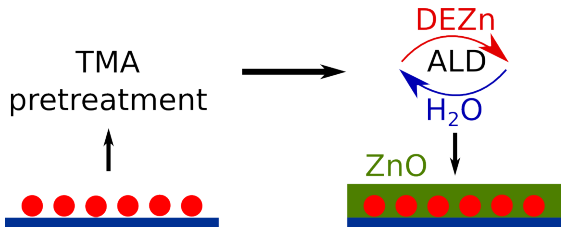

7.6 Acknowledgement

Christophe Detavernier and Jolien Dendooven also acknowledge funding by FWO-Vlaanderen, BOG-UGent GOA n° 01G01513 and the Hercules Foundation AUGE/09/014. Karl Ludwig acknowledges funding by the U.S. Department of Energy, under Contract n° DE-FG02-03ER46037. Use of the National Synchrotron Light Source, Brookhaven National Laboratory, was supported by the U.S. Department of Energy, Office of Science, Office of Basic Energy Sciences, under Contract n° DE-AC02-98CH10886

References

[1] D. V. Talapin, J. S. Lee, M. V. Kovalenko, and E. V. Shevchenko. *Prospects of Colloidal Nanocrystals for Electronic and Optoelectronic Applications*. Chem. Rev., 110(1):389–458, 2010.

[2] N. Gupta, J. Ibbetson, and B. Keller. *Quantum Dot Narrow-Band Downconverters for High Efficiency LEDs*, 2013.

[3] L. R. Bradshaw, K. E. Knowles, S. McDowall, and D. R. Gamelin. *Nanocrystals for Luminescent Solar Concentrators*. Nano Lett., 15(2):1315–1323, feb 2015.

[4] F. Hetsch, N. Zhao, S. V. Kershaw, and A. L. Rogach. *Quantum Dot Field Effect Transistors*. Mater. Today, 16(9):312–325, sep 2013.

[5] S. A. McDonald, G. Konstantatos, S. Zhang, P. W. Cyr, E. J. D. Klem, L. Levina, and E. H. Sargent. *Solution-Processed PbS Quantum Dot Infrared Photodetectors and Photovoltaics*. Nat. Mater., 4(2):138–142, feb 2005.

[6] A. Hassinen, I. Moreels, K. De Nolf, P. F. Smet, J. C. Martins, and Z. Hens. *Short-Chain Alcohols Strip X-Type Ligands and Quench the Luminescence of PbSe and CdSe Quantum Dots, Acetonitrile Does Not*. J. Am. Chem. Soc., 134(51):20705–20712, dec 2012.

[7] Y. Zhang, D. Zherebetskyy, N. D. Bronstein, S. Barja, L. Lichtenstein, A. P. Alivisatos, L.-W. Wang, and M. Salmeron. *Molecular Oxygen Induced In-Gap States in PbS Quantum Dots*. ACS Nano, 9(10):10445–10452, oct 2015.

[8] R. L. Puurunen. *Surface Chemistry of Atomic Layer Deposition: A Case Study for the Trimethylaluminum/Water Process*. J. Appl. Phys., 97(12):121301, 2005.

[9] A. H. Ip, A. J. Labelle, and E. H. Sargent. *Efficient, Air-Stable Colloidal Quantum Dot Solar Cells Encapsulated Using Atomic Layer Deposition of a Nanolaminate Barrier*. App. Phys. Lett., 103(26), dec 2013.

[10] J.-H. Choi, S. J. Oh, Y. Lai, D. K. Kim, T. Zhao, A. T. Fafarman, B. T. Diroll, C. B. Murray, and C. R. Kagan. *In Situ Repair of High-Performance, Flexible Nanocrystal Electronics for Large-Area Fabrication and Operation in Air*. ACS Nano, 7(9):8275–8283, sep 2013.

[11] S. H. Kim, P. H. Sher, Y. B. Hahn, and J. M. Smith. *Luminescence From Single CdSe Nanocrystals Embedded in ZnO Thin Films Using Atomic Layer Deposition*. Nanotechnology, 19(36):365202, sep 2008.

[12] K. Lambert, J. Dendooven, C. Detavernier, and Z. Hens. *Embedding Quantum Dot Monolayers in Al2O3 Using Atomic Layer Deposition*. Chem. Mater., 23(2):126–128, jan 2011.

[13] Y. Liu, M. Gibbs, C. L. Perkins, J. Tolentino, M. H. Zarghami, J. Bustamante, and M. Law. *Robust, Functional Nanocrystal Solids by Infilling With Atomic Layer Deposition*. Nano Lett., 11(12):5349–5355, dec 2011.

[14] I. Brunets, A. Aarnink, A. Boogaard, A. Kovalgin, R. Wolters, J. Holleman, and J. Schmitz. *Low-Temperature LPCVD of Si Nanocrystals From Disilane and Trisilane (Silcore®) Embedded in ALD-alumina for Non-Volatile Memory Devices*. Surf. Coatings Technol., 201(22-23):9209–9214, sep 2007.

[15] R. Ihly, J. Tolentino, Y. Liu, M. Gibbs, and M. Law. *The Photothermal Stability of PbS Quantum Dot Solids.* ACS Nano, 5(10):8175–86, oct 2011.

[16] C. Hu, A. Gassenq, Y. Justo, K. Devloo-Casier, H. Chen, C. Detavernier, Z. Hens, and G. Roelkens. *Air-Stable Short-Wave Infrared PbS Colloidal Quantum Dot Photoconductors Passivated With Al2O3 Atomic Layer Deposition*. Appl. Phys. Lett., 105(17):171110, oct 2014.

[17] S. H. Kim, P. H. Sher, Y. B. Hahn, and J. M. Smith. *Luminescence From Single CdSe Nanocrystals Embedded in ZnO Thin Films Using Atomic Layer Deposition*. Nanotechnology, 19(36):365202, sep 2008.

[18] S. ten Cate, Y. Liu, C. S. S. Sandeep, S. Kinge, A. J. Houtepen, T. J. Savenije, J. M. Schins, M. Law, and L. D. A. Siebbeles. *Activating Carrier Multiplication in PbSe Quantum Dot Solids by Infilling With Atomic Layer Deposition*. J. Phys. Chem. Lett., 4(11):1766–1770, jun 2013.

[19] J. J. Li, Y. A. Wang, W. Guo, J. C. Keay, T. D. Mishima, M. B. Johnson, and X. Peng. *Large-Scale Synthesis of Nearly Monodisperse CdSe/CdS Core/Shell Nanocrystals Using Air-Stable Reagents via Successive Ion Layer Adsorption and Reaction*. J. Am. Chem. Soc., 125(41):12567–12575, 2003.

[20] B. O. Dabbousi, J. Rodriguez-Viejo, F. V. Mikulec, J. R. Heine, H. Mattoussi, R. Ober, K. F. Jensen, and M. G. Bawendi. *(CdSe)ZnS CoreShell Quantum Dots: Synthesis and Characterization of a Size Series of Highly Luminescent Nanocrystallites*. J. Phys. Chem. B, 101(46):9463–9475, 1997.

[21] Y. Justo, I. Moreels, K. Lambert, and Z. Hens. *LangmuirBlodgett Monolayers of Colloidal Lead Chalcogenide Quantum Dots: Morphology and Photoluminescence*. Nanotechnology, 21(29):295606, jul 2010.

[22] K. Lambert, Y. Justo, J. S. Kamal, and Z. Hens. *Phase Transitions in Quantum-Dot Langmuir Films*. Angew. Chemie Int. Ed., 50(50):12058–12061, dec 2011.

[23] K. Devloo-Casier, J. Dendooven, K. F. Ludwig, G. Lekens, J. D'Haen, and C. Detavernier. *In Situ Synchrotron Based X-Ray Fluorescence and Scattering Measurements During Atomic Layer Deposition: Initial Growth of HfO_2 on Si and Ge Substrates*. Appl. Phys. Lett., 98(23):231905, 2011.

[24] J. Dendooven, S. Pulinthanathu Sree, K. De Keyser, D. Deduytsche, J. a. Martens, K. F. Ludwig, and C. Detavernier. *In Situ X-Ray Fluorescence Measurements During Atomic Layer Deposition: Nucleation and Growth of TiO_2 on Planar Substrates and in Nanoporous Films*. J. Phys. Chem. C, 115(14):6605–6610, apr 2011.

[25] J. Dendooven, S. Pulinthanathu Sree, K. De Keyser, D. Deduytsche, J. A. Martens, K. F. Ludwig, and C. Detavernier. *In Situ X-Ray Fluorescence Measurements During Atomic Layer Deposition: Nucleation and Growth of TiO_2 on Planar Substrates and in Nanoporous Films*. J. Phys. Chem. C, 115(14):6605–6610, apr 2011.

[26] J. Dendooven, K. Devloo-Casier, M. Ide, K. Grandfield, K. F. Ludwig, S. Bals, P. Van Der Voort, and C. Detavernier. *In Situ Study of ALD Processes Using Synchrotron-Based X-Ray Fluorescence and Scattering Techniques*. ECS Trans., 50(13):35–42, mar 2013.

[27] J. Dendooven, R. K. Ramachandran, K. Devloo-Casier, G. Rampelberg, M. Filez, H. Poelman, G. B. Marin, E. Fonda, and C. Detavernier. *Low-Temperature Atomic Layer Deposition of Platinum Using (Methylcyclopentadienyl)trimethylplatinum and Ozone*. J. Phys. Chem. C, 117(40):20557–20561, oct 2013.

[28] K. Devloo-Casier, K. F. Ludwig, C. Detavernier, and J. Dendooven. *In Situ Synchrotron Based X-Ray Techniques as Monitoring Tools for Atomic Layer Deposition*. J. Vac. Sci. Technol. A Vacuum, Surfaces, Film., 32(1):010801, 2014.

[29] J. Als-nielsen and D. McMorrow. *Elements of Modern X-Ray Physics*. John Wiley & Sons, Ltd, second edition, 2011.

[30] Z. Baji, Z. Lábadi, Z. E. Horváth, G. Molnár, J. Volk, I. Bársony, and P. Barna. *Nucleation and Growth Modes of ALD ZnO*. Cryst. Growth Des., 12(11):5615–5620, nov 2012.

[31] J. W. Elam and S. M. George. *Growth of ZnO/Al_2O_3 Alloy Films Using Atomic Layer Deposition Techniques*. Chem. Mater., 15(4):1020–1028, feb 2003.

[32] J. J. Hermans, K. Keune, A. V. Loon, and P. D. Iedema. *An Infrared Spectroscopic Study of the Nature of Zinc Carboxylates in Oil Paintings*. J. Anal. At. Spectrom., 30:1600–1608, 2015.

8

Paper IV: ALD encapsulation of supported CdSe/CdS/ZnS nanocrystals in a metal oxide matrix: TiO_2 vs Al_2O_3.*

8.1 Abstract

The influence of encapsulating a monolayer of CdSe/CdS/ZnS core/shell/shell quantum dots in ALD grown Al_2O_3 and TiO_2 is studied. The variation of film composition and nanocrystal arrangement during the ALD process are monitored *in situ* using x-ray fluorescence (XRF) and grazing incidence small angle x-ray scattering (GISAXS). A distinctive difference in nucleation behavior and interaction between the ALD precursors and the QDs can be observed, resulting in a significant effect on the photoluminescent response of the quantum dots. In the case of Al_2O_3 encapsulation, the photoluminescence quantum yield is reduced, while in the case of TiO_2 encapsulation, the photoluminescence quantum yield is enhanced. This illustrates the close chemical interaction of the ALD precursor with the surface of the quantum dots during the ALD process. Due to the aggressive nature of the ALD process to deposit Al_2O_3, the ALD process for TiO_2 deposition is to be preferred.

*Manuscript in preparation - Devloo-Casier K., Geiregat P., Ludwig K. F., van Stiphout K., Vantomme A., Rijckaert H., Van Driessche I., Hens Z., Detavernier C., Dendooven J.

8.2 Introduction

Atomic Layer Deposition (ALD) is a thin film deposition technique that employs the sequential exposure of a surface to a metal-containing precursor and a reactive gas. These react with the surface in a self-limiting way, resulting in an excellent thickness control and a conformal pinhole-free film with uniformity over large areas. The conformal nature allows ALD to be used for coating of irregular surfaces with high aspect ratio features with nanometer-thick films of typically metal oxides such as Al_2O_3, HfO_2, TiO_2 or ZnO. [1] This makes ALD a promising technique for the deposition of protective coatings. The function of the ALD coating can range from protecting moisture-sensitive materials, such as luminescent phosphors [2] and organic LEDs [3, 4] to corrosion protection [5, 6].

In recent years, ALD grown Al_2O_3 has been proposed as an encapsulation layer for quantum dot-based device stacks in order to obtain air-stable structures. [7, 8] The properties of these colloidal semiconductor nanocrystals or quantum dots (QD) are based on quantum-confinement effects allowing a wide tunable range in optical en electronic properties. Their solution based production method makes them ideal solution-processable building block for opto-electronic devices, nanoscale or flexible electronic components or solar energy conversion. [9] The need for encapsulating QD-based devices arises from a lack of long-term functionality. This is typically attributed to irreversible changes of the QD surface termination. Various studies have indeed shown that the photoluminescence quantum yield of QDs drops if surface-passivating moieties detach [10]. Instead of encapsulating the final QD stack, ALD can also be used to directly grow a thin film on the QDs outer shell. Al_2O_3 and ZnO films are known from literature to be able to directly grow on QD layers. [11, 12] These studies showed that ALD growth can protect, *e.g.*, PbS and PbSe QDs from oxidation, ripening and sintering [13–16] and CdSe QDs from deteriorating in air. [12, 17]

In this paper, we study the influence of encapsulating a monolayer of CdSe/CdS/ZnS core/shell/shell QDs in two different materials grown by ALD. The encapsulation by the widely used thermal ALD process, using TMA and water, for Al_2O_3 growth is compared to the thermal ALD process, using TDMAT and water, for TiO_2. Both materials are chosen to serve as a capping layer, since these are the most commonly grown ALD layers and are used in various application as protective barriers. The QD monolayers are made by Langmuir-Blodgett deposition and the variation of film composition and nanocrystal arrangement during the ALD process are monitored *in situ* using x-ray fluorescence (XRF) and grazing incidence small angle x-ray scattering (GISAXS).

The use of *in situ* XRF and GISAXS shows a distinctive difference in nucleation behavior and interaction between the ALD precursors and the QDs. Both processes have a significant effect on the photoluminescent response of the QDs.

In the case of Al_2O_3 encapsulation, the photoluminescence quantum yield is reduced, while in the case of TiO_2 encapsulation, the photoluminescence quantum yield is however enhanced. This illustrates the close chemical interaction of the ALD precursor with the QD-surface during the ALD process. The choice of ALD process and corresponding difference in precursor chemistry, is shown to have far reaching effects on the final functionality of a QD device. Due to the aggressive nature of the thermal ALD process to deposit Al_2O_3, the thermal ALD process for TiO_2 is to be preferred.

8.3 Experimental section

Preperation of the quantum dot monolayer. In this paper we study the encapsulation behavior of quantum dots. As a reference system, we use CdSe/CdS/ZnS core/shell QDs with oleic acid ligands, as CdSe/CdS/ZnS QDs are considered one of the most efficient visible emitting QDs. These QDs are produced using a successive ion layer adsorption and reaction (SILAR) method. [18, 19] The CdSe core has a diameter of 3 nm. The double shell consists of 3 layers of CdS and 2 layers of ZnS. These QDs have a photoluminescent quantum yield of $\approx 30\%$ in solution. The QDs are transferred from suspension to the silicon substrate through Langmuir-Blodgett deposition. A single monolayer of QDs, ordered (locally) in a hexagonal pattern is deposited. [20, 21] The final layer quality has been analyzed using AFM and TEM.

***In situ* synchrotron based X-ray fluorescence (XRF) and grazing incidence small angle scattering (GISAXS).** *In situ* synchrotron based X-ray fluorescence (XRF) and grazing incidence small angle scattering (GISAXS) are used to monitor the encapsulation by ALD of the QDs in a metal oxide matrix. [22–27] The UHV film growth facility installed at beamline X21 of the National Synchrotron Light Source at Brookhaven National Laboratory was adapted for thermal ALD and was used to perform the *in situ* experiments.

The incident x-ray energy was set to 10 keV. This energy allows the excitation of the Ti Kα lines at approximately 4.5 keV and of the Kα lines of Zn at approximately 8.6 keV. The Al Kα lines at 1.486 keV can also be excited, but the energy of these fluorescent x-rays is too low and are thus blocked by the beryllium exit window. During the *in situ* XRF measurements, an x-ray incident angle of 6.25° was chosen in combination width a silicon drift detector, mounted behind a Be window, positioned perpendicular to the sample. The XRF signal was integrated over a period of 30 s during the last pumping step of each ALD cycle. Based on Rutherford backscattering spectrometry (RBS) measurements performed after the *in situ* experiment, the XRF signal has been calibrated to correspond to a number of Ti and Zn atoms. To perform *in situ* GISAXS measurements, the x-ray inci-

dent angle was moved to 1 ° . The scattering intensity was collected during a 30 s interval by a Dectris Pilatus 100K area detector, mounted at a distance of approximately 80 cm from the sample. An evacuated flighttube was introduced between the detector and the Be exit window to reduce background scattering from the air. The GISAXS data were collected every 4 ALD cycles during both Al_2O_3 and TiO_2 growth.

ALD processes for encapsulation. Both materials, Al_2O_3 and TiO_2, are deposited using a thermal ALD process at a substrate temperature of 120 °C. To deposit Al_2O_3, trimethyl aluminium (TMA) and water are used as Al and O source and TiO_2 is deposited using Tetrakis(dimethylamido)titanium (TDMAT) and water as Ti and O source. Due to the low vapor pressure of TDMAT, argon is used as a carrier gas during TDMAT exposure. One ALD cycle consists of 8 s exposure to the metal containing precursor at 5 10^{-3} mbar, 20 s pumping, 8 s water exposure at 5 10^{-3} mbar, and again 40 s pumping. During the last pumping step, the *in situ* measurements are performed. The duration of each step is chosen to ensure saturation and avoid CVD-like side reactions. Under these conditions the growth per cycle (GPC) is approximately 1 Å and 0.5 Å per cycle for Al_2O_3 and TiO_2 respectively.

X-ray Photoelectron Spectroscopy (XPS) Measurements. X-ray photoelectron spectroscopy (XPS) was performed on the encapsulated quantum dot layers. A Theta Probe system of Thermo Scientific equiped wit an Al X-ray excitation source, operating at a base pressure of $\approx 10^{-10}$ mbar, was used to measure the samples. Argon milling was used to obtain a depth profile. The energy scale was calibrated using the surface carbon peak at 284.6 eV.

Transmission electron microscopy (TEM). To analyze the microstructure of the optimal final structure, a FEI Nova 600 Nanolab Dual Beam FIB-SEM and a JEOL JEM-2200FS TEM with Cs corrector was used. The sample for TEM investigations was prepared using ion milling techniques where a cross-sectional lamella was obtained via the FIB in-situ lift-out procedure with an Omniprobe extraction needle and top cleaning. The TEM was operated at 200 kV.

Photoluminescence Spectroscopy. A silicon PMT (Edinburgh Instruments) was used to measure photoluminescence(PL) spectra. The sample was excited with light from a Xenon discharge lamp at a wavelength of 350 nm. During time resolved measurements, a Fianium Supercontinuum laser, with an output at 450 nm at a repetition rate of 5 MHz is used as an excitation source. The count rates were limited to 1% of the stop rates to ensure single photon counting (TCSPC, time-correlated single photon counting). The refractive index of both Al_2O_3 and TiO_2 is larger than that of air (n=1) or ligands (n=1.5), which might induce a change

in PL efficiency through a change in the radiative decay rate, but this effect is negligible. For the PL measurements, seperate samples were deposited on a glass support, in order to minimize substrate coupling and absorption losses.

8.4 Results and discussion

8.4.1 CdSe/CdS/ZnS Quantum Dot Monolayers Reference System

In this study, a monolayer of CdSe/CdS/ZnS core/shell QDs with oleic acid ligands, deposited by Langmuir-Blodgett in a hexagonal pattern, is used as a reference system. The use of a monolayer is preferred over thicker stacks of QDs in order to avoid inconclusive results due to partial infilling of the film with ALD. The use of Langmuir-Blodgett deposition ensures a single monolayer,locally ordered in a hexagonal pattern, of QDs is deposited. [20] The transmission electron microscopy (TEM) image in Figure 8.1a shows this local order. The $\approx 6.0\,\mathrm{nm}$ QDs are mostly surrounded by 6 neighboring QDs with an average QD-QD interdistance of $\approx 7.5\,\mathrm{nm}$. The use of GISAXS allows us to confirm the hexagonal order over a larger area. In Figure 8.1c, the scattering pattern measured *in situ* just before ALD deposition features a central $q_y = 0\,\mathrm{nm}^{-1}$ peak corresponding to near specular reflection together with three side lobes that correspond to the hexagonal structure within the QD monolayer. The q_y positions of these lobes have specific ratios. The lobes are located at q_0, $\sqrt{3}q_0$ and $2q_0$. These correspond to the the $\{10\}$, $\{11\}$ and $\{20\}$ reflections of a two-dimensional hexagonal lattice. [28] This allows us to calculate the QD-to-QD distance as $2\pi/q_0$. Based on the GISAXS we get a distance between nearest neighbors of $7.7\,\mathrm{nm}$. This value is in agreement with that distance obtained, locally, from the TEM analysis. This allows us to conclude that the local hexagonal order within the monolayer of QDs, as seen in TEM, is present over the total area illuminated during GISAXS measurements.

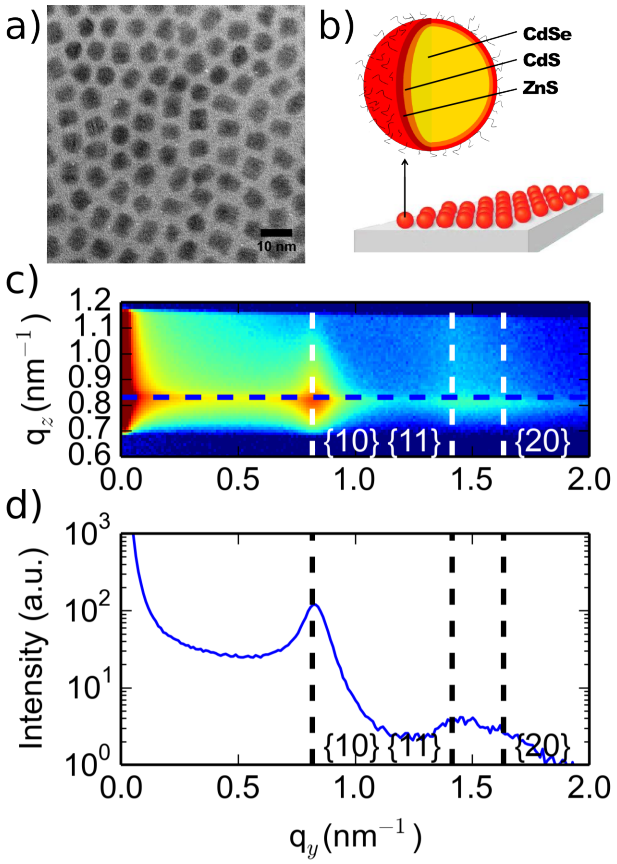

Figure 8.1: (a) TEM image of a monolayer of CdSe/CdS/ZnS quantum dots, showing the local hexagonal order. (b) Schematic representation of the as deposited monolayer of quantum dots. (c) GISAXS image measured for the as deposited monolayer of quantum dots. The three side lobes correspond to the 10, 11 and 20 reflections of a two-dimensional hexagonal lattice. The position of the cross section near the angle of total external reflection, shown in (d), is indicated with the blue dashed line.

8.4.2 X-ray Study During TiO_2 Encapsulation

The encapsulation process has been monitored using XRF and GISAXS. In the case of TiO_2 deposition, the intensity of the Ti Kα x-ray emission line can be directly used to quantify the amount of deposited Ti. The integrated intensity has been calibrated using the amount of Ti detected in the final layer by RBS. The XRF data clearly shows a nucleation delay in the growth curve (see Figure 8.2). During the first ≈30 ALD cycles, a reduced amount of TiO_2 is deposited, indicating a limited interaction between the precursors and the QD layer.

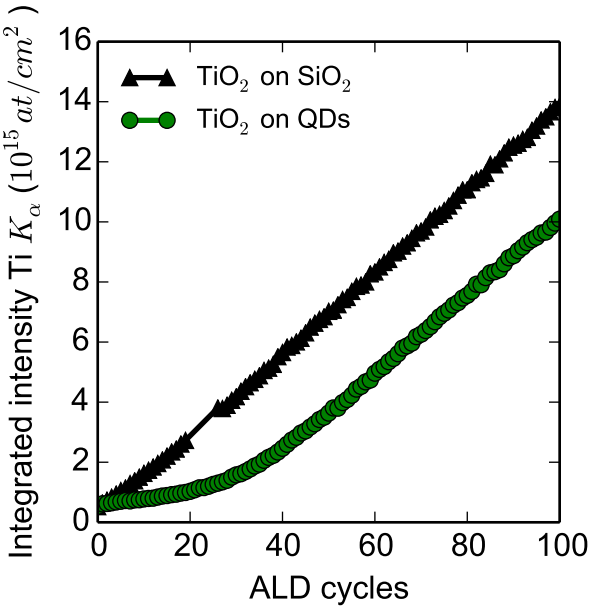

Figure 8.2: The integrated XRF intensity of the Ti Kα emission line indicating the amount of deposited TiO_2 during the encapsulation process. The growth curve for TiO_2 on a SiO_2 substrate is added as a reference. A clear nucleation delay can be seen for the growth on the monolayer of QDs.

During the encapsulation process, GISAXS data have been collected every 4 ALD cycles. A selection of GISAXS images is shown in Figure 8.3. During TiO_2 growth we see a gradual decrease in scattering intensity. This decrease can be attributed to a change in the electron density near the surface as the TiO_2 layer grows and gradually buries the QDs. The peak positions corresponding to the 2D hexagonal lattice, however, do not change during encapsulation. If we study the GISAXS data in detail, we can see that only after ≈20 ALD cycles, the scattering intensity starts to change. This is clearly visible in the cross-sections in figure 8.3, confirming the nucleation delay in the TiO_2 growth.

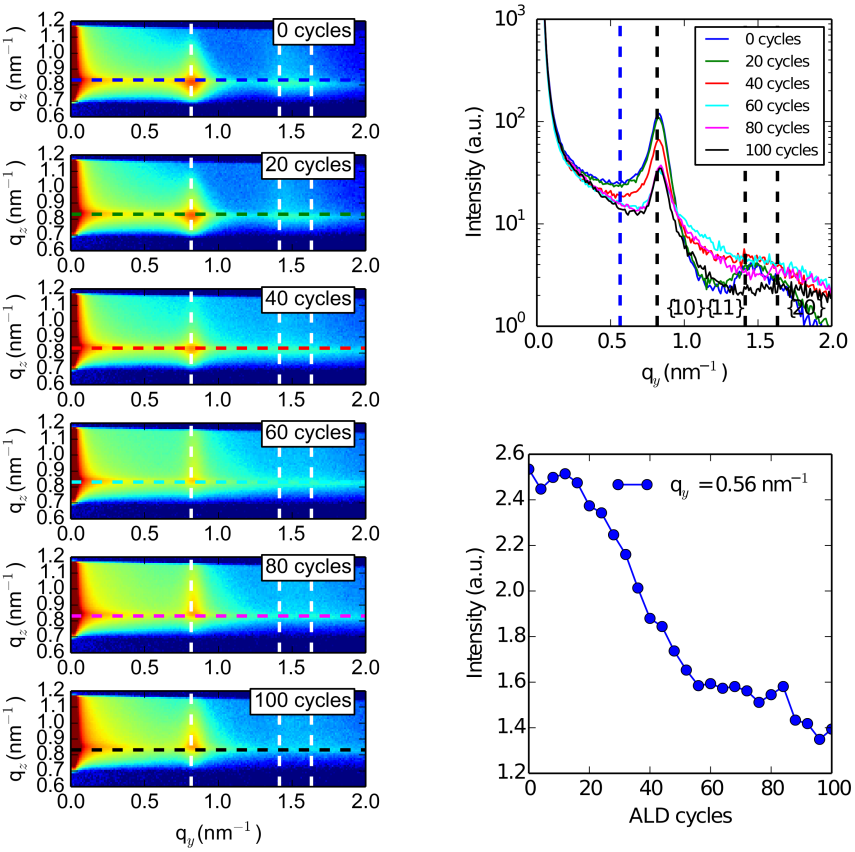

Figure 8.3: Evolution of the GISAXS pattern during TiO_2 encapsulation. The evolution of the 2D scattering pattern is shown in the left part of the figure. The top right shows the cross-sections, as indicated on the right with the dotted lines and the bottom left shows the evolution of the scattering intensity at $q_y = 0.56\,nm^{-1}$. The peak positions corresponding to the 2D hexagonal lattice do not change during deposition. The nucleation delay can clearly be seen in the change of scattering intensity.

8.4.3 X-ray Study During Al_2O_3 Encapsulation

Similarly to the previous section, the encapsulation in Al_2O_3 has been monitored using XRF and GISAXS. However, in contrast to Ti Kα, the energy of the Al Kα emission lines is too low to pass the Be exit window. The XRF data therefore does not contain any information about the amount of deposited Al_2O_3. The GISAXS data, however, contains similar information as during the TiO_2 encapsulation process.

A selection of GISAXS images is shown in Figure 8.4. From the evolution in scattering intensity, we can conclude, similar as in the case of TiO_2 encapsulation, that the Al_2O_3 layer changes the scattering surface and gradually buries the QDs. The peak positions corresponding to the 2D hexagonal lattice, again, do not change during encapsulation. If we study the GISAXS data in detail, we can see that already after 4 ALD cycles the scattering intensities is changing, in contrast to during the first stages of TiO_2 growth. This indicates that the Al_2O_3 starts growing from the first ALD cycles. From this we can conclude that no nucleation delay is present during Al_2O_3 growth. This has to be the result of more interaction between the TMA precursor molecules and the QDs, compared with the interaction between the TDMAT precursor molecules and the QDs during TiO_2 deposition.

During the last ALD cycles Al_2O_3 deposition, the general background intensity increases, while the peak intensity stays at the same level. This corresponds to the increase of general scattering from the roughness of the Al_2O_3, while keeping the scattering contribution of the fully encapsulated QDs constant. This is not yet observed in the case of TiO_2 as the lower steady-state GPC for this process leads to a lower layer thickness.

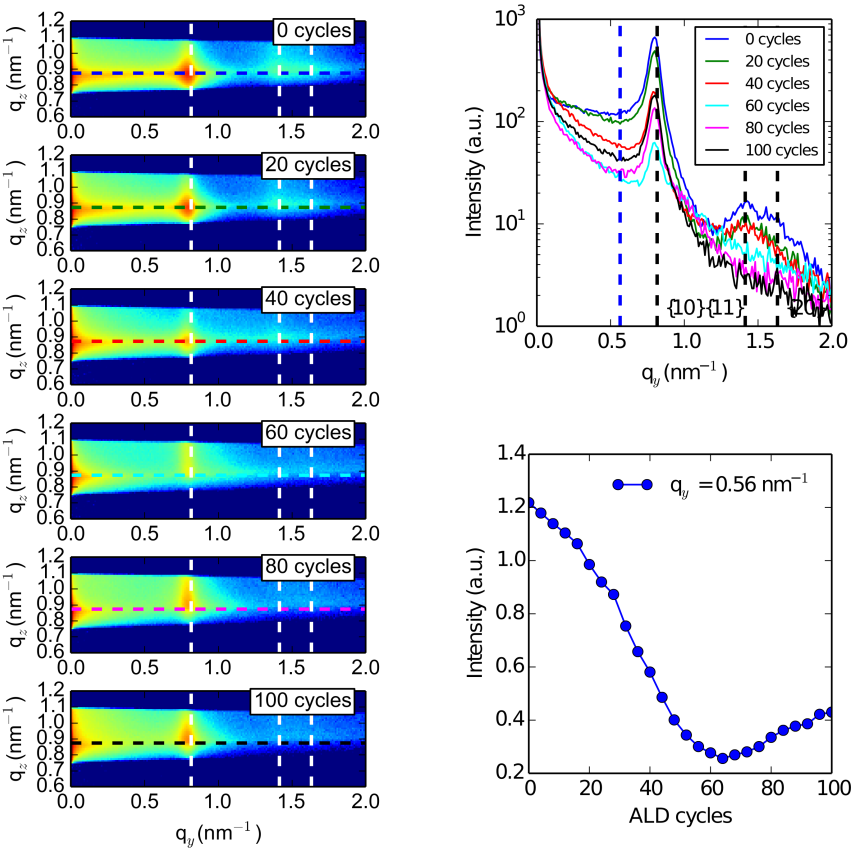

Figure 8.4: Evolution of the GISAXS pattern during Al_2O_3 encapsulation. The evolution of the 2D scattering pattern is shown in the left part of the figure. The top right shows the cross-sections, as indicated on the right with the dotted lines and the bottom left shows the evolution of the scattering intensity at $q_y = 0.56\,nm^{-1}$. The peak positions corresponding to the 2D hexagonal lattice do not change during deposition. No nucleation delay is observed.

8.4.4 Effect of the encapsulation process on the Photoluminescence

From the *in situ* x-ray analysis, we have learned that the monolayer of QDs retains its hexagonal order and can be encapsulated by both Al_2O_3 and TiO_2 using thermal ALD. An important remaining question is how the encapsulation process has affected the properties of the QDs. The used CdSe/CdS/ZnS core/shell QDs are highly luminescent, therefore, the photoluminescence of the encapsulated layers is a good measure of the quality of the material and whether this is preserved during ALD treatment. (see Figure 8.5) Encapsulation by the used processes has a significant effect on the final photoluminescence of the encapsulated QDs. The Al_2O_3 coated QDs have lost most of their luminescence, while the TiO_2 coated QDs show an increase in photoluminescence efficiency by approximately a factor 2.5. The increase in photoluminescence can be linked to the reduction of non-radiative recombination paths. In Figure 8.6 a time-resolved photoluminescence measurement is shown, comparing an uncoated monolayer of QDs to a monolayer of TiO_2 encapsulated QDs. The lifetime is fitted to an exponetial decay with an additional constant term to account for the noise at low intensity. An increase in the radiative lifetime after TiO_2 encapsulation indicates that the non-radiative reaction rate has been reduced. We note that the thickness of the layer is too thin and the dielectric contrast between QDs and oxide too small to cause any substantial local field effects that could alter the lifetime to this degree.

8.4.5 Interaction with the QDs During ALD

The difference in effect on the PL between both materials, has to be attributed to the difference in interaction between the ALD precursors and the QDs. When studying the Zn Kα emission line, corresponding to the Zn atoms in the outer ZnS shell of the QDs, a distinctive difference can be observed. (see Figure 8.7) In the case of TiO_2 growth, no change in the amount of detected Zn is observed, indicating that the ZnS shell remains intact. However, during Al_2O_3 growth the Zn surface density is reduced by approximately 35-40%. This reduction can be attributed to a substitution-reaction between TMA and Zn^{2+} present in the ZnS shell of the QDs or as surface adsorbed excess cations:

$$3\,\mathrm{Zn}^{2+} + 2\,\mathrm{Al(CH_3)_3(g)} \longrightarrow 2\,\mathrm{Al}^{3+} + 3\,\mathrm{Zn(CH_3)_2(g)} \tag{8.1}$$

A similar effect is known from literature, where TMA can etch ZnO. [27, 29] The XRF data also indicates that this is a self-limiting reaction, as most Zn gets removed during the first exposure to TMA during the first ALD cycle, whereas during the later ALD cycles, the Zn content remains constant.

The XRF data has shown that there is a distinctive difference in interaction between the ALD precursors and the QD outer surface during TiO_2 and Al_2O_3

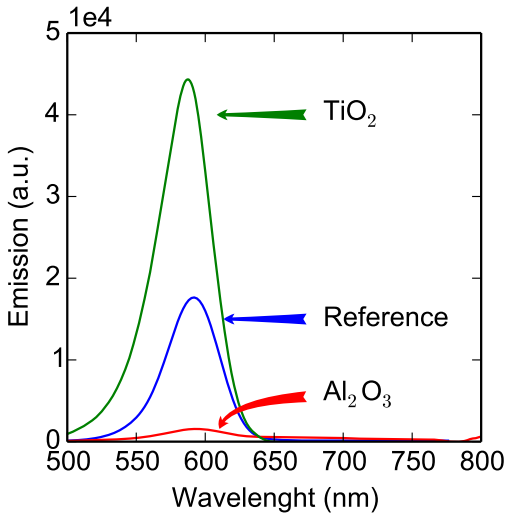

Figure 8.5: Photo luminescence response for a monolayer of QDs before encapsulation, after TiO_2 encapsulation and after Al_2O_3 encapsulation. The QDs encapsulated in TiO_2 show an enhancement in photoluminescence. The QDs encapsulated in Al_2O_3 show a large reduction in photoluminescence

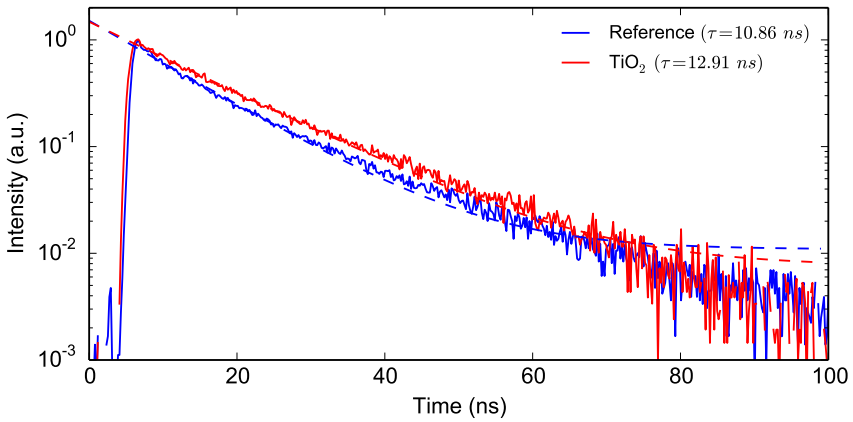

Figure 8.6: Time-resolved PL measurement, indicating an increase in the radiative lifetime after TiO_2 encapsulation

encapsulation. Additionally, XPS is used to examine possible differences in interactions with the oleate ligands. In Figure 8.8 an XPS depth profile is shown. At the surface, a large presence of aliphatic carbon can be detected. The Cd from the QDs can already be seen at the surface, due to the low thickness of the encapsulating

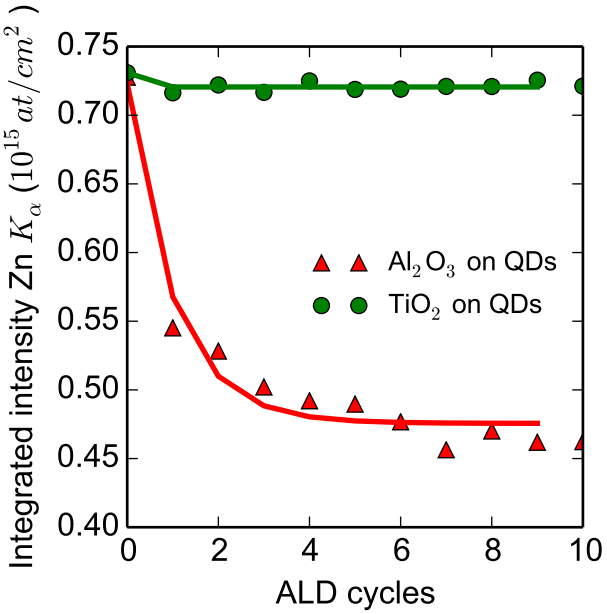

Figure 8.7: The integrated XRF intensity of the Zn Kα emission line indicating the amount of zinc present from the ZnS shell. During TiO_2 growth the ZnS shell stays intact, while during Al_2O_3 growth, a reduction of the zinc content is observed. The solid lines are added as a guide for the reader.

TiO_2 layer. Inside the TiO_2 layer, no carbon is detected. Near the QD interface, the presence of carbon is seen, indicating that the oleic acid ligands are being incorporated into the TiO_2 matrix. The C1s peak position is slightly shifted, due to the argon milling involved in the depth profiling. In the case of Al_2O_3 encapsulation, the carbon from the ligands is also still present at the QD-Al_2O_3 interface. Because in both cases the ligands get buried during encapsulation, we can mainly attribute the distinction between both processes in photoluminescent response to the different interaction with the outer ZnS shell.

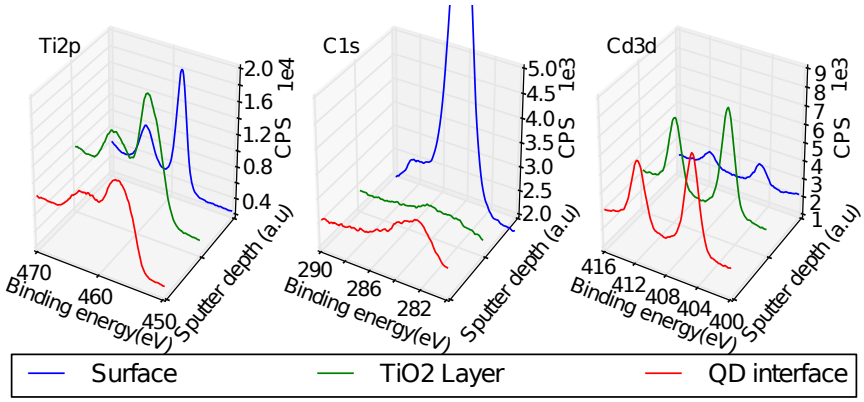

Figure 8.8: XPS spectra for Ti 2p, C 1s and Cd 3d. The spectra indicate the presence of carbon near the quantum dots, caused by the incorporation of the oleic acid ligands.

The quality of the QD encapsulation by TiO_2 was further examined using bright field cross-sectional TEM. In Figure 8.9 a cross-section TEM image is shown for a monolayer of QDs after 100 cycles of TiO_2 deposition. The fast fourier transform (FFT) of the QD-layer in combination with elemental analysis allows identification of each individual layer. The TiO_2 layer forms a uniform, conformal barrier on top of the QDs.

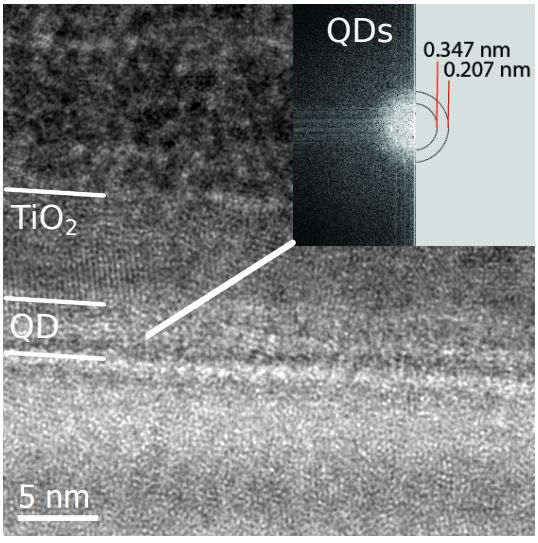

Figure 8.9: Bright field cross-sectional TEM images of the TiO_2 encapsulated monolayer of quantum dots. The inset show the Fast Fourier Transform (FFT) of the quantum dot layer, corresponding to the polycrystalline quantum dots

8.4.6 The Role of the TiO_2 Layer

Above, we have shown that the material choice for an ALD grown protective layer can have important effects on the functionality of encapsulated QDs. Exposing CdSe/CdS/ZnS QDs to an Al_2O_3 ALD process reduces the PL response, while using a TiO_2 ALD process enhances the PL.

To increase our understanding in the role of the TiO_2, additional experiment combining the Al_2O_3 and TiO_2 process where performed. 100 ALD cycles of the Al_2O_3 process were performed after, respectively, 5 exposures to TDMAT, 5 ALD cycles of TiO_2 and 40 ALD cycles of TiO_2. The effect on the PL response can be seen in Figure 8.10. In the first 2 cases the decrease in PL due to the subsequent Al_2O_3 growth is reduced, indicating that the TDMAT interacts with the QDs during the first exposures, partially protecting the QDs from the subsequent etching by TMA. Similarly, 5 ALD cycles of the TiO_2 process provide similar protection. Combining 40 ALD cycles of the TiO_2 process with 100 ALD cycles of the Al_2O_3 process, enhances the PL response in a similar way as when depositing a 100 ALD cycles of TiO_2. This shows that 40 ALD cycles of TiO_2 deposition can provide the enhancement effect on the PL, while providing sufficient protection from post processing.The XRF data shown in Figure 8.2 provides some explanation for the difference between using 5 ALD cycles and 40 ALD cycles. From the data it is clear that 5 ALD cycles only provide a low amount of TiO_2, leading to only a partial layer. The amount of deposited TiO_2 40 ALD cycles corresponds to approximately a TiO_2 layer with a thickness of 1 nm.

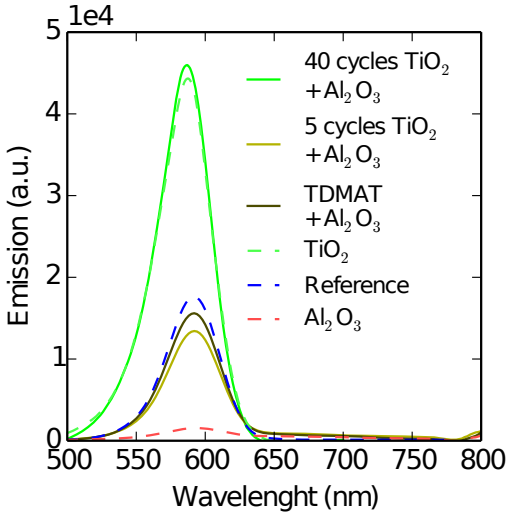

Figure 8.10: Photo luminescence response when first exposing the monolayer of QDs to TDMAT or a number of TiO_2 ALD cycles before continuing Al_2O_3 encapsulation.

8.5 Conclusions

The encapsulation of CdSe/CdS/ZnS core/shell/shell quantum dots in a Al_2O_3 and TiO_2 protective layer by ALD has been investigated. By using *in situ* XRF and GISAXS, we have shown the difference in nucleation behavior and interaction between the ALD precursors and the QDs. Both processes have a significant effect on the PL response of the QDs. This stresses that the choice in ALD process can have far reaching effects on the final functionality of a QD device. In the case of the widely used ALD process for Al_2O_3 encapsulation, the photoluminescence quantum yield is reduced. This effect can be attributed to a substitution-reaction between TMA and Zn^{2+} present in the ZnS shell of the QDs or as surface adsorbed excess cations. In the case of TiO_2 deposition, the photoluminescence quantum yield is however enhanced. This shows that even the deposition of a passive protective layer by ALD can have a significant effect on the final functionality, due to the inherent chemical nature of ALD-reactions.

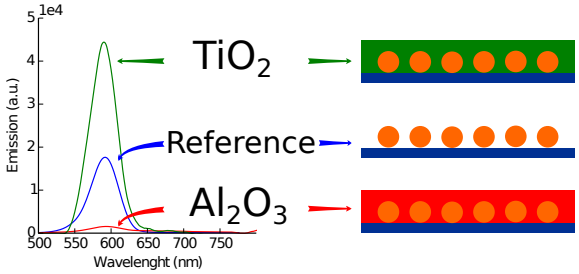

8.6 Acknowledgement

Christophe Detavernier and Jolien Dendooven also acknowledge funding by FWO-Vlaanderen, and GOA n° 01G01513. Karl Ludwig acknowledges funding by the U.S. Department of Energy, under Contract n° DE-FG02-03ER46037. Use of the National Synchrotron Light Source, Brookhaven National Laboratory, was supported by the U.S. Department of Energy, Office of Science, Office of Basic Energy Sciences, under Contract n° DE-AC02-98CH10886

References

[1] R. L. Puurunen. *Surface Chemistry of Atomic Layer Deposition: A Case Study for the Trimethylaluminum/Water Process*. J. Appl. Phys., 97(12):121301, 2005.

[2] N. Avci, J. Musschoot, P. F. Smet, K. Korthout, A. Avci, C. Detavernier, and D. Poelman. *Microencapsulation of Moisture-Sensitive CaS:Eu^{2+} Particles With Aluminum Oxide*. J. Electrochem. Soc., 156(11):J333, 2009.

[3] a. P. Ghosh, L. J. Gerenser, C. M. Jarman, and J. E. Fornalik. *Thin-Film Encapsulation of Organic Light-Emitting Devices*. Appl. Phys. Lett., 86(22):223503, 2005.

[4] J. Meyer, D. Schneidenbach, T. Winkler, S. Hamwi, T. Weimann, P. Hinze, S. Ammermann, H.-H. Johannes, T. Riedl, and W. Kowalsky. *Reliable Thin Film Encapsulation for Organic Light Emitting Diodes Grown by Low-Temperature Atomic Layer Deposition*. Appl. Phys. Lett., 94(23):233305, 2009.

[5] R. Matero, M. Ritala, M. Leskelä, T. Salo, J. Aromaa, and O. Forsén. *Atomic Layer Deposited Thin Films for Corrosion Protection*. J. Pysics IV Fr., 9:PR8–493, 1999.

[6] M. Kemell, M. Ritala, M. Leskelä, R. Groenen, S. Lindfors, M. Kernell, M. Ritala, M. Leskelä, R. Groenen, and S. Lindfors. *Coating of Highly Porous Fiber Matrices by Atomic Layer Deposition*. Chem. Vap. Depos., 14(11-12):347–352, nov 2008.

[7] A. H. Ip, A. J. Labelle, and E. H. Sargent. *Efficient, Air-Stable Colloidal Quantum Dot Solar Cells Encapsulated Using Atomic Layer Deposition of a Nanolaminate Barrier*. App. Phys. Lett., 103(26), dec 2013.

[8] J.-H. Choi, S. J. Oh, Y. Lai, D. K. Kim, T. Zhao, A. T. Fafarman, B. T. Diroll, C. B. Murray, and C. R. Kagan. *In Situ Repair of High-Performance, Flexible Nanocrystal Electronics for Large-Area Fabrication and Operation in Air*. ACS Nano, 7(9):8275–8283, sep 2013.

[9] D. V. Talapin, J. S. Lee, M. V. Kovalenko, and E. V. Shevchenko. *Prospects of Colloidal Nanocrystals for Electronic and Optoelectronic Applications*. Chem. Rev., 110(1):389–458, 2010.

[10] A. Hassinen, I. Moreels, K. De Nolf, P. F. Smet, J. C. Martins, and Z. Hens. *Short-Chain Alcohols Strip X-Type Ligands and Quench the Luminescence of PbSe and CdSe Quantum Dots, Acetonitrile Does Not*. J. Am. Chem. Soc., 134(51):20705–20712, dec 2012.

[11] S. H. Kim, P. H. Sher, Y. B. Hahn, and J. M. Smith. *Luminescence From Single CdSe Nanocrystals Embedded in ZnO Thin Films Using Atomic Layer Deposition*. Nanotechnology, 19(36):365202, sep 2008.

[12] K. Lambert, J. Dendooven, C. Detavernier, and Z. Hens. *Embedding Quantum Dot Monolayers in Al2O3 Using Atomic Layer Deposition*. Chem. Mater., 23(2):126–128, jan 2011.

[13] I. Brunets, A. Aarnink, A. Boogaard, A. Kovalgin, R. Wolters, J. Holleman, and J. Schmitz. *Low-Temperature LPCVD of Si Nanocrystals From Disilane and Trisilane (Silcore®) Embedded in ALD-alumina for Non-Volatile Memory Devices*. Surf. Coatings Technol., 201(22-23):9209–9214, sep 2007.

[14] R. Ihly, J. Tolentino, Y. Liu, M. Gibbs, and M. Law. *The Photothermal Stability of PbS Quantum Dot Solids.* ACS Nano, 5(10):8175–86, oct 2011.

[15] Y. Liu, M. Gibbs, C. L. Perkins, J. Tolentino, M. H. Zarghami, J. Bustamante, and M. Law. *Robust, Functional Nanocrystal Solids by Infilling With Atomic Layer Deposition*. Nano Lett., 11(12):5349–5355, dec 2011.

[16] C. Hu, A. Gassenq, Y. Justo, K. Devloo-Casier, H. Chen, C. Detavernier, Z. Hens, and G. Roelkens. *Air-Stable Short-Wave Infrared PbS Colloidal Quantum Dot Photoconductors Passivated With Al2O3 Atomic Layer Deposition*. Appl. Phys. Lett., 105(17):171110, oct 2014.

[17] S. H. Kim, P. H. Sher, Y. B. Hahn, and J. M. Smith. *Luminescence From Single CdSe Nanocrystals Embedded in ZnO Thin Films Using Atomic Layer Deposition*. Nanotechnology, 19(36):365202, sep 2008.

[18] J. J. Li, Y. A. Wang, W. Guo, J. C. Keay, T. D. Mishima, M. B. Johnson, and X. Peng. *Large-Scale Synthesis of Nearly Monodisperse CdSe/CdS Core/Shell Nanocrystals Using Air-Stable Reagents via Successive Ion Layer Adsorption and Reaction*. J. Am. Chem. Soc., 125(41):12567–12575, 2003.

[19] B. O. Dabbousi, J. Rodriguez-Viejo, F. V. Mikulec, J. R. Heine, H. Mattoussi, R. Ober, K. F. Jensen, and M. G. Bawendi. *(CdSe)ZnS CoreShell Quantum Dots: Synthesis and Characterization of a Size Series of Highly Luminescent Nanocrystallites*. J. Phys. Chem. B, 101(46):9463–9475, 1997.

[20] Y. Justo, I. Moreels, K. Lambert, and Z. Hens. *LangmuirBlodgett Monolayers of Colloidal Lead Chalcogenide Quantum Dots: Morphology and Photoluminescence*. Nanotechnology, 21(29):295606, jul 2010.

[21] K. Lambert, Y. Justo, J. S. Kamal, and Z. Hens. *Phase Transitions in Quantum-Dot Langmuir Films*. Angew. Chemie Int. Ed., 50(50):12058–12061, dec 2011.

[22] K. Devloo-Casier, J. Dendooven, K. F. Ludwig, G. Lekens, J. D'Haen, and C. Detavernier. *In Situ Synchrotron Based X-Ray Fluorescence and Scattering Measurements During Atomic Layer Deposition: Initial Growth of HfO_2 on Si and Ge Substrates*. Appl. Phys. Lett., 98(23):231905, 2011.

[23] J. Dendooven, S. Pulinthanathu Sree, K. De Keyser, D. Deduytsche, J. a. Martens, K. F. Ludwig, and C. Detavernier. *In Situ X-Ray Fluorescence Measurements During Atomic Layer Deposition: Nucleation and Growth of TiO_2 on Planar Substrates and in Nanoporous Films*. J. Phys. Chem. C, 115(14):6605–6610, apr 2011.

[24] J. Dendooven, S. Pulinthanathu Sree, K. De Keyser, D. Deduytsche, J. A. Martens, K. F. Ludwig, and C. Detavernier. *In Situ X-Ray Fluorescence Measurements During Atomic Layer Deposition: Nucleation and Growth of TiO_2 on Planar Substrates and in Nanoporous Films*. J. Phys. Chem. C, 115(14):6605–6610, apr 2011.

[25] J. Dendooven, K. Devloo-Casier, M. Ide, K. Grandfield, K. F. Ludwig, S. Bals, P. Van Der Voort, and C. Detavernier. *In Situ Study of ALD Processes Using Synchrotron-Based X-Ray Fluorescence and Scattering Techniques*. ECS Trans., 50(13):35–42, mar 2013.

[26] J. Dendooven, R. K. Ramachandran, K. Devloo-Casier, G. Rampelberg, M. Filez, H. Poelman, G. B. Marin, E. Fonda, and C. Detavernier. *Low-Temperature Atomic Layer Deposition of Platinum Using (Methylcyclopentadienyl)trimethylplatinum and Ozone*. J. Phys. Chem. C, 117(40):20557–20561, oct 2013.

[27] K. Devloo-Casier, K. F. Ludwig, C. Detavernier, and J. Dendooven. *In Situ Synchrotron Based X-Ray Techniques as Monitoring Tools for Atomic Layer Deposition*. J. Vac. Sci. Technol. A Vacuum, Surfaces, Film., 32(1):010801, 2014.

[28] J. Als-nielsen and D. McMorrow. *Elements of Modern X-Ray Physics*. John Wiley & Sons, Ltd, second edition, 2011.

[29] J. W. Elam and S. M. George. *Growth of ZnO/Al_2O_3 Alloy Films Using Atomic Layer Deposition Techniques*. Chem. Mater., 15(4):1020–1028, feb 2003.

9

Summary, Conclusions and Suggestions for Future Work

9.1 Summary and Conclusions

In this thesis, *in situ* synchrotron based x-ray techniques were introduced as a tool to study ALD processes and implemented to investigate ALD encapsulation of Quantum Dots. The most significant insights and remarks are summarized below.

Part I: X-ray Techniques for In Situ Monitoring of ALD

In the first part of this work, the focus was on the introduction of various synchrotron based x-ray techniques and their corresponding possibilities in ALD research.

***In situ* synchrotron based x-ray techniques** Extending the wavelength range of optical in situ techniques to x-rays enables the use of a new range of techniques (e.g. XRR, XRF and GISAXS) during ALD. This expands the information available in the study of layer growth during ALD, both on planar and on complex structures. The use of synchrotron based x-rays is beneficial to in situ studies. First of all, the high photon flux reduces measurement time and lowers the detection limit. Secondly, the energy tunability available at a synchrotron enables GISAXS and XAS. All these techniques are especially sensitive to changes at the (sub-)nanometer scale. As the changes during ALD growth are typically of this

order, they are ideally suited for *in situ* studies. Below, the techniques introduced in chapter 4 and 5 are listed with their respective relevance for ALD research.

XRR
X-ray reflectivity (XRR) can be used to determine the thickness, roughness and density of ALD grown thin films.

GISAXS
Grazing incidence small angle x-ray scattering (GISAXS) allows the morphological characterization of ALD grown nanoscale objects (e.g. particles) or allows monitoring of nanoscale structures during ALD encapsulation or modification.

XRD
X-ray diffraction (XRD) enables the study of the properties of crystalline materials. For *in situ* ALD research, XRD is limited to processes depositing (poly-)crystalline materials.

XRF
X-ray fluorescence (XRF) is a spectroscopy technique that allows the study of the composition of an ALD grown material with submonolayer precision.

XAS (in vacuo)
X-ray absorption spectroscopy (XAS) can be used to study the local atomic environment within a material.

XPS (in vacuo)
X-ray photoelectron spectroscopy (XPS) allows the study of composition and chemical state of the elements in a material.

These *in situ* synchrotron based x-ray techniques form a new set of valuable tools for the study of ALD processes.

Part II: ALD Encapsulation of Quantum Dots

In the second part of this work, two of the introduced techniques, XRF and GISAXS, were applied to the study of ALD encapsulation of quantum dots (QDs) and the accompanying interaction between the ALD precursors and the surface of the QDs.

Encapsulation Here, the ALD encapsulation of a monolayer of CdSe/CdS/ZnS QDs is used as a model system. The encapsulation by respectively ZnO, Al_2O_3 and TiO_2 has been studied. Each of these encapsulation processes has a different level of interaction with the QDs, causing a significant effect on the final properties of the QD-layer. The differences are summarized below.

ZnO encapsulation

The use of *in situ* XRF allowed us to identify the inhibition of ZnO growth on as-deposited QDs. The growth can however be triggered by exposing the QDs to TMA vapor. *In situ* XRF enabled the detection of a reduction in the Zn content of the QDs during this pretreatment. This can be attributed to an Al-for-Zn substitution-reaction at the QD surface, involving the substitution of approximately one third of the original Zn by Al. This surface reaction primes the QD-surface for further ZnO growth, but causes a reduction of the photoluminescence quantum yield. *In situ* GISAXS showed the preservation of the hexagonal order within the QD-layer and supplied complimentary information to the XRF data during the encapsulation process.

TiO_2 encapsulation

In situ XRF and GISAXS have been used to show a small nucleation delay during TiO_2 encapsulation. The encapsulation process, however, leads to a uniform and conformally coated QD-layer. Based on the *in situ* XRF, it has been shown that the used ALD process preserves the outer shell of the QDs. The protective layer not only conserves the original photoluminescence quantum yield, but even causes an enhancement.

Al_2O_3 encapsulation

In situ GISAXS suggests the absence of a nucleation delay during Al_2O_3 encapsulation. The encapsulation process has, however, causes a significant reduction in the photoluminescent response. *In situ* XRF provides a unique insight in the responsible surface reaction. Similar to the pretreatment during ZnO encapsulation, a reduction in the Zn content of the QDs can be observed during the first ALD cycles. The surface alteration of the QDs can be seen as the root cause of the loss in photoluminescence quantum yield. To preserve the quantum yield, a thin layer of TiO_2 was shown to sufficiently protect the QDs from any damaging effects during subsequent Al_2O_3 growth.

The use of *in situ* XRF and GISAXS helped us to uncover the important interplay between the highly reactive ALD precursors and the QD surface. The choice of encapsulation process can not only be governed by the material properties of the barrier layer, but needs to take into account the important difference in precursor chemistry and the corresponding effect on the surface sensitive QD system. Here, we have shown that e.g. the widely used ALD process for Al_2O_3 growth is not the optimal choice for the encapsulation of QDs, even-tough Al_2O_3 encapsulation is by far the most popular coating withing the ALD community.

9.2 Suggestions for Future Work

In this work, various *in situ* synchrotron based x-ray techniques were introduced as tools for ALD research. A growing interest in synchrotron based research can be seen within the ALD community, evident by an upcoming workshop on *Synchrotron Radiation to Study Atomic Layer Deposition*. [1]

To make synchrotron radiation accessible to the wider ALD community, a close interaction is needed between both beamline scientists and ALD researchers. Currently, several strategies are used to bring ALD research to a synchrotron facility. In a first approach, existing beamline equipment is being adapted to allow ALD deposition. [2] This approach can yield relatively fast and cost effective results, but poses a risk to the beamline equipment and can limit the flexibility for the ALD researcher. In a second approach, dedicated ALD reactors are being designed, specifically for synchrotron based ALD experiments. [3–5] These reactors can either be designed to be used at a specific beamline, optimized for the available x-ray techniques, or a degree of mobility can be incorporated into the design, allowing it to be moved between several beamlines and even different synchrotron facilities.

In part I of this work, various applications of synchrotron based x-ray techniques for *in situ* ALD research have been mentioned. Due to the possibility to study the very first ALD cycles and the interaction between the surface and the ALD precursors to a high level of accuracy, these techniques will provide an important tool in the study of nucleation behavior of various ALD processes. These studies can provide important insights into the more fundamental principles underlying these nucleation processes. For example the influence of surface mobility during metal ALD growth become accessible and this could lead to a greater understanding of the fundamental principle of metal ALD. This in turn could lead to a better control of for example particle formation during the first ALD cycles, which is important for applications ranging from memory cells to catalysis.

In part II we have used the available techniques to study ALD encapsulation of QDs. This remains an important field of research, as the ambient protection and incorporation of QDs into devices remains a challenge. ALD has shown promising results in both these areas, but as we have shown, unexpected interactions between the ALD precursors and the QD-surface can significantly affect the final functionality. Therefor, specific research is needed in combining ALD processes with various QD-systems.

Within the field of ALD research new themes are gaining traction within the

scientific community. A first is area selective ALD. Area selective ALD has been proposed as a promising way to perform patterning in semiconductor device manufacturing. Alignment by conventional lithography techniques is becoming increasingly challenging with continuing downscaling of device dimensions. By using differences in surface reactivity, area selective ALD only deposited material only where needed on a pre-patterned structure. This ensures self-alignment of all patterns. In situ GISAXS and XRF can prove to be a useful tool to both provide information about nanostructure encapsulation and about the available reactive surface area.

A second area of growing interest is molecular layer deposition (MLD). MLD specifically incorporates larger organic molecules within the ALD process. This results in hybrid organic-inorganic materials. In vacuo XPS en XAS can be further explored to gain more insight in the specific structure and chemical build-up of these organic materials. GISAXS could be used to study nanolaminates created by MLD.

Recently, various research groups have started research into atomic layer etching (ALE). Instead of adding a (sub-)monolayer of material during every ALD cycle, ALE removes material in a self-limiting way. In this field the high intensity and accuracy of synchrotron based techniques can prove invaluable tools. ALE is mainly explored as a tool to modify nanosctructures in a controlled way. GISAXS and XRF can here again provide information, unavailable to other in situ techniques.

In conclusion, *in situ* synchrotron based x-ray techniques can both advance knowledge in established applications of ALD and provide insight in novel areas of exploration within the field.

References

[1] M. Tallarida and J. Dendooven. *Synchrotron Radiation to Study Atomic Layer Deposition*, June 2016.

[2] K. Devloo-Casier, K. F. Ludwig, C. Detavernier, and J. Dendooven. *In Situ Synchrotron Based X-Ray Techniques as Monitoring Tools for Atomic Layer Deposition*. Journal of Vacuum Science & Technology A: Vacuum, Surfaces, and Films, 32(1):010801, 2014.

[3] R. Methaapanon, S. M. Geyer, C. Hagglund, P. a. Pianetta, and S. F. Bent. *Portable Atomic Layer Deposition Reactor for in Situ Synchrotron Photoemission Studies.* The Review of scientific instruments, 84(1):015104, jan 2013.

[4] J. A. Klug, M. S. Weimer, J. D. Emery, A. Yanguas-Gil, S. Seifert, C. M. Schlepütz, A. B. F. Martinson, J. W. Elam, A. S. Hock, and T. Proslier. *A Modular Reactor Design for in Situ Synchrotron X-Ray Investigation of Atomic Layer Deposition Processes*. Review of Scientific Instruments, 86(11):113901, nov 2015.

[5] J. Dendooven, R. K. Ramachandran, K. Devloo-Casier, G. Rampelberg, M. Filez, H. Poelman, G. B. Marin, E. Fonda, and C. Detavernier. *Low-Temperature Atomic Layer Deposition of Platinum Using (Methylcyclopentadienyl)trimethylplatinum and Ozone*. The Journal of Physical Chemistry C, 117(40):20557–20561, oct 2013.

List of Publications

1. **ALD encapsulation of supported CdSe/CdS/ZnS nanocrystals in a metal oxide matrix: TiO_2 vs Al_2O_3**
   K. Devloo-Casier, P. Geiregat, K. F. Ludwig , K. van Stiphout, A. Vantomme, H. Rijckaert, I. Van Driessche, Z. Hens, C. Detavernier and J. Dendooven
   Manuscript in preparation

2. **A case study of ALD encapsulation of quantum dots: embedding supported CdSe/CdS/ZnS quantum dots in a ZnO matrix.**
   K. Devloo-Casier, P. Geiregat, K. F. Ludwig , K. van Stiphout, A. Vantomme, H. Rijckaert, I. Van Driessche, Z. Hens, C. Detavernier and J. Dendooven
   Manuscript in preparation

3. **Improved thermal stability and retention properties of Cu-Te based CBRAM by Ge alloying**
   W. Devulder, K. Opsomer, G. Rampelberg, B. De Schutter, K. Devloo-Casier, M. Jurczak, L. Goux and C. Detavernier
   Journal of Materials Chemistry C, vol. 3, pp. 12469-12476, 2015

4. **Plasma-enhanced atomic layer deposition: a gas-phase route to hydrophilic, glueable polytetrafluoroethylene**
   A. K. Roy, J. Dendooven, D. Deduytsche, K. Devloo-Casier, K. Ragaert, L. Cardon, and C. Detavernier
   Chemical Communications, vol. 51, no. 17, pp. 3556-3558, 2015.

5. **Controllable nitrogen doping in as deposited TiO_2 film and its effect on post deposition annealing**
   S. Deng, S. W. Verbruggen, S. Lenaerts, J. A. Martens, S. Van den Berghe, K. Devloo-Casier, W. Devulder, J. Dendooven, D. Deduytsche, and C. Detavernier
   Journal Vacuum Science and Technology A: Vacuum, Surfaces, Film., vol. 32, no. 1, p. 01A123, 2014.

6. **Air-stable short-wave infrared PbS colloidal quantum dot photoconductors passivated with Al_2O_3 atomic layer deposition**
   C. Hu, A. Gassenq, Y. Justo, K. Devloo-Casier, H. Chen, C. Detavernier, Z. Hens, and G. Roelkens
   Applied Physics Letters, vol. 105, no. 17, p. 171110, Oct. 2014.

7. **In situ synchrotron based x-ray techniques as monitoring tools for atomic layer deposition**
   K. Devloo-Casier, K. F. Ludwig, C. Detavernier, and J. Dendooven
   Journal of Vacuum Science and Technology A: Vacuum, Surfaces, Film., vol. 32, no. 1, p. 010801, 2014.

8. **In situ XAS and XRF study of nanoparticle nucleation during O_3-based Pt deposition**
   M. Filez, H. Poelman, R. R. K. Ramachandran, J. Dendooven, K. Devloo-Casier, E. Fonda, C. Detavernier, and G. B. Marin
   Catalasis Today, vol. 229, pp. 2-13, Jun. 2014.

9. **In Situ IR Spectroscopic Investigation of Alumina ALD on Porous Silica Films: Thermal versus Plasma-Enhanced ALD**
   E. Levrau, K. de Kerckhove, K. Devloo-Casier, S. Pulinthanathu Sree, J. A. Martens, C. Detavernier, and J. Dendooven
   Journal of Physical Chemistry C, vol. 118, no. 51, pp. 29854-29859, 2014.

10. **Atomic layer deposition-based tuning of the pore size in mesoporous thin films studied by in situ grazing incidence small angle X-ray scattering**
    J. Dendooven, K. Devloo-Casier, M. Ide, K. Grandfield, M. Kurttepeli, K. F. Ludwig, S. Bals, P. Van Der Voort, and C. Detavernier
    Nanoscale, vol. 6, no. 24, pp. 14991-14998, Oct. 2014.

11. **Low-Temperature Atomic Layer Deposition of Platinum Using (Methylcyclopentadienyl)trimethylplatinum and Ozone**
    J. Dendooven, R. K. Ramachandran, K. Devloo-Casier, G. Rampelberg, M. Filez, H. Poelman, G. B. Marin, E. Fonda, and C. Detavernier
    Journal of Physical Chemistry C, vol. 117, no. 40, pp. 20557-20561, Oct. 2013.

12. **In Situ Study of ALD Processes Using Synchrotron-based X-ray Fluorescence and Scattering Techniques**
    J. Dendooven, K. Devloo-Casier, M. Ide, K. Grandfield, K. F. Ludwig, S. Bals, P. Van Der Voort, and C. Detavernier
    ECS Transactions, vol. 50, no. 13, pp. 35-42, Mar. 2013.

13. **Low temperature plasma-enhanced atomic layer deposition of thin vanadium nitride layers for copper diffusion barriers**
G. Rampelberg, K. Devloo-Casier, D. Deduytsche, M. Schaekers, N. Blasco, and C. Detavernier
Applied Physics Letters, vol. 102, no. 11, p. 111910, 2013.

14. **Atomic Layer Deposition of TiO_2 on Surface Modified Nanoporous Low-k Films**
E. Levrau, K. Devloo-Casier, J. Dendooven, K. F. Ludwig, P. Verdonck, J. Meersschaut, M. R. Baklanov, and C. Detavernier
Langmuir, vol. 29, no. 39, pp. 12284-12289, Oct. 2013.

15. **Plasma-Enhanced ALD of Platinum with O_2, N_2 and NH_3 Plasmas**
D. Longrie, K. Devloo-Casier, D. Deduytsche, S. Van den Berghe, K. Driesen, C. Detavernier, S. den Berghe, K. Driesen, and C. Detavernier
ECS Journal of Solid State Science and Technology, vol. 1, no. 6, pp. Q123-Q129, 2012.

16. **Tuning the Pore Size of Ink-Bottle Mesopores by Atomic Layer Deposition**
J. Dendooven, B. Goris, K. Devloo-Casier, E. Levrau, E. Biermans, M. R. Baklanov, K. F. Ludwig, P. Van Der Voort, S. Bals, and C. Detavernier
Chemistry of Materials, vol. 24, no. 11, pp. 1992-1994, Jun. 2012.

17. **In Situ Monitoring of Atomic Layer Deposition in Nanoporous Thin Films Using Ellipsometric Porosimetry**
J. Dendooven, K. Devloo-Casier, E. Levrau, R. Van Hove, S. Pulinthanathu Sree, M. R. Baklanov, J. A. Martens, and C. Detavernier
Langmuir, vol. 28, no. 8, pp. 3852-3859, Feb. 2012.

18. **In situ synchrotron based x-ray fluorescence and scattering measurements during atomic layer deposition: Initial growth of HfO_2 on Si and Ge substrates**
K. Devloo-Casier, J. Dendooven, K. F. Ludwig, G. Lekens, J. D'Haen, and C. Detavernier
Applied Physics Letters, vol. 98, no. 23, p. 231905, 2011.

Acknowledgements
–Dankwoord–

The words and numbers on the preceding pages are not the sole result of my personal efforts, but the outcome of a wonderful collaboration. Various people have contributed to this work, either directly, in the form of scientific work or indirectly, as a source of moral support and in some rare cases, both. Therefore, it is only fitting that I conclude this thesis by thanking these people.

Thanking everybody involved, is an impossible task. For each person I mention, it seems like I am forgetting 10 others (see Figure). As a start, I thank everyone in the S1 building and in particular the people from the CoCooN research group. All of you made the S1 a pleasant place for me to work these past 5 years.

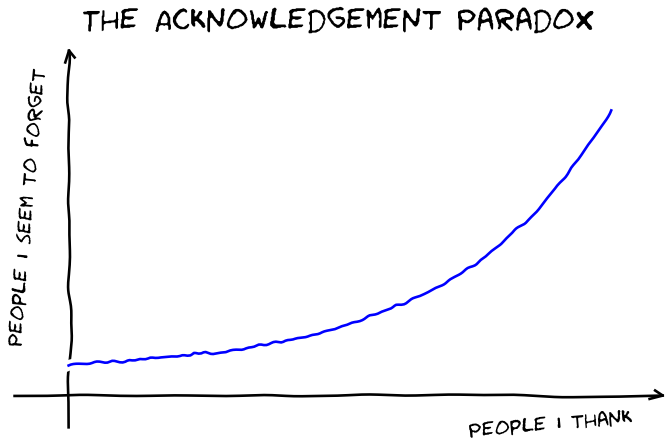

When I first arrived, working on my master thesis, I ended up in an office with Delphine. Quickly, I learned that she did not only provided the necessary conversation, but also a useful soundboard. A year later, Shaoren joined us. He served as a more silent presence to counter Delphine, but was always available for a critical view and a useful suggestion. Later Filip joined us for a year, leading to

absurd discussions and the discovery of the 'turbo pump' and/or 'bass clarinet' as a new unit to express the price of lab equipment. He later moved to an other office, but the sporadic absurd discussions remained. During the final years, Thomas got added to the 'office-mix', to add a drop of reason. Finally, Jakob arrived, filling the office again to maximum capacity. Together with Thomas, he converted me to the 'Ubuntu' philosophy. All these people made a magnificent mix, that made our office, an ever changing, pleasant environment to work in.

One of the most important people during these past years has been Jolien. She was my advisor during my master thesis and introduced me into the wonderful world of ALD research. Together we have spend countless hours at various synchrotron facilities. From the start in the dusty and cramped control room at X21 in NSLS, to the modern and spacious control room at SIXS in SOLEIL. During these synchrotron campaigns, we shared a passion for the research, resulting in interesting discussions and a refusal to let go of the experiments, leading in turn to minor sleep deprivation. Later Ranjith, Matthias(Minjauw), Eduardo, Matthias(Filez) and Hilde joined us at the various synchrotron campaigns adding new fresh view on our synchrotron work. It was always a pleasure working together and exploring the limits of human biorhythm.

A few other people deserve to be mentioned specifically. Davy, as the unofficial keystone of our research group, was always available to help fix various practical problems in the lab, which he magically always seemed to solve by his mere presence. Studying quantum dots, provided a link to the PCN research group. Pieter served as a perfect contact person, providing me with a never ending stream of quantum dot samples and PL data. Felix, Jan, Kevin, Liesje and Filip provided the munch needed distraction, with an occasional 'Friday Challenge' or 'S1 Movie Night'.

All of the people above, I would of course have never met, if I would not have been able to start my master thesis and later PhD research at the lab. Thank you Christophe for giving me this chance and motivating me throughout the years. You provided much needed guidance and always seemed to have an alternative view on the results. Pushing me to the optimal outcome.

Next to my colleagues, I obviously couldn't have done this, without the support of my friends and family. I particularly want to thank both of my parents and my brother for there unconditional support, even-though they not always knew what I was exactly doing. Thank you for supporting me in everything I have done. More and more, I realize how lucky I am to have you.

To conclude, I would like to dedicate this work to my grandparents, who are not able to see me finish my research, and more specifically, to my grandfather, Josef Casier, who passed away while I was writing this text.

Ghent, February 2016
Kilian Devloo-Casier